Development and Characterization of Magnetostrictive GaFe and Plasmonic Gold Thin Films

A Thesis
SUBMITTED TO THE FACULTY OF
UNIVERSITY OF MINNESOTA
BY

Eliot Lewis Cuthbert Estrine

IN PARTIAL FULFILLMENT OF THE REQUIREMENTS
FOR THE DEGREE OF
DOCTOR OF PHILOSOPHY

Professor Bethanie J. Hills Stadler

April 2015

Acknowledgements

I would like to thank all my family and friends who helped to make graduate school a genuinely enjoyable experience, especially my mother Nancy, father Robert and brother Evan for their continued support. Finally, I can't thank my advisor, Prof. Beth Stadler, enough for literally a decade of advice and guidance.

Abstract

As device sizes continue to shrink into the nano-scale, material development becomes increasingly important. This presents new deposition and characterization challenges which must be overcome to produce the next generation of devices. Magnetostrictive GaFe (galfenol) is one such material in which development of deposition and characterization techniques is necessary to enable new MEMS devices. In addition, plasmonic gold Near Field Transducers (NFTs) used in Heat Assisted Magnetic Recording (HAMR) require new characterization options to understand device failure modes as well as new gold deposition processes to improve device reliability. While these applications are very different, the underlying material deposition and characterization challenges involving thin film crystallinity are very similar.

Magnetostriction measurements of electrodeposited galfenol show that it is possible to achieve thin films of this material over a wide range of compositions using electrodeposition. In addition, grain refinement in gold was achieved through alloying which shows the potential to create more robust thin films while maintaining gold's desirable plasmonic properties. Finally, advanced characterization processes using Electron Back Scatter Diffraction (EBSD) were also developed to analyze thin film crystal structure and its role in NFT stability. These

results will further progress in the fields of MEMS and HAMR as well as provide the basis for identifying and solving materials challenges in the future.

Table of Contents

List of Tables

List of Figures

List of Equations

1 Introduction

Device scaling into the nano-scale presents many new material development challenges. In particular, deposition and characterization advancements involving thin film crystallographic structure are important to producing the next generation of devices. Magnetostrictive galfenol is one such application in which development of deposition and characterization techniques is necessary to enable new MEMS devices. In addition, plasmonic gold Near Field Transducers used in Heat Assisted Magnetic Recording (HAMR) require new characterization options to understand device failure modes as well as new gold deposition processes to improve device reliability. While these applications are very different, the underlying material deposition and characterization challenges involving thin film crystallinity are very similar.

Galfenol is a promising material due to its large magnetostriction constant (up to 400 ppm) and robust mechanical properties. A wide range of sensors, actuators and other transducers can be fabricated by taking advantage of galfenol's unique mix of magnetic and mechanical properties. Electrodeposition allows galfenol to be easily integrated into a variety of applications, such as torque sensors with conformal, monolithic active layers. In this work, we examine the underlying

factors that influence magnetostriction in electrodeposited galfenol including composition and crystallinity.

Successful deposition and evaluation of galfenol thin films is necessary for the design of galfenol based microelectromechanical (MEMS) and nanoelectromechanical (NEMS) devices. Stress is a primary concern because thick films and poor adhesion to substrates can lead to delamination and peeling. In addition, magnetostriction measurements require films that are uniform in thickness and composition over the sample area. Uniformity and composition were controlled by the use of a rotating disk electrode which created a uniform boundary condition across the sample during deposition. These results represent the first magnetostriction measurements of electrodeposited galfenol and show that it is possible to achieve magnetostrictive galfenol thin films over a wide range of compositions using electrodeposition.[1, 2]

Heat Assisted Magnetic Recording (HAMR) is another application which presents incredible materials challenges due to the large energy densities required during writing. While successful prototypes have been demonstrated and reliability has increased from "several tens of write cycles" in 2009 to 1000 "write power on" hours of operation in 2014, further improvement is required to produce a successful consumer product.[3, 4] In addition to materials challenges, HAMR requires

increased understanding of the process by which nanoscale plasmonic Near Field Transducers (NFTs) deform and fail due to thermal deformation.

One advantage of electrodeposited gold and gold alloys for this application is that they are not damaged by ion bombardment during patterning and can be widely modified through varying bath composition and deposition parameters.[5] In addition, grain refinement can be achieved through alloying which has potential to create more robust thin films while maintaining gold's desirable plasmonic properties. Advanced characterization processes using Electron Back Scatter Diffraction (EBSD) were developed to analyze thin film crystal structure and its role in NFT stability. These results will hopefully contribute to the successful implementation of HAMR as well as improve plasmonic device reliability in other applications.

While the two applications covered in this thesis may seem disconnected, development of deposition and characterization process solutions based on the fundamentals of materials science has produced remarkable results. These results will hopefully further progress in the fields of MEMS and HAMR as well as provide the basis for identifying and solving materials challenges in the future.

2 Thin Film Deposition

2.1 Thin film growth

2.1.1 Overview

Understanding the fundamental science behind thin film deposition is especially important to nano-scale device performance. There are many alternatives for thin film deposition including vacuum processes such as physical vapor deposition (PVD) and chemical vapor deposition (CVD), as well as wet processes like electrochemistry. However, all these processes share many common fundamentals.

Thin film growth modes are largely controlled by the surface energies between the deposited material and the substrate. Adatoms nucleate and form into droplets with a contact angle given by Young's equation, Equation 2-1.

$$\cos(\theta) = (\gamma_{sv} - \gamma_{fs})/\gamma_{fv}$$

Equation 2-1: Young's equation.

In this equation θ is the angle between the substrate and the nucleated droplet while the γ terms are surface energies between the substrate, film and vapor. This

results in 3 potential modes of thin film growth based on the possible surface energy relationships which are shown in Figure 2-1.[6]

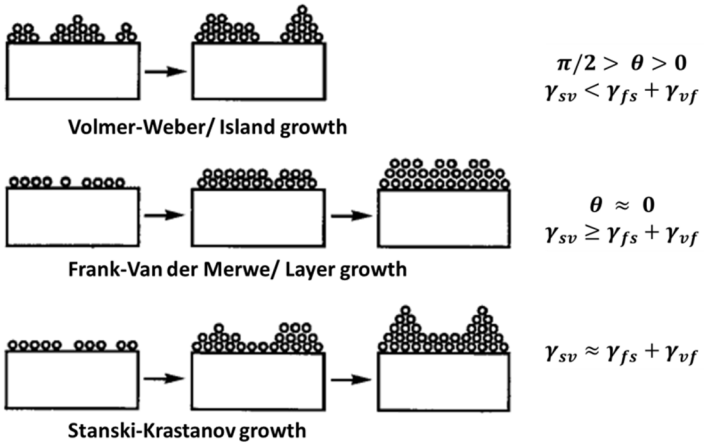

Figure 2-1: Thin film growth modes.[6]

The first mode occurs when film atoms bond more strongly to each other than the substrate and the contact angle is greater than 0 resulting in the formation of islands. This can be due to slow adatom diffusion and is therefore also due to substrate temperature as well as surface energies. This growth mode is referred to as Volmer-Weber or island growth and is especially relevant for metal deposition on oxides requiring the use of seed layers to produce continuous thin films. In the second case, the atoms in the deposited film bond strongly with the substrate and the contact angle between the film and substrate is 0. In this case, the film is deposited in monatomic layers and the growth mode is referred to a Frank-Van der Merwe or layer growth. The final growth mode occurs when bonding between film

atoms is significantly weaker than the bonding between adatoms and the substrate. In this mode, referred to as Stranski-Krastanov growth, the deposition produces layers initially followed by islands.[6, 7]

The importance of substrate temperature on thin film growth was mentioned above. As substrate temperatures increase, adatom diffusion and grain boundary mobility increases resulting in vastly different deposited thin films. At low temperatures, the lack of adatom and grain boundary mobility results in the formation of small, irregularly sized grains. In addition, voids can form when surface diffusion is not able to overcome the effects of shadowing during deposition. For moderate substrate temperatures, voids are eliminated and a columnar grain structure occurs. This type of growth is also common for electrodeposition. Finally, for large substrate temperatures, adatom mobility is high and bulk diffusion processes occur resulting in lateral grain growth and recrystallization. Twin boundaries are also more common under these deposition conditions.[8]

Grain size is also dependent on deposition rate. At higher deposition rates, new grains nucleate at a faster rate than grains coalesce. This relationship is shown in Equation 2-2 below.

$$l_g = 0.9(\dot{G}/\dot{N})^{1/3}$$

Equation 2-2: Mean grain diameter.

In this equation, $\dot{G}$ is the linear growth rate of grains in cm/s while $\dot{N}$ is the nucleation rate in nuclei/cm^2-s. Nucleation rate is proportional to the rate at which atoms impinge the substrate during deposition resulting in an average grain size that is inversely proportional to deposition rate.

Post processing techniques can also affect grain size. Heating a thin film results in grain growth according to Equation 2-3 where R_0 and R are the initial and final grain sizes, t is the heating time and k is a constant dependent on grain boundary energy and temperature.

$$R^2 - R_0^2 \approx kt$$

Equation 2-3: Grain growth due to heating.

This relationship correctly predicts parabolic grain growth in bulk solids, however in thin films, grain sizes are generally limited to 2 to 3 times the film thickness by the surface energies of the substrate and surface interfaces.

Film texture is another important parameter. Polycrystalline thin films are made of separate grains with individual crystallographic orientations. Under some conditions, these orientations are randomly distributed while other conditions produce a preferred orientation known as texturing. For example, fcc films often have their close packed (111) plane parallel to the substrate in order to minimize surface energy.[6]

2.1.2 Crystal Structure

As device critical dimensions continue to shrink into the nanoscale, the crystallographic orientation of individual grains in material becomes increasingly important. This can affect almost all material properties making the ability to understand and properly characterize crystal structure valuable.

Atoms can be arranged in a wide variety of configurations. By looking at the simplest possible representation of this configuration, the unit cell, it is possible to infer properties of the entire material. There are 14 different possible ways to arrange atoms in three dimensions such that when they are repeated they cover the entire space. These configurations are known as the 14 Bravais lattices. However, for metals, such as the materials studied in this work, cubic structures are the most common.[9]

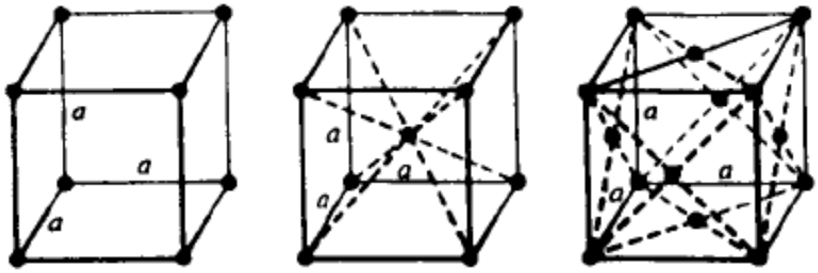

Figure 2-2: Cubic Bravais lattices.

Figure 2-2 shows three different cubic unit cells.[6] The first is referred to as simple cubic and is rarely seen in metals, it has one atom per unit cell. The second is body centered cubic (BCC), this lattice has 2atoms per unit cell and is the preferred structure for Iron. Finally, the third cubic lattice is face centered cubic (FCC) which has 8 atoms per unit cell and is the structure of Gold.[10]

The Bravais lattices describe the configuration of atoms in a sample; however it is also important to describe their orientation. This is done with Miller indices. Miller indices are used to describe planes and directions in a crystal with the indices h, k and l which correspond to the x, y and z directions. Calculating a Miller index for a plane is done by finding the intersections of a plane in a unit cell and then with each axis and then taking the reciprocal. Example Miller indices for some of the most commonly encountered planes are shown in Figure 2-3.

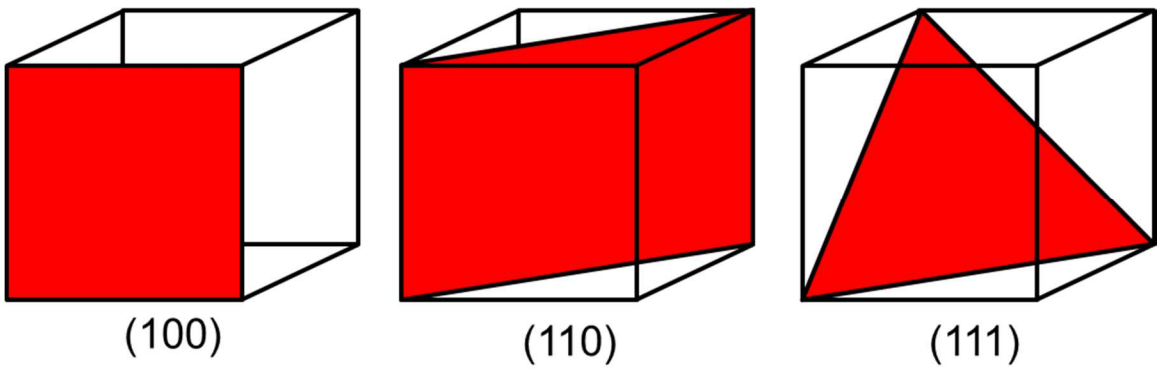

Figure 2-3: Example Miller indices.

Structures can be further described using bracket notation to differentiate between planes and directions in a crystal lattice. Individual planes are labeled with parentheses such as (100) in Figure 2-3 above while families of equivalent planes are labeled as {100}. Directions within a crystal lattice are labeled using square brackets such as [100]. For a cubic crystal system, a direction is defined as perpendicular to the plane with the same Miller indices. Families of equivalent directions can be collectively referred to using notation such as <100>.[9, 11]

In addition to being useful for describing planes and directions in a crystal lattice, Miller indices can be used to calculate the distance between parallel lattice planes. For a cubic crystal, the lattice spacing is given by the following equation where *h*, *k* and *l* are the Miller indices of a given plane and d_{hkl} is its spacing given a lattice constant, *a*.[12]

$$d_{hkl} = \sqrt{\frac{a^2}{h^2 + k^2 + l^2}}$$

Equation 2-4: Lattice plane spacing for a cubic crystal.

It is also useful to know the angle between 2 planes or vectors given their *hkl* notation. For 2 given planes, *hkl* and *h'k'l'*, their interplanar angle can be found using Equation 2-5.

$$\cos\theta = \frac{hh' + kk' + ll'}{\sqrt{h^2 + k^2 + l^2}\sqrt{h'^2 + k'^2 + l'^2}}$$

Equation 2-5: Interplanar angle formula.

2.1.3 Defects in thin films

Thin films also exhibit a variety of defects which can have a large impact on material properties. There are 3 categories of defects; the most basic are point defects. Point defects include vacancies where an atom is missing from a lattice site, interstitials where an additional atom is located between lattice sites and substitutions where an atom is replaced by an atom of a different element. Vacancies occur in all materials due to thermal energy as shown in Equation 2-6. For T = 1000 K and E_f = 1 eV, the unoccupied fraction of sites is $f = 10^{-5}$.

$$f = \exp(-\frac{E_f}{k_B T})$$

Equation 2-6: Vacancy probability due to thermal energy.

Point defects can also be specifically introduced through doping.

The second type of defects are line defects which include edge dislocations where an additional row of atoms is placed in the lattice and screw dislocations where the lattice is sheared. These types of defects are shown below in Figure 2-4.[6] Line defects can be described using the Burgers vector which is labeled **b** in

Figure 2-4. The Burgers vector measures the effect of a dislocation by showing the magnitude and direction of deformation compared to an undeformed crystal lattice.

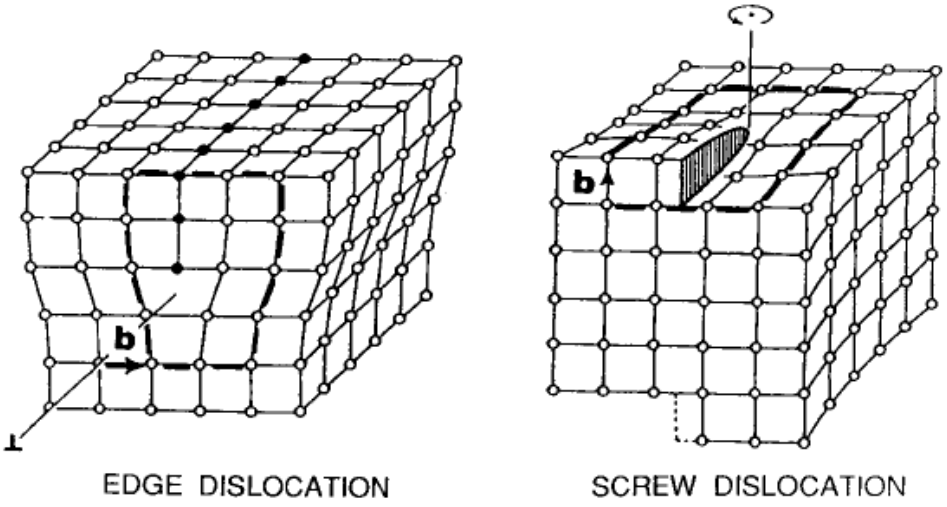

Figure 2-4: Types of dislocation defects.[6]

The final type of defects are planar or area defects. These are created by grain boundaries which separate individual single crystal grains in solids. Grain boundaries are especially high energy regions due to their large number of surface atoms and differences between adjacent grains. Defects help explain the mechanical and electrical properties of metals. Strain in metals can be explained by the creation and motion of dislocations which reduce the energy needed for deformation to occur. Electron scattering from defects gives a material its electronic properties, grain boundaries are especially significant because the number of atoms involved in grain boundaries can be as high as 1 out of 100 in thin films.

Grain boundaries also have a large effect on material strength by limiting the motion of dislocations. Dislocation motion is limited to within a single grain which can make thin films more resistant to deformation. This relationship is known as Hall-Petch grain size strengthening and can result in higher ultimate tensile strength for smaller grain sizes down to 10nm. Equation 2-7 shows that the ultimate tensile strength, σ_{UTS}, increases from its initial value, σ_i, proportional to a material specific strengthening coefficient, K, over the square root of the grain size, d. This property can be utilized to engineer more robust thin films by reducing their grain size.

$$\sigma_{UTS} = \sigma_i + \frac{K}{\sqrt{d}}$$

Equation 2-7: Hall-Petch equation.

The misorientation between textures in adjacent grains is known as the grain boundary angle and can impact film properties. The angle between two grains can be found by using the interplanar angle formula in Equation 2-5 for each grain's lattice orientation. Grain boundaries less than approximately 10 degrees are referred to as low angle grain boundaries and have lower energy which make them less susceptible to failure.[13] This behavior can be seen for the low angles in Figure 2-5, however there are many other possible low energy configurations at higher angles as well.

2.1.4 Coincident Site Lattice boundaries and twins

A special case of a grain boundary occurs when 2 adjacent lattices are at specific angles which cause some lattice sites to be shared. This creates a coincidence-site lattice, also known as a CSL boundary. CSL boundaries are important because they can have greatly lower energy than high angle grain boundaries.

For example, when adjacent [110] lattices are rotated 70 degrees apart in the [001] direction, it creates an overlap such that every third atom in the adjacent lattices overlap. Figure 2-5 shows an energy minimum at 70 degrees corresponding to this configuration.[13] In this configuration, the boundary between the two lattices occurs at a [111] lattice plane. This specific CSL boundary would be classified as a Σ3 boundary since every third lattice site is coincident, it is also possible to have Σ5, Σ7, Σ13 and higher boundaries. The classification and resulting lattice at the interface of several low energy CSL boundaries are labeled in Figure 2-5. Higher CSL boundary density has been shown to improve interconnect reliability and increase the mean time to failure.[14] Figure 2-5 also shows low grain boundary energy for small misorientation angles, defined as less than 10 degrees as discussed above.

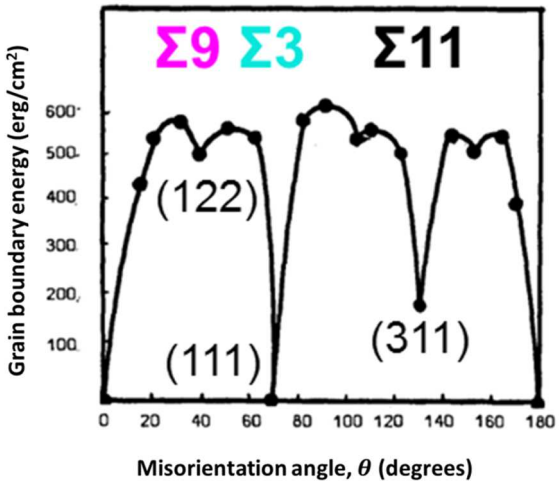

Figure 2-5: Grain boundary energy density versus misorientation angle for two mirrored [110] grains rotated symmetrically about a single axis.[13]

There are an incredible number of possible grain configurations due to the large number of degrees of freedom involved. In total, there are 5 degrees of freedom necessary to describe a grain boundary. 3 are used to describe the relative orientation of each grain while 2 are needed to describe the boundary between the grains. The graph in Figure 2-5 is only for the case of two mirrored [110] grains rotated symmetrically about a single axis. To account for all possible grain boundary configurations, as well as the orientation range of coincidence, a model proposed by D. G. Brandon is used.[15] This model is used by EBSD analysis software to determine whether a given grain boundary should be considered a CSL boundary.

If the two crystal lattices are symmetric about a CSL boundary, the boundary is said to be a twin. The energy minimum seen at 70 degrees in Figure 2-5 is the

result of a Σ3 twin. Twin boundaries are especially common in fcc metals because they can be created by introducing a stacking fault. If a fcc material has a sequence of layers given by ABCABCA, a stacking fault can cause the sequence to become ABC/A/CBA which creates a twin. This is shown below in Figure 2-6. Stacking faults and twin boundaries have extremely low energies and are widely observed in fcc metals.

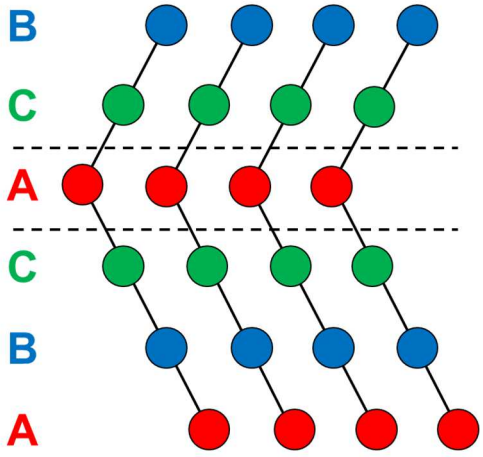

Figure 2-6: Twin boundary resulting from a stacking fault.

Grain boundaries can also be classified as coherent or incoherent. For a coherent CSL boundary, each atom on the adjacent lattice lines up exactly. If the atoms do not exactly coincide, the boundary is called incoherent. Both boundaries have the same boundary angle, but coherent boundaries have much lower energies.

2.2 Electrochemistry

2.2.1 Principles

Electrodeposition is a versatile thin film deposition technique with many research and industrial applications. While the chemistry and reaction dynamics of electrochemistry have been known for decades, its recent adoption by the semiconductor industry has shown that it is a viable technique for use in cutting edge fabrication. Electrodeposition has several advantages over other thin film vacuum deposition techniques. Unlike physical vapor deposition (PVD), electrodeposition is not a line of sight deposition process and can be used to fill high aspect ratio vias or templates.[16] In addition, electrodeposition is a relatively low cost process because it does not require the use of vacuum equipment. Finally, electrodeposition allows a wide range of materials to be deposited with a large degree of control over deposition conditions which effect the resulting thin films.

A standard electrochemical cell consists of the components needed to control an oxidation-reduction reaction. Reduction occurs at the cathode, or working electrode while oxidation occurs at the anode or counter electrode. There is also a reference electrode to measure the potential between the anode and cathode during deposition.

The electrochemical reaction proceeds according to the equilibrium shown in Equation 2-9.

$$M^{z+} \cdot nH_2O + ze^- \leftrightarrow M + nH_2O$$

Equation 2-8: Metal atom equilibrium equation.

In this equation, hydrated metal ions, $M^{z+} \cdot nH_2O$, are reduced to solid metal in the presence of an electrolyte. This is a reversible reaction and can be controlled by applying a potential. The metal/ metal ion equilibrium potential, E_0, is given by the Nernst equation, below, where $E_{0,standard}$ is the standard potential, F is the Faraday constant and Q the ratio of concentration of products to reactants.[17, 18]

$$E_0 = E_{0,Standard} + \frac{RT}{zF} \ln Q$$

Equation 2-9: The Nernst equation.

It is therefore important to understand how the concentration of the ions involved in the reaction changes during the electrodeposition process. Ions are depleted at the surface of the cathode during deposition creating a concentration gradient and boundary layer near the surface as shown in Figure 2-7.[17]

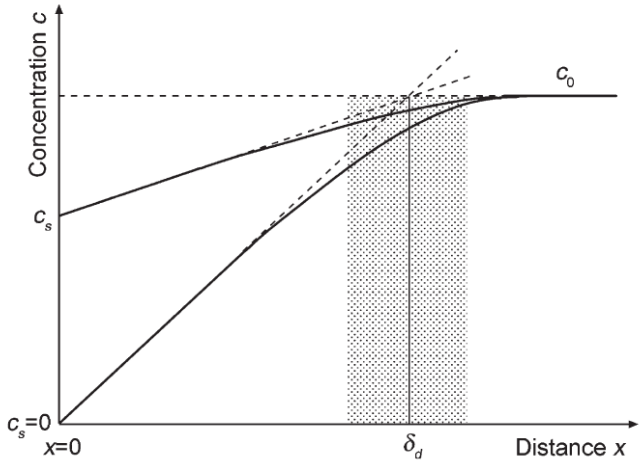

Figure 2-7: Electrolyte concentration versus distance from electrode.

Fick's first law, shown in Equation 2-10, describes the motion of ions across this boundary layer and shows that it is proportional to the diffusion constant, D, and in the opposite direction of the concentration gradient.

$$J = -D\frac{\partial c}{\partial x}$$

Equation 2-10: Fick's first law.

The motion of ions results in an electric current and can be combined with Fick's second law to produce calculate the concentration of ions at the deposition surface as a function of time. This equation is called the Sand equation and is shown in Equation 2-12.

$$\frac{\partial c}{\partial t} = D\frac{\partial^2 c}{\partial x^2}$$

Equation 2-11: Fick's second law.

$$c_s(t) = c_0 - \frac{|i|\sqrt{t}}{0.5nF\sqrt{\pi D}}$$

Equation 2-12: Sand equation.

The Sand equation shows that the ion concentration at the electrode surface decreases with the square root of time.[19] Since the equilibrium potential shown in Equation 2-9 is dependent on concentration this means that this potential also changes during deposition. The boundary layer thickness also increases with time according to Equation 2-13.

$$\delta = \sqrt{\pi D t}$$

Equation 2-13: Boundary layer thickness.

From Figure 2-7, the limiting current density can be calculated from the slope of the line when the electrolyte concentration at the surface, c_S, has been depleted.

$$i = \frac{nFD}{\delta} c_0$$

Equation 2-14: Limiting current density.

Equation 2-14 can be combined with the Equation 2-13 to produce the Cottrell equation shown in Equation 2-15 which gives current density as a function of time.[20] It can be seen that the deposition current will initially increase sharply then proceed to decrease proportional to $t^{-1/2}$.

$$i(t) = nF\sqrt{\frac{D}{\pi}}\frac{c_0}{\sqrt{t}}$$

Equation 2-15: The Cottrell equation.

The previous equations show the importance of the boundary layer on electrodeposition. To increase the limiting current density it is necessary to either increase the ion concentration, c_0, or decrease the boundary layer thickness, δ. However, these equations assumed a quiescent solution where diffusion is the only process available to cause ion motion. By introducing convection to the system it is possible to control the boundary layer and increase the limiting current density. Simply stirring the solution is one method, but to have more precise and repeatable control of the hydrodynamic conditions at the electrode, a rotating disk electrode (RDE) can be used. An example RDE is shown below in Figure 2-8.

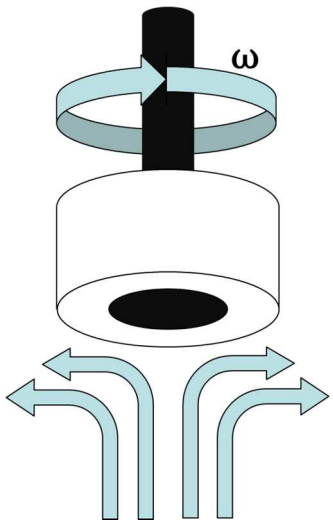

Figure 2-8: Rotating disk electrode.

When the electrode is rotated, centrifugal forces pull the electrolyte out towards the edge of the disc creating an approximately uniform boundary layer across the disk. The thickness of the boundary layer is given by Equation 2-16 where D is the diffusion coefficient, ν is the kinematic viscosity and ω is the rotation rate.

$$\delta = 1.61 \frac{D^{1/3} \nu^{1/6}}{\omega^{1/2}}$$

Equation 2-16: RDE diffusion layer thickness.

Equation 2-16 shows that for a given electrolyte with constant D and ν, the boundary layer thickness can be entirely controlled by the rotation rate. The limiting current density can then be calculated using the Levich equation in Equation 2-17 below since the limiting current density is based on the bulk electrolyte concentration and the diffusion layer thickness. Also, it is important to note that the limiting current density in Equation 2-17 is independent of r, which means that deposition is uniform across the electrode. Control of the limiting current density by rotation rate makes the rotating disk electrode an extremely valuable system for electrochemistry development.[21]

$$i = -0.62nF \frac{D^{2/3} \omega^{1/2} c_0}{\nu^{1/6}}$$

Equation 2-17: Levich equation.

In addition to mass transport, charge transfer at the electrode surface is a critical process for electrodeposition. The total current density is composed of the oxidation and reduction partial current densities and is shown in Equation 2-18, below.[22, 23, 24]

$$i = i_0 \left(e^{\frac{\alpha_a n F \eta}{RT}} - e^{-\frac{\alpha_c n F \eta}{RT}} \right)$$

Equation 2-18: Butler-Volmer equation.

In this equation, η is the overpotential, equal to $E - E_0$ while α_a and α_c are charge transfer coefficients with $\alpha_a + \alpha_c = 1$. If the system is not limited by mass transport conditions discussed above, the Butler-Volmer equation can be very useful for determining the kinetics of an electrochemical reaction.

2.2.2 Techniques

There are a variety of techniques for investigating the mass transport and kinetics properties of an electrochemical reaction discussed in the previous section. The ability to control the reaction with an applied voltage and measure the reaction progress as a current allows researchers to investigate the chemical reactions involved in electrochemistry.

One such technique is cyclic voltammetry (CV). In this procedure, the applied voltage is swept at a constant scan rate (in mV/s) in both a forward and

reverse direction while current is measured. CV is generally used with a stationary electrode in a quiescent solution to observe current peaks caused by the depletion of ions during electrodeposition as described by the Cottrell equation in Equation 2-15. The resulting current peak potentials, heights and widths give information about the reaction. Peak current at room temperature for a sweep rate of ν in Volts/second is given by the Randles-Sevcik equation shown in Equation 2-19 below.[17, 25, 26]

$$i_p = 2.6 \times 10^2 n^{3/2} \sqrt{D} c_0 \sqrt{\nu}$$

Equation 2-19: The Randles-Sevcik equation.

This equation can be used to derive the diffusion coefficient for a given electrochemical reaction.

Peaks due to both oxidation and reduction reactions are both observable using CV. If a reaction is reversible, a reduction peak will have a corresponding oxidation peak during the reverse sweep while an irreversible reaction will only contain a peak during the forward sweep. If it is not necessary to measure oxidation peaks, the current can be swept in only the forward direction in which case the technique is referred to as linear sweep voltammetry (LSV).

To investigate the kinetics of an electrochemical reaction, a Tafel plot can be generated by plotting the natural log of the current versus the overpotential. This

can be used to calculate the charge transfer coefficient seen in the Butler-Volmer equation (in Equation 2-18). With a conventional chemical reaction, it would be necessary to vary the temperature and observe the reaction rate. However, with an electrochemical reaction, the process is exponentially dependent on applied potential so it can be investigated at a constant temperature and the reaction rate is proportional to current so it can be easily measured. Since oxidation and reduction process may be different, it is possible to observe different Tafel slopes at positive and negative overpotentials. However, Tafel plots are only valid below the limiting current, where the reaction is kinetically limited and not mass transfer limited, as well as above the linear region close to the equilibrium potential.[27]

3 Morphology Characterization

3.1 Atomic Force Microscopy

3.1.1 Background

Atomic Force Microscopy (AFM) is a versatile measurement technique which takes advantage of the forces between a nano-structured probe and a sample to get information. While the most common AFM measurement produces the topography of the sample, it is also possible to measure a wide variety of sample properties capable of exerting a force on the probe. AFM can also be used to manipulate the sample though these interactions. The variety of measurements available using AFM make it a valuable technique for any material characterization project.[28]

This technique was first proposed in 1986 by Binning and Quate while working at IBM. By modifying the approach used for Scanning Tunneling Microscopy to observe the deflection of a cantilever, they were able to accurately measure the forces acting on the probe down to 10^{-18} N. These forces were then used to create a topographical image with a vertical resolution of less than 1 Å.[29] Since then there have been many advances made to the capabilities of AFM, however the technique remains under-utilized for material characterization.[30]

3.1.2 Theory of Operation

Atomic Force Microscopy relies on the interactions between a nano-probe and the sample surface. An example probe is shown in the inset of Figure 3-1 and is composed of a flexible cantilever and probe tip.[28] Despite being in the nano-Newton range, the forces acting on the probe tip are enough to cause a deflection in the cantilever. This deflection is amplified and detected by a quad photodiode.

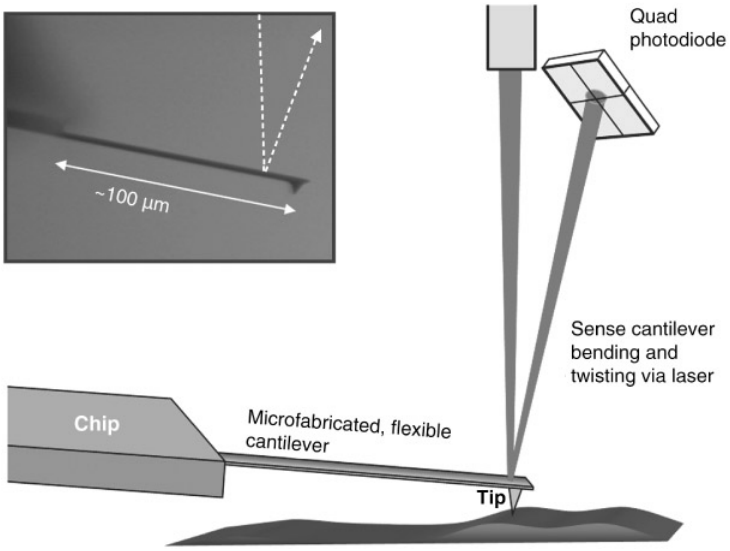

Figure 3-1: Schematic of AFM operation showing the probe, cantilever, laser and detector.[28]

The deflection of a cantilever is given by Hooke's law where F is the force acting on the cantilever, k is the cantilever spring constant and Δx is the deflection caused by the force. k is given by Equation 3-2 where w, t and L are the width, thickness and length of the cantilever and E is the Young's modulus of the cantilever material.

$$F = k\Delta x$$

Equation 3-1: Hooke's Law.

$$k = \frac{Ewt^3}{4L^3}$$

Equation 3-2: Cantilever spring constant.

There are several forces acting on the probe. The first to consider are van der Waals interactions, which are attractive forces due to the energy of dipole-dipole interactions. As the probe nears the sample, these van der Waals forces pull the probe closer to the sample. van der Waals forces are proportional to $1/r^6$ where r is the distance between the probe and sample.

In addition, there are repulsive forces present due to the electron orbitals of the probe and sample beginning to overlap. This is known as Pauli repulsion and is proportional to $1/r^{12}$. Together with the van der Waals forces discussed above, this creates a model known as the Leannard-Jones potential which is shown in Equation 3-3. In this equation, ε is the minimum energy of the system while σ is the distance at which the potential energy is 0.

$$U(r) = 4\varepsilon\left(\left(\frac{\sigma}{r}\right)^{12} - \left(\frac{\sigma}{r}\right)^{6}\right)$$

Equation 3-3: Lennard-Jones potential.

The Lennard-Jones potential is shown in Figure 3-2 below.[28]

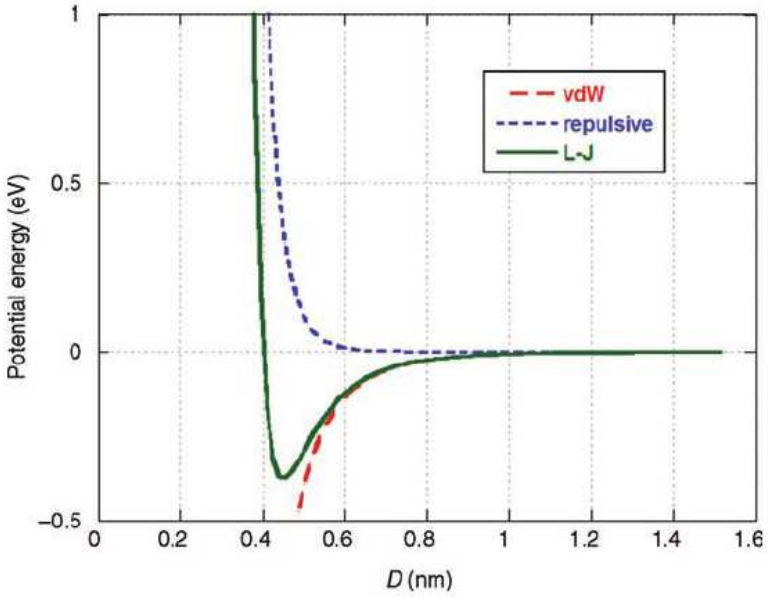

Figure 3-2: Energy due to forces acting on an AFM probe.[28]

While Pauli repulsion and van der Waals forces are the dominant forces acting on the probe during normal operation, the ability of AFM to detect extremely small forces present allows it to be used in a variety of interesting modes. One such mode is Magnetic-Force Microscopy (MFM). In this mode, the probe is magnetized which enables the sample magnetization to be measured by observing the interaction between the probe and sample. This small amount of force is enough to create a map of sample magnetization and is useful for measuring magnetic orientation in nanostructures.

The probe is rastered across the surface to measure the entire sample. A feedback loop is used to maintain a constant deflection (by maintaining a constant force per Hooke's law from Equation 3-1) by moving the sample up and down

relative to the probe. Measurements are normally performed in one of 2 modes. The first is "contact mode" where the probe is kept in physical contact with the sample. The second is "non-contact mode." In non-contact mode a cantilever of mass m is vibrated at its resonant frequency, given by Equation 3-4.

$$\omega_0 = \sqrt{\frac{k}{m}}$$

Equation 3-4: Cantilever resonant frequency.

The force acting on the cantilever changes this resonant frequency which can then be measured.

3.1.3 Measurement and Data Analysis

Choosing the correct measurement parameters is important to achieving useful AFM data. The image in Figure 3-3 shows the effect of modifying the feedback parameters on the measured data. All 3 images are taken from the same sample, a Si stamp from LightSmyth. Figure 3-3A shows a scan taken with feedback parameters that are too large, resulting in a resonance effect. In Figure 3-3B, the feedback parameters are too low resulting in a system that is unable to adjust fast enough to track the sample topography. Finally, Figure 3-3C shows a scan taken with optimized feedback parameters.

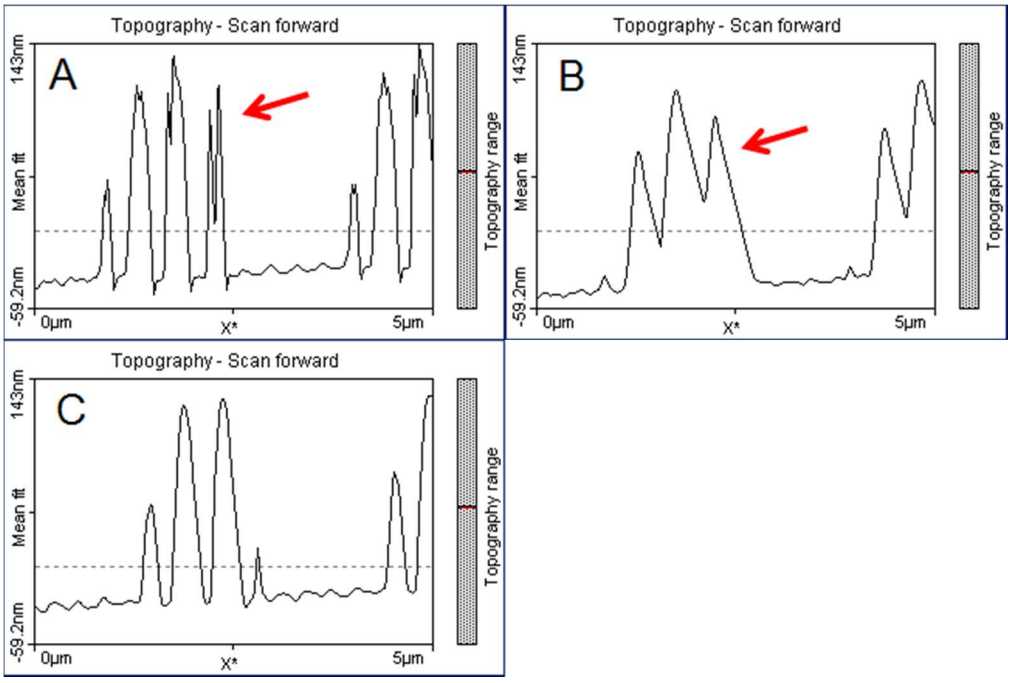

Figure 3-3: Effect of feedback parameters. A) Oscillation caused by excessive feedback B) Poor tracking due to slow feedback and C) Optimized imaging parameters.

Figure 3-4 highlights another potential issue in Atomic Force Microscopy, the possibility for artifacts. The most common artifacts are due to the geometry of the probe tip. Standard probe tips are pyramidal in shape with a tip radius of approximately 10nm. This means that it is difficult to resolve some high-aspect ratio structures such as nano-pores or nano-pillars. In addition, deterioration of the probe tip can cause the pyramidal probe shape to become convolved with the measured data. Figure 3-4 shows an array of cylindrical pillars manufactured by LightSmyth, as confirmed by Scanning Electron Microscopy. However, AFM results show triangular shaped features instead due to the use of a damaged scanning probe.

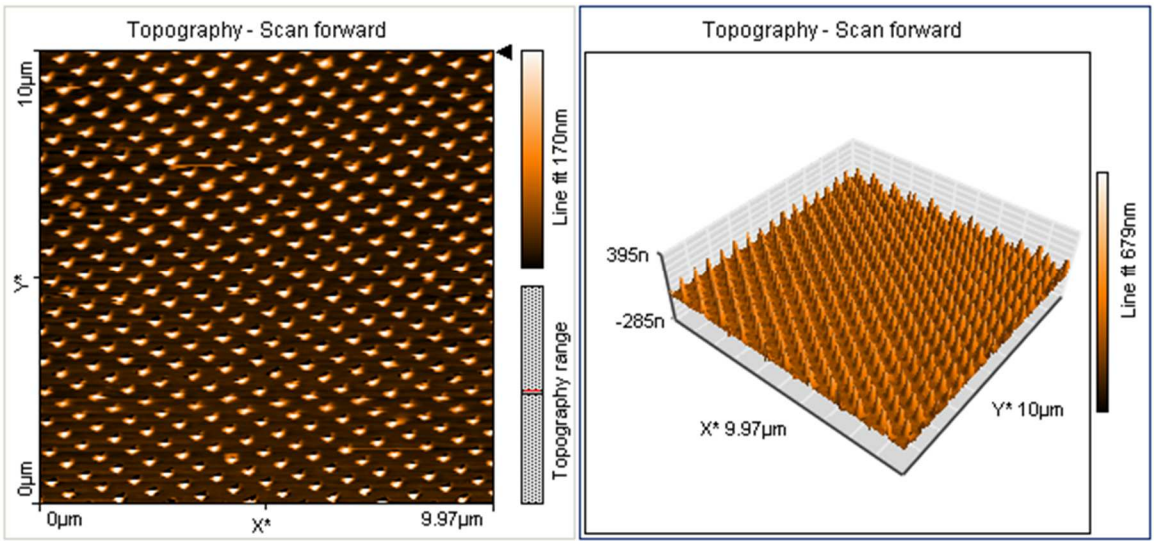

Figure 3-4: AFM scan of a LightSmyth stamp showing triangular features due to convolution with the tip shape (A) along with 3 dimensional representation (B).

One of the primary uses of AFM is roughness analysis. AFM is able to precisely quantify a sample's roughness which is difficult to do with other characterization techniques. The two primary ways of measuring roughness are average roughness, shown in Equation 3-5, and root mean squared (RMS) roughness, shown in Equation 3-6. These formulas give a simple roughness value by calculating the average distance between the height of each pixel and the average sample height. However, in many cases, these calculations over-simplify the roughness measurement and ignore potentially valuable information.

$$R_a = \sum_{n=1}^{N} \frac{|z_n - z_{average}|}{N}$$

Equation 3-5: AFM average roughness.

$$R_{rms} = \sqrt{\sum_{n=1}^{N} \frac{\left(z_n - z_{average}\right)^2}{N}}$$

Equation 3-6: AFM root mean squared roughness.

The above equations do not take into account the lateral spacing of the roughness. The length scale of roughness is especially important for plasmonic applications which have a greater sensitivity to roughness with a length scale less than 100 nm.[31] It is possible to retain this roughness length scale information with the use of the Power Spectral Density (PSD) function. The PSD function is generated by taking a Fourier transform of the height image and then plotting it squared versus wavelength as shown in Equation 3-7, below.

$$W(K_X) = \frac{2\pi}{XYh} \sum_{x=0}^{X} \left| \frac{h}{2\pi} \sum_{y=0}^{Y} z_{xy} e^{-iK_x yh} \right|^2$$

Equation 3-7: Power spectral density function for a X by Y image.

With this technique it is possible to see the breakdown of roughness as a function of length scale and gain a more detailed understanding of the sample surface.

A PSD function generated from the LightSmyth stamp seen in Figure 3-4 is shown below in Figure 3-5. The peak marked "A" corresponds to the spacing between pillars, approximately 500 nm or 2 per μm, while the peak marked "B" corresponds to the size and shape of the pillars. The other peaks such as those

around 20/ μm are due to shorter length scale factors such as film roughness.

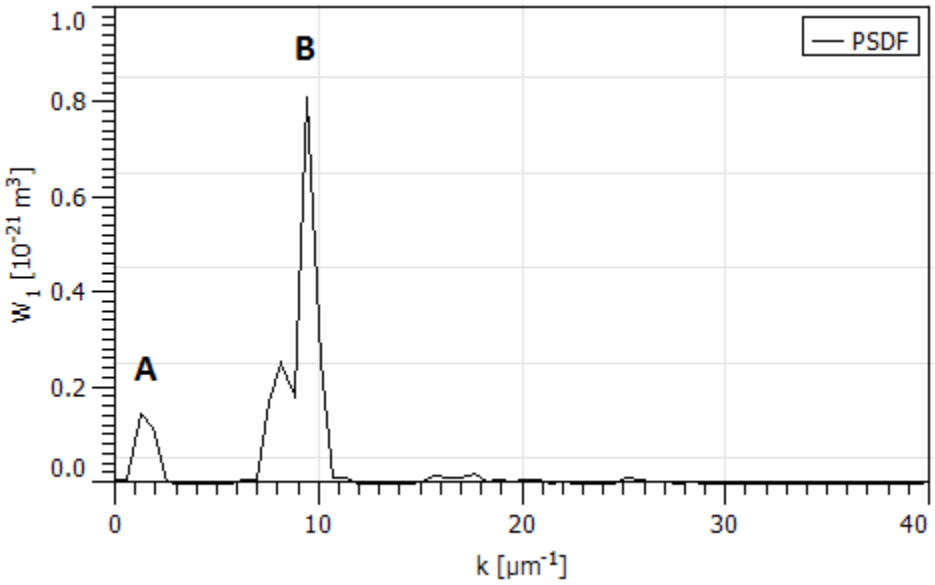

Figure 3-5: Power Spectral Density function example.

It can be seen that roughness due to the feature shape is about two orders of magnitude greater than the material roughness. By integrating W over a subset of K and then taking the square root, it is even possible to calculate a RMS roughness value which only includes a given range of length scales.

3.2 Crystallographic Measurement

3.2.1 X-Ray Diffraction

Lattice spacings described in Equation 2-4 as well as other material properties can be identified through the use of X-ray diffraction. Diffraction patterns result from the interference of X-rays that scatter off of a sample and are therefore dependent on the spacing between lattice planes in a sample. This property makes X-ray diffraction useful for elemental and phase analysis which are dependent on the unit cell as well as longer range properties such as texture and grain size which are dependent on the arrangement of lattice planes within the sample.

Diffraction from a crystal structure is given by Bragg's law, below. X-rays scatter off the atoms in the sample and can produce constructive and destructive interference. This is shown in Figure 3-6. An X-ray beam incident at an angle of θ scatters off lattice planes separated by a distance of d_{hkl}.

$$n\lambda = 2d_{hkl}\sin(\theta)$$

Equation 3-8: Bragg's law.

The incident beam has the same wavelength and phase, however it can be seen in Figure 3-6 that the X-ray which reflects off the lower lattice plane travels an

additional $2dsin(\theta)$ distance. If this distance is equal to $n\lambda$, then constructive interference will occur from this family of planes producing a characteristic X-ray peak. The incident beam angle is varied to produce a graph of diffracted intensity versus angle which can then be indexed and matched using a database of known materials.

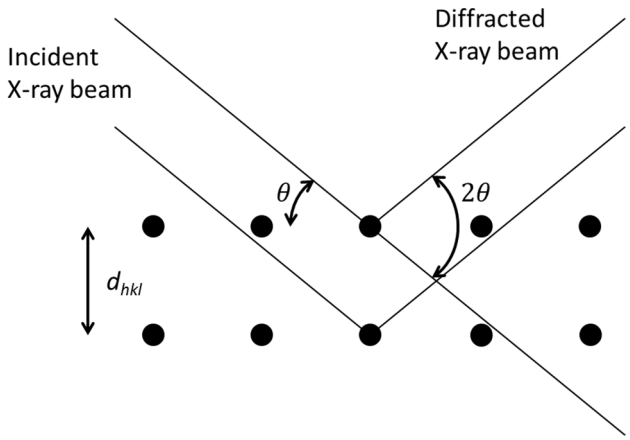

Figure 3-6: Bragg's law geometry.

In the case of gold, with a fcc structure and a lattice constant, a, of 4.08Å using Equation 2-4 gives a (111) lattice spacing of d_{111} of 2.355Å. Using a X-ray diffraction system with a Cu Kα source generating 1.541Å wavelength radiation produces constructive interference when the incident angle, θ, is 19.1°. The angle of the diffracted beam will be at 2θ (38.2°) with respect to the incident beam.

X-ray diffraction can also be a powerful technique for determining the crystallite size in a sample. For metallic thin films, the crystallite size is equal to the

grain size and can give valuable information about the film's properties. There are two primary ways of measuring crystallite size, the first is the Scherrer method. This process relates the full width half maximum (FWHM) of a peak to crystallite size in the direction normal to the peak's corresponding crystal plane. A variety of factors including instrument effects, microstrain and defects can also cause peak broadening making this technique only an approximation of crystallite size.

The Scherrer equation is shown below in Equation 3-9 for calculating the crystallite size, D. λ is the wavelength of X-ray radiation used for the measurement. κ is the Scherrer constant which depends on the crystallite shape and is equal to 0.94 for spherical grains of a cubic material, it is often approximated as 1. θ is the Bragg angle of the peak while β is the FWHM peak with after compensating for instrumental broadening effects.

$$D = \frac{\kappa\lambda}{\beta\cos(\theta)}$$

Equation 3-9: Scherrer equation.

There are a variety of possible XRD configurations, which all share similar characteristics. Figure 3-7 shows one such setup using a Bruker-AXS Microdiffractometer.[32] X-rays are generated using a Cu Kα source and focused onto the sample using a collimator tube. The angle between the incident X-ray beam and the sample is θ as show in Figure 3-6 above. In a Bragg-Brentano focusing

geometry, both the X-ray source and detector are equidistant from the sample and kept symmetric throughout the measurement. A goniometer is used to position the sample throughout the measurement. This setup also allows control of tilt (χ) and rotation (φ).

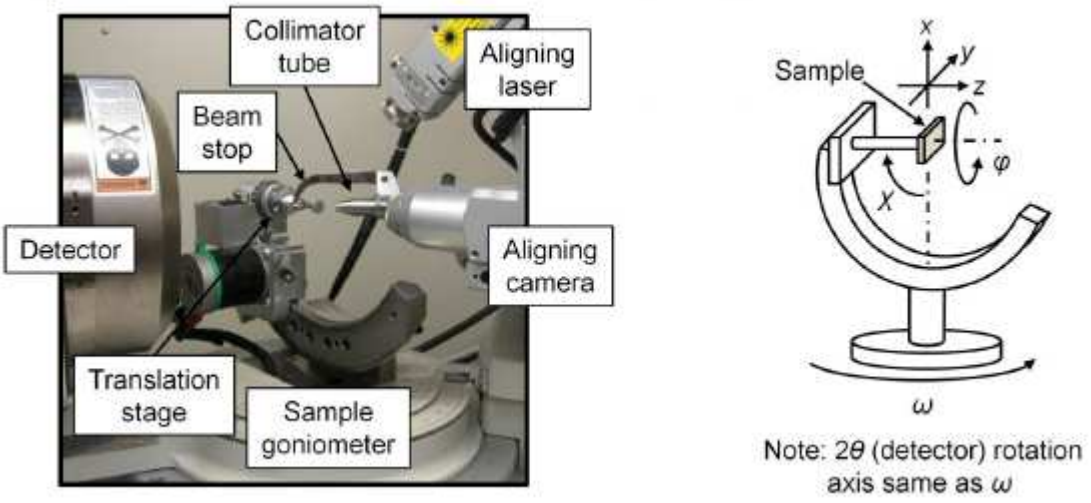

Figure 3-7: XRD geometry showing x-ray source, goniometer and areal 2D detector.

X-ray intensity measurements are taken at a series of θ values. When the Bragg condition in Equation 3-8 is met, a characteristic peak is seen. These peaks are then compared to those of known samples for indexing. When using the symmetric Bragg-Brentano geometry described above, only peaks corresponding to d_{hkl} spacings of planes parallel to the sample substrate are observed.[12]

In order to measure out-of-plane texture, a rocking curve measurement can be used in which the sample is tilted in the ω direction while maintaining the

positions of the source and detector. This technique can be used to measure the planes in a polycrystalline sample not parallel to the substrate at a given θ. The width of the peak generated by a rocking curve measurement can give information about crystallite size using Equation 3-9 and strain in a thin film.

It is also possible to observe film texture through the use of a 2 dimensional detector like the one shown in Figure 3-7. Many metal samples have a preferred texture due to the energetics of deposition and treatment. This results in a non-uniform diffraction pattern characteristic of the film texture. An example is shown below in Figure 3-8. The top image is from a randomly polycrystalline sample while the bottom image is from a recrystallized aluminum sample.[33]

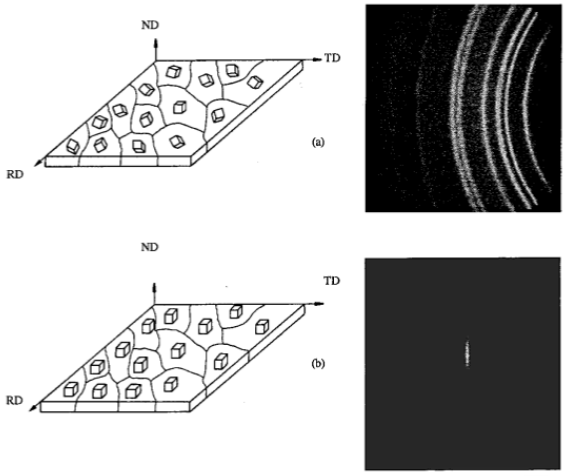

Figure 3-8: Grain orientation distribution and corresponding XRD patterns for polycrystalline (top) and textured (bottom) samples.[33]

Additional texture information can be obtained using a pole figure. By measuring a given peak intensity over a range of φ and χ angles, it is possible to construct a pole figure showing the distribution of texture direction present in a sample. An example pole figure is shown in Figure 3-9 for the (0002) peak in a titanium thin film.[6] The (0002) texture is strongly oriented in the Z direction (out of plane) which is common in thin film samples.

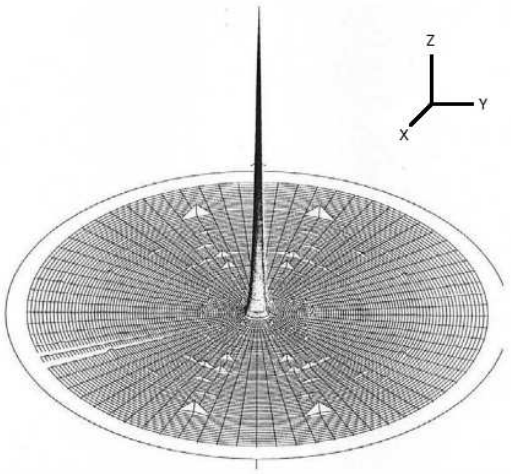

Figure 3-9: Example pole figure of Titanium.[6]

Measuring thin film samples with XRD sometimes requires different acquisition geometries. Grazing incidence diffraction is useful for measuring thin films or surfaces since x-rays in a conventional diffraction geometry can penetrate deeply into the sample. In this technique, the incident beam is placed at a low angle (< 5°) with respect to the sample surface and the detector is swept through the range of 2θ angles. The beam therefore travels mostly near the surface of the

sample. This process also increases the XRD signal by increasing the interaction volume of the x-ray beam within thin films since the X-rays may not travel through the thin film into the substrate.

3.2.2 Electron Backscatter Diffraction

In addition to X-rays, electrons can also scatter off a sample to create characteristic diffraction patterns. If electrons scatter elastically without losing their kinetic energy, they interact similarly to X-rays described above and can be analyzed using Bragg's law. However, electron scattering is much more probable than X-ray scattering which makes techniques based on electron scattering very useful for nanoscale characterization. When compared with X-ray diffraction based techniques, electron scattering based techniques can be used to analyze samples that are one million times smaller.[12, 34]

Sample composition can limit the resolution of electron scattering based techniques. Simulated electron trajectories in gold and silicon are shown below in Figure 3-10. Due to its higher atomic number and density Gold (left) shows a much smaller interaction volume as well as a larger back scatter coefficient. Gold has a density of 19.3g/cm^3 while silicon has a density of 2.33g/cm^3. The interaction volume is approximately 200nm for gold while it is approximately 2000nm for silicon. Trajectories shown in red are back scattered electrons, gold shows a back

scatter coefficient of 0.47 while silicon shows a much lower back scatter coefficient of 0.10.

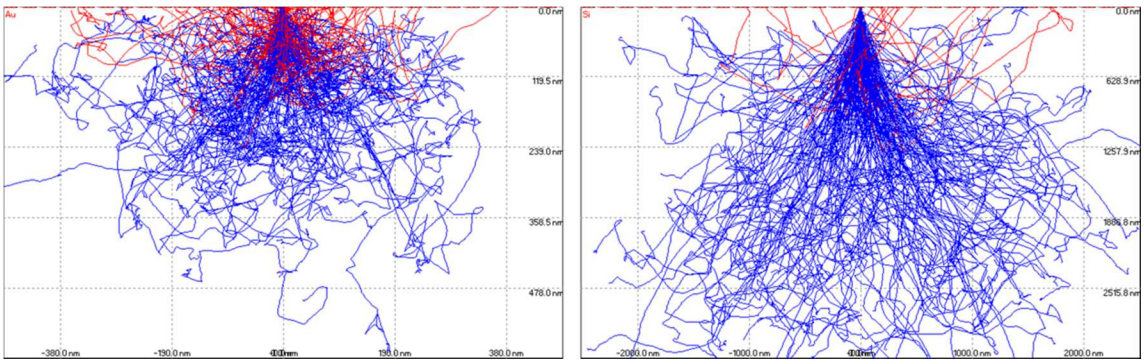

Figure 3-10: Simulated electron trajectories in Au (left) and Si (right).

When electrons scatter inelastically, the energy loss can be used to derive a variety of information about the sample. If an incident electron causes a vacancy by ejecting an inner shell electron, an electron from an outer shell will replace it, generating a characteristic X-ray which can be used for elemental analysis. This technique is referred to as energy dispersive spectroscopy (EDS). Ejected secondary electrons can also be used for SEM imaging.

Elastically scattered electrons do not have any change in their energy or wavelength and can interact to form characteristic diffraction patterns. Electrons are scattered off lattice planes at the Bragg angle creating a dark band in the direction of the incident beam and a light band at the Bragg angle. Diffraction cones produced by a lattice plane are shown in Figure 3-11 below.[35] These lines are

referred to as Kikuchi lines. Example diffraction patterns for Gold and Pyrite in the <111> direction are shown in Figure 3-12 below.

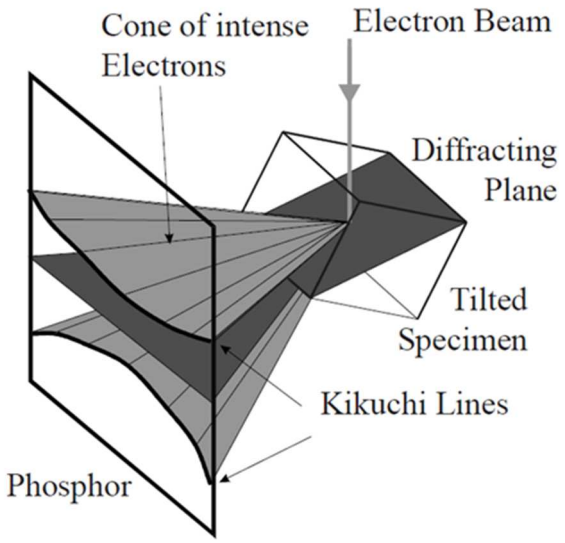

Figure 3-11: Example diffraction cones generated from a crystal lattice.[35]

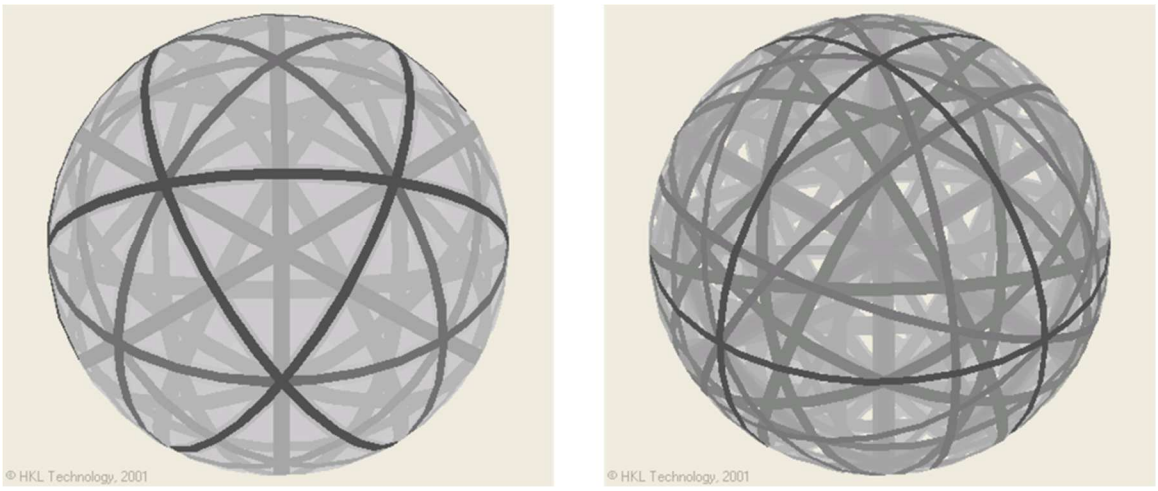

Figure 3-12: Spherical Kikuchi maps for Gold (left) and Pyrite (right).

Electron Back Scatter Diffraction (EBSD) uses this scattering behavior to characterize texture and phase in complement to elemental analysis available

through EDS. In EBSD, a phosphor screen is used to collect scattering patterns which are then indexed by computer. The sample is typically held at an angle of 70 degrees to the incident beam while the detector is positioned to the side as shown in Figure 3-13 below in order to maximize electrons scattered near the surface and improve image quality. The phosphor detector captures the Kikuchi lines shown in Figure 3-11. Since the electron scattering is confined to the interaction volume pictured in Figure 3-10, this technique allows characterization of texture on the nano-scale. Crystallographic information from areas as small as 30 nm has been obtained using this technique and resolutions are typically better than 1 μm. By rastering the electron beam across a sample, it is possible to generate a texture map and extract a variety of useful crystallographic data.[36, 37, 38]

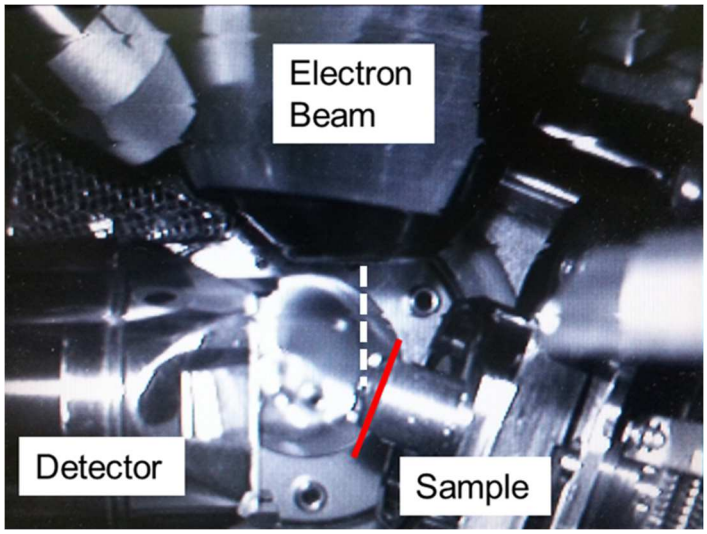

Figure 3-13: Standard Electron Backscatter Diffraction geometry.

4 Material Properties

4.1 Magnetostriction

4.1.1 Fundamentals and Applications

Magnetostriction is the strain (shape change) of a magnetic sample in the presence of a magnetic field. This effect is generally small, on the order of 10's to 100's of parts per million; however it can still be utilized for a number of practical applications.[39] The strain induced by the magnetostriction effect is denoted by the symbol λ.

$$\lambda = \frac{\Delta l}{l}$$

Equation 4-1: Magnetostrictive strain.

When the measured magnetostrictive strain is in the same direction as the magnetization, the magnetostriction of a cubic sample is given by the following equation.

$$\lambda_{Si} = \frac{3}{2}\lambda_{100}\left(\alpha_1^4 + \alpha_2^4 + \alpha_3^4 - \frac{1}{3}\right) + 3\lambda_{111}(\alpha_1^2\alpha_2^2 + \alpha_2^2\alpha_3^2 + \alpha_3^2\alpha_1^2)$$

Equation 4-2: Magnetostriction equation in a cubic crystal.

In this equation, λ_{100} and λ_{111} are the single crystal magnetostriction values in the (100) and (111) directions and the α terms are direction cosines.[39] Average magnetostriction can then be calculated with the following integral.

$$\overline{\lambda_{Si}} = \frac{4}{2\pi}\int_{\theta=0}^{\pi/2}\int_{\phi=0}^{\pi/2}\lambda_{Si} sin\phi d\phi d\theta$$

Equation 4-3: Polycrystalline magnetostriction calculation.

The factor of 4 in the above equation accounts for symmetry in our calculation. When the integral is computed, the value for average magnetostriction from a polycrystalline thin film is given by Equation 4-4.

$$\overline{\lambda_{Si}} = \frac{2\lambda_{100} + 3\lambda_{111}}{5}$$

Equation 4-4: Average magnetostriction for a polycrystalline sample.

The integral in Equation 4-3 can also be solved for textured samples by choosing the appropriate direction cosines to describe the system as will be done in section 5.3.

4.1.2 Iron-Gallium alloys

Iron-Gallium alloys (galfenol) were first proposed as an option for applications such as energy harvesting, torque sensing and actuation which require a material with large magnetostriction, high durability and low cost.[40, 41] The addition of nonmagnetic Ga atoms greatly increases the magnetostriction of iron in the (100) direction.[42] Magnetostriction constants (λ_{100}) as high as 400 ppm have

been measured in single crystal (100) galfenol, a dramatic increase when compared to the 20 ppm observed in pure single crystal iron.[40, 42, 43]

A wide range of sensors, actuators and other transducers can be fabricated by taking advantage of galfenol's unique mix of magnetic and mechanical properties. In addition, electrodeposition allows galfenol to be easily integrated into a variety of applications, such as torque sensors with conformal, monolithic active layers. Galfenol is also free of rare earth elements making it more economical than other giant magnetostrictive alloys.

4.1.3 Measurement

Magnetostriction values can be determined in a number of ways. For bulk samples, a commercial strain gauge can be used in conjunction with a bridge circuit to measure the small change in resistance caused by magnetostrictive strain. It is also possible to utilize the inverse magnetostrictive effect by applying a stress to the sample and measuring a change in the sample's magnetic anisotropy.[39]

For thin films, a variety of capacitance, inductance or optical measurements can be performed to measure the deflection of a magnetostrictive thin film and non-magnetic substrate. A capacitance bridge system is one such device which uses a parallel plate capacitor configuration shown in Figure 4-1 in which one side of the

parallel plate capacitor is a magnetostrictive thin film. Deflection due to magnetostrictive strain causes a change in capacitance which can be observed using a bridge circuit.

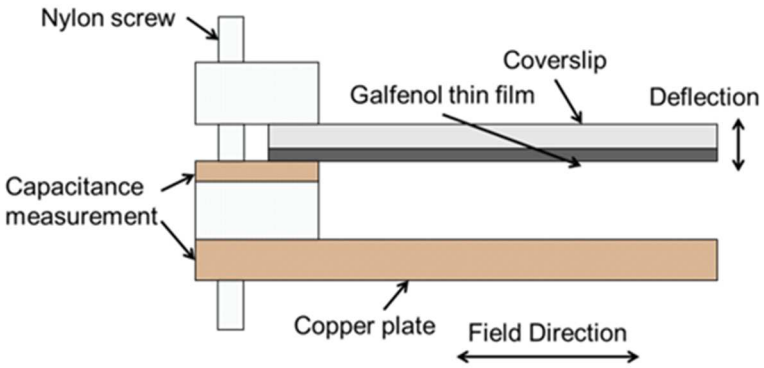

Figure 4-1: Capacitance bridge setup for magnetostriction measurement.

For the system shown in Figure 4-1 above, the amount of deflection is given by Equation 4-5.

$$d = \frac{3t_f l^2 \lambda_m E_f (1 - v_s)}{t_s^2 E_s (1 + v_f)}$$

Equation 4-5: Cantilever deflection due to magnetostriction.[44]

In Equation 4-5, t_f is the film thickness, t_s is the substrate thickness and l is the length of the sample. E and v are the Young's modulus and Poisson's ratio of the film and substrate.[44] Deflection can be measured by a change in capacitance according to Equation 4-6.

$$d = \frac{-\varepsilon_0 A \Delta C}{\left(C_0 - C_{empty}\right)^2}$$

Equation 4-6: Deflection and capacitance relationship.

In this equation, A is the sample area, ΔC is the change in capacitance measured between the on and off states of the electromagnet, C_0 is the capacitance at zero field and C_{empty} is the capacitance without a sample present. Equation 4-5 and Equation 4-6 can then be used to calculate the magnetostriction constant, λ_m, of the material by measuring the change in capacitance due to the substrate bending as shown in the following equation.[44, 45]

$$\lambda_m = \frac{k \Delta C}{t_f \left(C_0 - C_{empty}\right)^2}$$

Equation 4-7: Magnetostriction constant calculation.

4.2 Plasmonics

4.2.1 Background and Theory

Plasmonics is a rapidly growing field of research with the potential to improve many areas of daily life. While plasmonic nanostructures have been utilized for over a thousand years, it was not until the early 1900's that a mathematical understanding of their behavior was found and only in the last 30 years has the technology existed to design and fabricate custom plasmonic structures. Already, in that short time there have been numerous advancements due to plasmonics research. One such advancement, Heat Assisted Magnetic Recording, offers the potential to overcome fundamental limits in data storage and enable cheap, high capacity hard drives. However, there are many challenges which must first be met by plasmonics researchers to improve understanding of this new technology and achieve its full potential.

The study of plasmonics is an exciting area with a range of potentially revolutionary applications. When light interacts with an interface between a metal and dielectric, under certain conditions, oscillations of surface electrons in the metal can allow electromagnetic energy to be confined at the surface of the metal. By localizing electromagnetic energy at the interface between a metal and a dielectric,

plasmonic structures can bypass the fundamental resolution limit regarding the confinement of light energy. This allows electromagnetic energy to be localized and focused by tuning the shape and materials of a plasmonic structure and enables the creation of many novel systems that could not otherwise exist using conventional optics.

Plasmonic based technologies have existed for over a millennium, however it was not until the 20th century that their operation was understood. One of the earliest examples of the use of plasmonics is the Lycurgus cup, shown in Figure 4-2 below. This cup is from Rome in 400AD and shows a green or red color depending on the incident light due to the plasmonic scattering and absorption of embedded nanoparticles. Stained glass used in the 1600's also takes advantage of the absorption of embedded nanoparticles to create unique colors.[46, 47]

Figure 4-2: The Lycurgus cup, dating from 400AD.[47]

Modern understanding of plasmonics began when Faraday investigated the properties of colloidal gold in the middle of the 19th century. In 1908, Mie derived equations for the absorption caused by nanoparticles by solving Maxwell's equations. This theory describes the resonance of nanospheres and is the basis for calculating the plasmonic response due to device shape.[48]

The next major advancement in plasmonic understanding began in the 1980's. Improvements in fabrication and characterization techniques allowed specific plasmonic shapes to be created and analyzed instead of just spheres. In addition, the increase in computation power allowed simulations of new shapes. These advancements, combined with promising initial results in the field of Raman spectroscopy led to an explosion in plasmonics research and applications.[46, 47, 49, 50]

In metals, the plasma frequency is the frequency at which a metal becomes transparent to incident electromagnetic radiation or light. At low frequencies, the electrons in the metal create a damping effect causing incident light to be reflected. Electrons can be treated as a plasma because of the large number of free electrons present. The plasma frequency of a metal is given by Equation 4-8.

$$\omega_p = \frac{ne^2}{\varepsilon_0 m}$$

Equation 4-8: Plasma frequency.

In this equation, n is the density of electrons with charge e and mass m while ε_0 is the free space permittivity. For most metals, this value exists in the UV range resulting in their reflective appearance. This oscillation of electrons in response to incident radiation is the key mechanism behind the plasmonic effect.[49]

For a nanoparticle, the polarizability of the particle is given by Equation 4-9.

$$\alpha = 4\pi a^3 \frac{\varepsilon_m - \varepsilon_d}{\varepsilon_m + 2\varepsilon_d}$$

Equation 4-9: Nanoparticle polarizability.

In this equation, a is the particle radius, ε_m is the relative permittivity of the metal and ε_d is the relative permittivity of the dielectric. This equation shows that the relative permittivity of the metal should be equal to $-2\varepsilon_d$ to achieve a large polarizability. Metals like gold have large negative permittivities at optical frequencies as shown in Figure 4-3 and therefore make good candidates for plasmonic structures.

The permittivity of a material can be described as a complex value using the Drude equation shown in Equation 4-10 where ε'_m is the real part of the metal's complex permittivity while $i\varepsilon''_m$ is the complex part.

$$\varepsilon_m(\omega) = \varepsilon'_m(\omega) + i\varepsilon''_m(\omega) = \varepsilon_{int} - \frac{\omega_p^2}{\omega(\omega - i\Gamma)}$$

Equation 4-10: The Drude model.

This equation represents the Drude theory for damping in a metal. The ω_p term is the plasma frequency as described above in Equation 4-8. ε_{int} is due to transitions between energy bands and is equal to 1 for an ideal system. Finally, Γ is the relaxation frequency of the electrons. This Γ term can be size and shape dependent allowing the response of a material to be engineered. Drude model parameters for 4 common plasmonic materials are shown in Table 4-1 below.[51]

Material	ε_{int}	ω_p (eV)	Γ (eV)	ω_{int} (eV)
Silver	3.7	9.2	0.02	3.9
Gold	6.7	8.9	0.07	2.3
Copper	6.7	8.7	0.07	2.1
Aluminum	0.7	12.7	0.13	1.14

Table 4-1: Drude model parameters for common plasmonic materials.

Using the Drude model of permittivity described above, Maxwell's equations can be solved for the conditions under which a surface wave is a solution. This surface wave can be used to transmit electromagnetic energy along the interface between the metal and dielectric. The wavevector of this surface plasmon is given by Equation 4-11.

$$k_{SPP} = k_0 \sqrt{\frac{\varepsilon_m \varepsilon_d}{\varepsilon_m + \varepsilon_d}}$$

Equation 4-11: Surface plasmon wave vector.

The propogation length of the surface plasmon is given by Equation 4-12.

$$\delta_{SPP} = \lambda_0 \frac{(\varepsilon'_m)^2}{2\pi\varepsilon''_m}\left(\frac{\varepsilon'_m + \varepsilon_d}{\varepsilon'_m\varepsilon_d}\right)^{3/2}$$

Equation 4-12: Surface plasmon propogation length.

Both the wavevector, k_{SPP}, and the propogation length, δ_{SPP}, should be large for an effective plasmonic device.[49]

Since for a given application, the wavelength and dielectric permittivity are fixed, Equation 4-12 can be simplified to produce a quality factor term useful for evaluating plasmonic metals. In addition, ε'_m is generally much larger than ε_d, so the 3/2 term can also be approximated as the constant $(1/\varepsilon_d)^{3/2}$ and the equation can be further reduced to produce the Q factor of the system shown in Equation 4-13.

$$Q_{SPP}(\omega) = \frac{\varepsilon'_m(\omega)^2}{\varepsilon''_m(\omega)}$$

Equation 4-13: Plasmonic quality factor.

This value should also be large for an effective plasmonic device.[51]

These equations imply that ε'_m should be large and negative while ε''_m should be small. A large and negative real part of the relative permittivity, ε'_m, corresponds to a metal that is highly reflective while a small real part of the permittivity, ε''_m, corresponds to a metal that has low loss. Gold and silver are some of the most promising plasmonic materials because their complex permittivity matches these requirements.[46, 49, 51]

While gold and silver are the most commonly researched plasmonic materials, other metals show promising results for specific applications. These metals are summarized in Figure 4-3 below.[51] The real and complex parts of several potential metals are shown as a function wavelength. While silver shows the best response, it also tarnishes and degrades quickly. Copper has an advantage of being cheaper than gold or silver while still showing reasonable plasmonic performance.

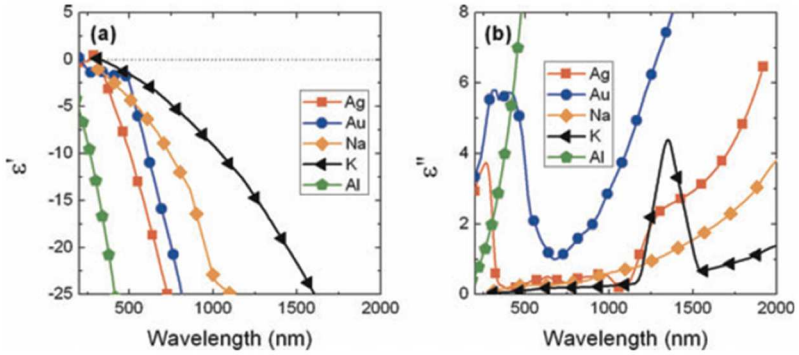

Figure 4-3: Dielectric properties of common plasmonic materials.

It is also possible to create plasmonic devices out of metal alloys. Alloys can improve on specific weaknesses, such as the softness of gold, while maintaining desired plasmonic characteristics. In addition, alloying can dope the metal and alter its Fermi level, band structure and absorption. Semiconductors can also have negative ε' required for plasmon resonance, these materials require heavy doping and show plasmonic characteristics in the IR frequency range. Finding the correct material for a given application is critical to fabricating plasmonic devices.

The shape of a nanostructure can have a significant impact on its plasmonic properties. In Equation 4-10 above, the Γ term is size and shape dependent. By varying the shape, the complex permittivity of the structure can also be varied. This opens up a branch of plasmonics research dedicated to understanding this interaction. The shape of the plasmonic structure is also critical for the power transmission efficiency. Shapes can be simulated using finite element models of Maxwell's equations.[52]

4.2.2 Heat Assisted Magnetic Recording

Due to advances in simulation and fabrication, the last 2 decades have seen rapid advancements in plasmonics research. While plasmonic properties have been utilized for hundreds of years, the rise in nanofabrication capabilities and the need for high energy confinement have created a new field of study. Many prototype plasmonic structures and devices have been fabricated and there is a greater understanding of plasmonics shapes, materials and theory.

One such area is in magnetic recording. Over the years, areal data density has increased exponentially, however, the superparamagnetic limit prevents further scaling due to the instability of the small magnetic grains needed to record data at higher densities. Heat Assisted Magnetic Recording has the potential to overcome this limit by using plasmonic nanostructures to localize electromagnetic energy and

heat a small area to write stable high density data. This application requires advancements in many areas of plasmonic research including new materials, analysis techniques, design and reliability. While Heat Assisted Magnetic Recording is a complex project best suited to industrial groups, the individual advancements required are well suited for university research groups.

Figure 4-4, below shows the growth in areal density over the past 30 years. In fact, areal density has grown exponentially over the last 60 years, approximately doubling every 3 years since 1955. This exponential scaling has enabled larger and cheaper hard drives to meet the demand of businesses and consumers. However, in recent years this scaling has slowed significantly and may not continue due to the superparamagnetic limit.[53] The hard disk industry has been quick to adopt new technologies into their products, for example it took only about 10 years between the discovery of Giant Magnetoresistance (GMR) and its inclusion in products.[54] To achieve continued areal density growth, it will be necessary to incorporate plasmonic research into magnetic recording.

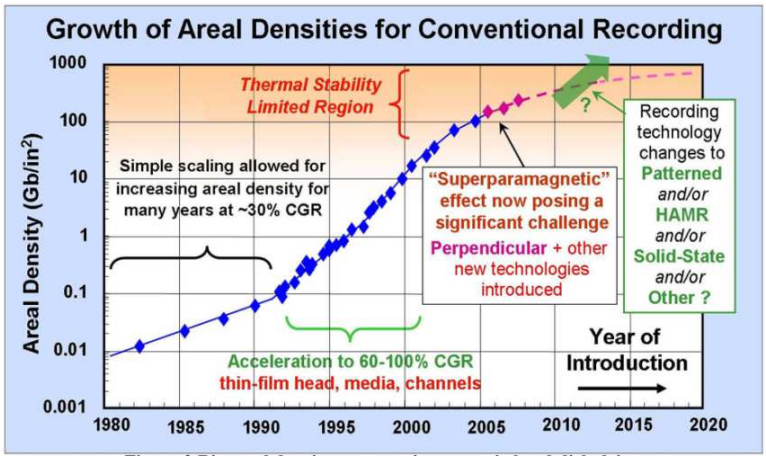

Figure 4-4: Hard Disk Drive areal density growth.[53]

The superparamagnetic limit is a density limit imposed by the thermal fluctuations and maximum magnetic field capable. This relationship is outlined in Figure 4-5 below.

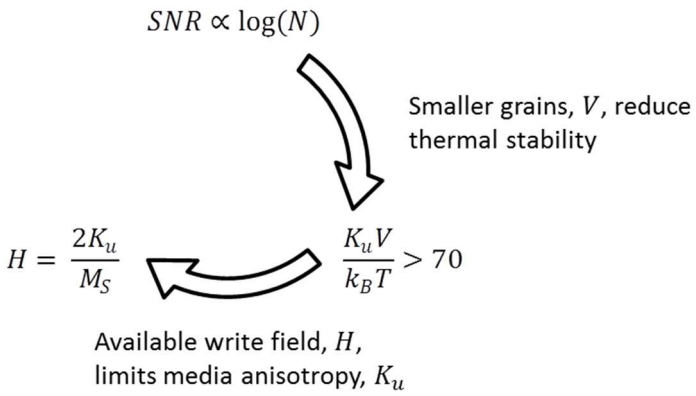

Figure 4-5: Magnetic recording trilemma.

Signal to noise ratio (SNR) in magnetic recording is approximately proportional to the log of the number of magnetic grains (N) that make up an individual bit of data.

$$SNR \propto \log(N)$$

Equation 4-14: Signal to noise ratio for magnetic recording.

Therefore, as each bit of data gets smaller, the individual grain size must also decrease in order to maintain the same signal to noise ratio. However, small grains can become unstable due to random thermal fluctuations switching their magnetic moment.[55] Equation 4-15 shows the average time between flips, τ_N, due to random thermal fluctuations in a magnetic nanoparticle. In this equation, K_u is the uniaxial anisotropy of the particle, V is the particle volume, k_B is the boltzman constant, T is the temperature and τ_0 is the attempt time.

$$\tau_N = \tau_0 e^{(\frac{K_u V}{k_B T})}$$

Equation 4-15: Néel-Arrhenius equation.

The criteria for stability in a magnetic recording application is given by the following relationship.

$$\frac{K_u V}{k_B T} > 70$$

Equation 4-16: Criteria for magnetic thermal stability.

If the particle volume becomes too small, K_u can be increased. The field needed to write a bit is given by Equation 4-17:

$$H = \frac{2K_u}{M_S}$$

Equation 4-17: Write field required.

The maximum write field capable is approximately 2.4 Tesla which imposes a limit on the value of K_u and therefore imposes a limit on the highest achievable density.[53, 56, 57]

There are several approaches to overcoming this limit which are outlined below in Figure 4-6. The first is bit patterned recording. Bit patterned recording (BPR) uses media patterned into individual bits, bypassing the need for decreased grain volume to maintain SNR. Each bit can be composed of a single grain, greatly increasing its thermal stability. Bit patterned recording requires advancements in lithography to be successful. Another option is shingled recording which writes overlapping tracks, increasing the density but requiring a more complex writing and reading setup.[58, 59]

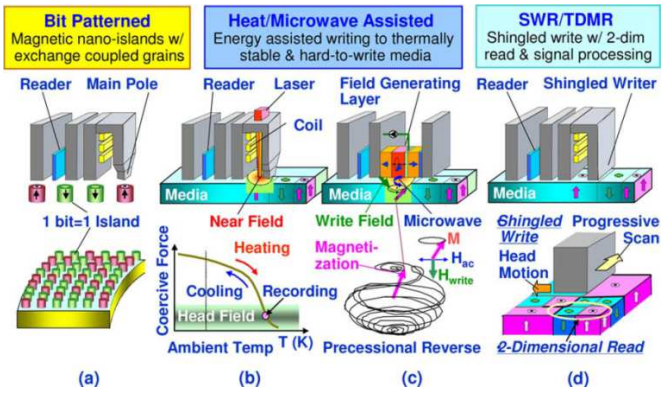

Figure 4-6: Technologies to enable higher recording densities.[59]

Another option, as mentioned above is to use Heat Assisted Magnetic Recording (HAMR). This approach is outlined in Figure 4-7. First, the magnetic media at the spot to be written is heated, which lowers the write field required. For HAMR, the data written is defined by the thermal spot size produced by the near field transducer (NFT) rather than the magnetic spot size produced by the write pole since the thermal spot size is smaller. After the data is written, the head is moved and the media quickly cools to room temperature where it stays thermally stable for permanent storage. By using this technique, media with a higher value of K_u can be used, increasing the thermal stability even though the individual grain size is reduced.[3, 57, 60, 61]

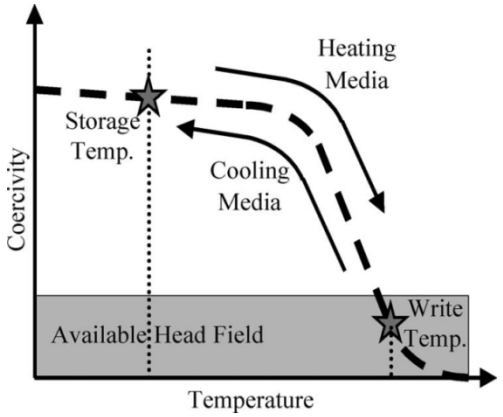

Figure 4-7: Heat Assisted Magnetic Recording procedure.[60]

One of the critical challenges for implementing HAMR is the focusing of energy at the nanoscale. This is where plasmonic resonance can be beneficial. Focusing energy using a beam of light is limited by the wavelength as shown in the Rayleigh criterion below, which determines the minimum spot size based on wavelength, λ, and numerical aperture, NA.

$$d = \frac{.51\lambda}{NA}$$

Equation 4-18: Rayleigh criterion.

This limits spot sizes to a minimum of about 240nm, which is used for blue-ray players, but is far too large for magnetic recording. It is also possible to use a nano-aperture to create a small spot size. However, as shown in Equation 4-19, transmission is very low due to the power of 4 dependence on the ratio of spot size to wavelength.

$$T = (\frac{64\pi^2}{27})(\frac{d}{\lambda})^4$$

Equation 4-19: Transmission through an aperture.

Plasmonic structures can produce high power densities much more focused and efficiently. Plasmonic nanostructures have been demonstrated to be effective for focusing electromagnetic energy to spot sizes as mall as 70nm.

HAMR prototypes have come a long way from lasting "several tens of track recordings" in 2009 to achieving 1 Terabit per square inch recording in 2012 and 1000 write power on hours in 2014.[3, 4, 62] However, there are still obstacles to overcome in order for HAMR to be a successful consumer product. The primary obstacle is reliability, gold near field transducers melt and deform due to high temperatures during operation. New materials offering higher endurance and reliability while maintaining desirable optical properties must be developed as a better understanding of NFT failure are required to meet the exponentially growing demands of data storage. These challenges provide great opportunities for researchers looking to explore the exciting new field of plasmonics.

4.2.3 Characterization

Characterization of plasmonic structures is critical to validating the effectiveness of modeling and fabrication techniques. In addition to traditional

characterization methods such as SEM or AFM which can generate an image of the physical structure of a plasmonic element, there are several techniques capable of evaluating a device's plasmonic characteristics.

One technique, ellipsometry, uses polarized light to measure a material's optical properties. A polarized laser source is reflected off the sample and the shift in polarization phase, Δ, and amplitude, Ψ, due to the light's interaction with the sample. These values are then compared to a mathematical model to fit parameters for index of refraction, n, extinction coefficient, κ, and thickness. Measurements can be taken at a variety of wavelengths and angles to provide enough data to accurately fit the model used as well as to calculate the material's optical properties as a function of wavelength. If a material's optical properties are already known, ellipsometry can also be used to determine its thickness.

It is often useful to relate the index of refraction, n, and extinction coefficient, κ, measured using ellipsometry to the complex permittivity values used to describe plasmon propagation. The complex permittivity is given by Equation 4-20.

$$\varepsilon = \varepsilon' + i\varepsilon'' = (n + i\kappa)^2$$

Equation 4-20: Complex permittivity.

This equation can then be solved for both the real and imaginary terms using the equations below which can be used to calculate surface plasmon propagation length using Equation 4-12.

$$\varepsilon' = n^2 + \kappa^2$$

Equation 4-21: Real part of the complex permittivity.

$$\varepsilon'' = 2n\kappa$$

Equation 4-22: Imaginary part of the complex permittivity.

The ability to derive the complex permittivity through values which are easily obtained using ellipsometry makes this technique very useful for evaluating plasmonic materials.

5 Electrodeposited Galfenol Thin Films

5.1 Introduction

5.1.1 Background and Motivation

Galfenol (FeGa) is a promising technological material because of its valuable magnetic and mechanical properties. Bulk Galfenol has been shown to have magnetostrictive constants of 400 ppm, much larger than most other magnetostrictive materials such as Fe, Co or Ni alloys which have a maximum magnetostriction of 130ppm.[40] In addition, Galfenol has resilient mechanical properties and lower saturation magnetization than Terfenol-D, another giant magnetostrictive material which is very brittle.[43, 63] When compared to other high-magnetostriction materials, like Terfenol-D, Galfenol has lower magnetostriction (400 ppm versus over 1000 ppm) but greatly improved mechanical robustness making it an ideal material for many sensor and actuator applications. Galfenol is ductile and has been reported to have a tensile strength of 440 MPa.[64, 65] This combination of properties makes Galfenol a useful material for sensor and actuator applications and a fascinating topic for materials development.

Electrodeposition of Galfenol offers many advantages over other methods of deposition, including low cost and high deposition rate. It can also deposit material over large areas and or curved surfaces for devices such as integrated torque sensors. Electrodeposition is not a line-of-sight technique as are vacuum deposition processes, so active layers can be grown in situ, for example to fabricate a variety of devices such as acoustic sensors for peristaltic MEMS pumps.[66] In fact, with recent successes in electrodeposition of Galfenol, it may be the only multifunctional material that can be grown in situ. Other giant magnetostrictive materials usually incorporate rare earth alloys, and piezoelectric materials are typically ceramics.

A wide range of devices can be fabricated by taking advantage of galfenol's unique mix of magnetic and mechanical properties. Integrated torque sensors, MEMS pressure sensors, SONAR sensors and even actuators are just some examples of devices which could benefit from a material like galfenol. Some of these applications, such as high aspect ratio nanowire-based transducers, are only realizable through electrochemical deposition of galfenol.

However, there are several difficulties involved with electrodeposition of Galfenol. The first is that the standard reduction potential of gallium is large and negative at -0.56V.[64] In addition, hydrolysis can occur during electrodeposition creating hydrogen bubbles and oxygen rich films. Electrodeposition of gallium has been achieved through induced co-deposition with iron and a complexing agent

such as sodium citrate allowing the development of Galfenol based nanostructures.[67, 68, 69]

5.2 Electrodeposition and characterization

5.2.1 Experimental

There are many difficulties in measuring magnetostriction in electroplated thin films. Good composition and thickness uniformity is required for accurate magnetostriction measurements since the equations for calculating the magnetostriction constant, described in the next section, require that the material is uniform. These measurements also improve with increased film thickness which produces larger deflections and enhanced changes in capacitance resulting in more accurate measurements. However, increased film thickness also increases the chance for delamination due to stress and requires that the Galfenol have very good adhesion to the substrate.

Electrodeposition was carried out using a Gamry potentiostat, model PCI4750-3608. In addition, the system uses a rotating disk electrode, a Gamry RDE 710, capable of rotation rates up to 2000rpm. Above 2000rpm, the fluid flow becomes turbulent. The electrolyte was composed of 0.065M Sodium Citrate, 0.5M sodium sulfate, 0.015M Iron Sulfate and 0.038M Gallium Sulfate adjusted to a pH of 3.75 with Sodium Hydroxide. The experimental setup and deposition mechanism

have been described previously.[16, 64] Samples were deposited at 900rpm and -1.24V versus the reference electrode for 600 seconds.

The substrates used for these measurements were glass coverslips manufactured by Goldseal with dimensions of 18mm by 18mm by 0.13mm thick. Adhesion layers were deposited using a Lesker DC sputter system and film thicknesses were measured using a Nanosurf Mobile S Atomic Force Microscope. Various adhesion layers were tested and delamination was eliminated with Cr/Cu, which provided robust adhesion to the glass substrates used in capacitance bridge measurements.

Magnetostriction was measured using a capacitance bridge system, shown in Figure 4-1. The Galfenol film/ substrate pairs were placed in the system and the capacitance was precisely measured with and without an external magnetic field. When a magnetic field is applied, the amount of deflection is given by Equation 4-5 and can be used to calculate magnetostriction using Equation 4-7, repeated below, along with the sample's mechanical property constant, k, equal to 1.3×10^{-19} F-m for Galfenol.

$$\lambda_m = \frac{k\Delta C}{t_f\left(C_0 - C_{empty}\right)^2}$$

Equation 5-1: Capacitance based magnetostriction measurement.

This setup was verified by measuring a Ni standard sample which showed a magnetostriction constant of -26ppm as expected. An example of these measurements is shown in Figure 5-1.

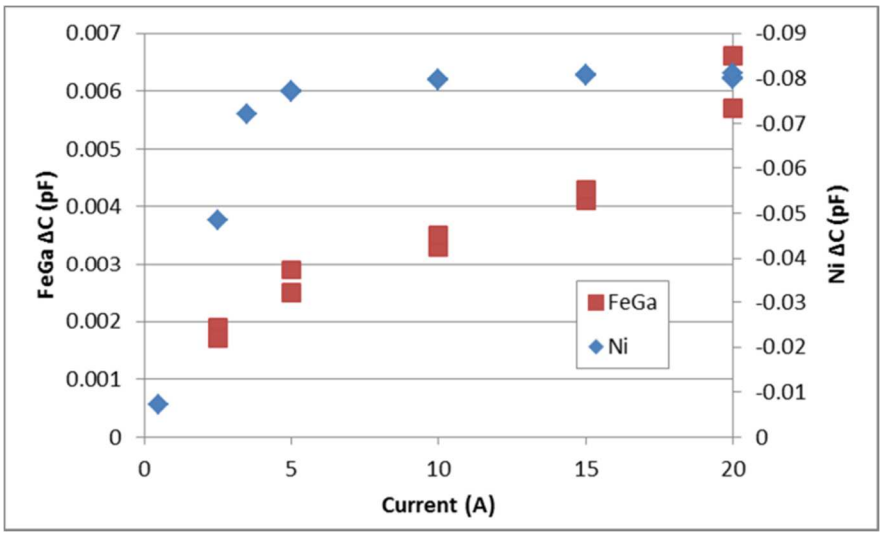

Figure 5-1: Capacitance change used to calculate Ni and GaFe magnetostriction.

This figure shows the measured change in capacitance as a function of current in the electro-magnet. The Ni film shows a much clearer signal than the FeGa because it is much thicker (1.9μm versus 170nm) and has a larger Young's modulus. In addition, the Ni sample shows a negative ΔC due to its negative magnetostriction constant. This data also shows the saturation behavior of the magnetic films.

5.2.2 Results and Discussion

Development of reliable seed layers was one of the most important prerequisites to accurate measurements of magnetostriction in Galfenol. Galfenol

thin films are especially susceptible to delamination because of the large stresses and strains during deposition and measurement.

Initially, titanium/ copper seed layers were used. However, delamination was observed due to poor adhesion between the Ti and glass substrate layers. A Cr/ Cu seed layer showed greatly improved adhesion. Cr was sputtered at 200W and 10mtorr of Ar for 10 minutes while Cu was deposited at 200W and 10mtorr for 30 minutes. The total thickness of adhesion layer and seed was measured to be 540nm. These films showed good adhesion to the glass coverslips.

Uniform films were required for accurate magnetostriction measurements. Non-uniformity was measured by taking thickness measurements at 10 locations distributed across the substrate. This gave an average deposition rate of 14.8nm/min with a standard deviation of 1.7nm/min across the sample. Compositional uniformity was also measured by taking EDS measurements at 7 locations across the sample, some as close as 1mm to the edge. These results showed a very uniform composition with an FeGa atomic ratio of 83 parts Fe to 17 parts Ga with a standard deviation of only 1.04 parts.

Rotating Disk Electrochemistry was used to achieve this result. RDE produces a uniform electrolyte boundary layer across the entire substrate which is independent of the radial position according to Equation 2-16. This equation shows

that the boundary layer, δ, is proportional to the inverse square root of the rotation rate (ω) as well as the cube root of the diffusion constant (D) and importantly is independent of position on the sample. In addition to providing uniform films, RDE allows us to vary the composition of the deposited films by controlling the mass transfer rates of the ions in solution. The samples were mounted using copper tape on a stainless steel holder to minimize any bending of the sample during deposition as well as to serve to improve uniformity.

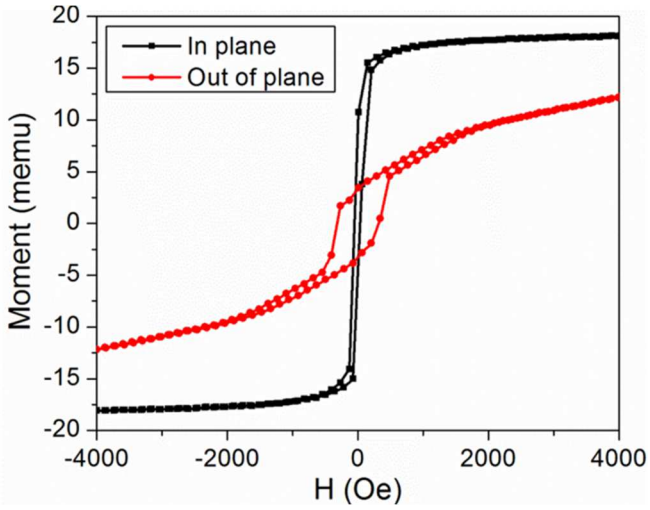

Figure 5-2: VSM measurements of Galfenol.

Figure 5-2 shows magnetization hysteresis (MH) loops of a 148nm thick Galefenol (Fe83Ga17) film when the field was applied in plane and perpendicular to the plane of the film. The in-plane and out-of-plane coercivities were measured to be 61Oe and 343Oe, respectively, with the easy axis magnetization lying in plane of

the film. The saturation magnetization was then estimated, using the volume of the sample, to be 1520 emu/cm^3 which is reasonable for an 82% iron film.

Initial magnetostriction measurements showed a value of approximately 140 ppm for $Fe_{83}Ga_{17}$. This value is lower than bulk Galfenol created by quenching, but comparable to other reported values for thin film Galfenol of the same composition deposited by magnetron sputtering.[40, 64, 70] Figure 5-1suggests that our electrochemically deposited Galfenol films may not have completely saturated during measurement and that the value of saturation magnetization could be even higher. In addition, magnetostriction could perhaps be further increased by annealing our Galfenol thin films. The specific composition was chosen to target the observed peak in magnetostriction value seen in both sputtered and bulk films at around 18% Ga.

A measured magnetostriction value of 140 ppm shows that electrodeposition is a viable deposition technique for magnetostrictive Galfenol and comparable to sputtered films. However, electrodeposition also has several advantages over other methods of deposition, such as the ability to deposit in situ thin films and nanowire structures, which make this deposition process potentially valuable for MEMS applications.

These results, for the first time, show magnetostriction in electrodeposited Galfenol thin films. There are several difficulties associated with electrodeposition and measurement of Galfenol including delamination due to stress and non-uniformity. However, we were able to overcome these issues by improving our adhesion layer process with a Cr/ Cu layer. In addition, a rotating disk electrode was used during deposition to not only control the composition of the deposited films, but also provide uniform deposition conditions across the substrate. These results show that Galfenol can be deposited using electrodeposition and values for magnetostriction similar to those of sputtered Galfenol thin films can be achieved.

5.3 Effect of Composition and Crystallinity

5.3.1 Experimental

Previously, we have shown electrodeposition of magnetostrictive galfenol thin films.[1, 68] Electrodeposition allows Galfenol to be easily integrated into a variety of applications, such as torque sensors with conformal, monolithic active layers. Highly uniform (standard deviation of 10% for thickness and 1% for composition) thin films have been produced using electrodeposition as well as extremely high aspect ratio nanowire structures. These results demonstrate the viability of electrodeposited galfenol for use in MEMS.

Electrodeposition was performed using a rotating disc electrode plating cell. Rotating disc electrochemistry is useful for achieving highly uniform thin films due to creating a uniform hydrodynamic boundary condition across the surface of the substrate. This cell consists of a Teflon and stainless steel sample holder capable of rotating at speeds up to 1000 rpm, a platinum coated titanium mesh anode and a potassium chloride (KCl) reference electrode.

The electrolyte used in these experiments was composed of 0.5 M sodium sulfate (Na_2SO_4), 0.075 M gallium(III) sulfate ($Ga_2(SO_4)_3$), 0.015 M iron(II) sulfate ($FeSO_4$) and 0.065 M sodium citrate. pH was adjusted to 3.75 using sulfuric acid,

H_2SO_4. The sodium sulfate serves as a supporting electrolyte to improve the conductivity of the solution while the sodium citrate complexes the iron and gallium ions to prevent oxidation.

The substrates used were Goldseal glass coverslips (dimensions 18 x 18 x 0.13 mm3) with a sputtered chrome/copper adhesion layer.[1] Compositions were measured using Energy Dispersive X-Ray Spectroscopy (EDS) on a JEOL 6500. Crystallographic measurements were made using a Bruker D8 Discover.

Magnetostriction was measured using the capacitance bridge method discussed previously. Substrates were mounted as one half of a parallel plate capacitor which allowed us to measure a capacitance change when a magnetic field was applied. The change in capacitance is related to the deflection due to magnetostrictive strain in the thin films. This technique was confirmed by measuring a thin film nickel standard sample.

5.3.2 Results and Discussion

Initially, electrochemical measurements were performed to determine the approximate deposition potential corresponding to iron-gallium alloy electrodeposition. These results are shown in Figure 5-3. Linear Sweep Voltametry (LSV) measures deposition current as a function of applied potential to determine

the point at which reduction occurs. For the convention used in these measurements, negative current values correspond to reduction. 4 different surfaces were studied using this technique including solid carbon, solid platinum, copper coated platinum similar to the surface of our seed layer at the start of the deposition and Galfenol coated platinum similar to the surface of our samples during electrodeposition.

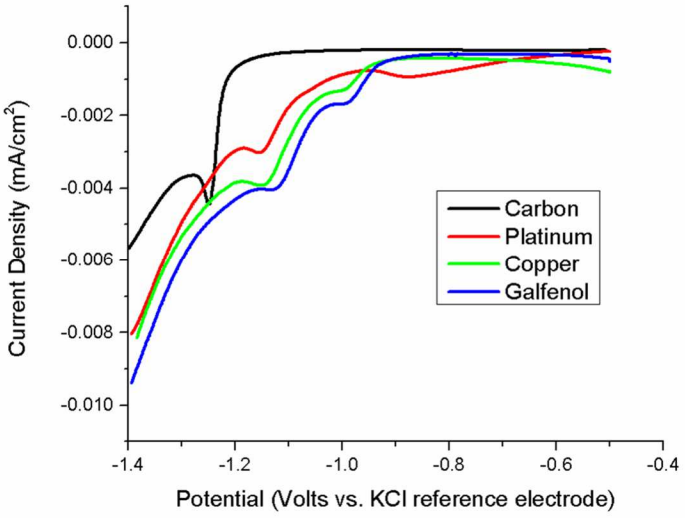

Figure 5-3: Galfenol Linear Sweep Voltametry results.

The results show that deposition potentials around -1.2V versus the KCl reference electrode should produce iron-gallium alloys. Electrodeposition at potentials far below this value do not result in reduction while electrodeposition at around -1.3V or higher causes electrolysis of the water and supporting electrolyte which results in rough, non-uniform oxide rich films. The results in Figure 5-3 also

show that the reduction potential is dependent on the substrate. Electrodeposition on a metallic substrate, such as copper or platinum, should be carried out at a less negative potential than on carbon.

Thin films were deposited at potentials in the range of -1.1V to -1.3V versus the reference electrode. Composition, as measured using EDS, as a function of deposition potential is shown in Figure 5-4. These results show the capability to deposit galfenol thin films over the range of 10-40% gallium using a single electroplating solution. This composition range corresponds to the highest expected magnetostriction values observed in single crystal iron-gallium alloys.[40]

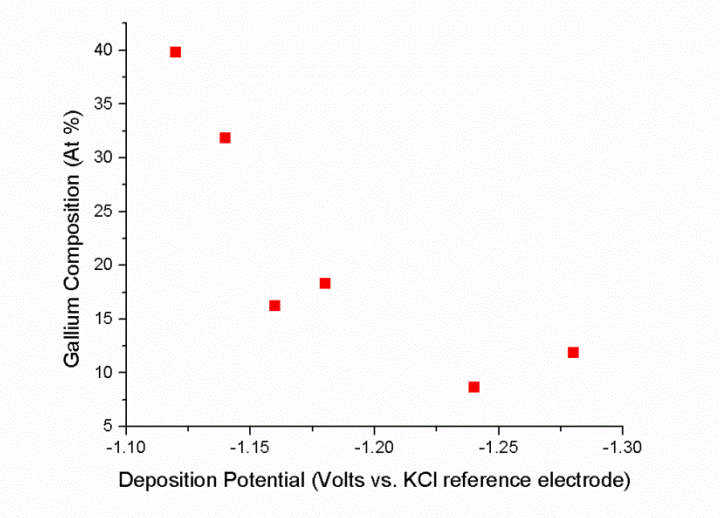

Figure 5-4: Galfeonol composition as a function of deposition potential.

Magnetostriction values for these films were measured using the capacitance bridge method described in the previous section and are shown in Figure 5-5 along

with single crystal galfenol magnetostriction values reported in literature.[40] These results show that while our electrodeposited galfenol thin films show relatively large magnetostriction of approximately 100ppm, they have significantly lower magnetostriction than bulk single crystal samples. This is due to the polycrystalline nature of our electrodeposited films.

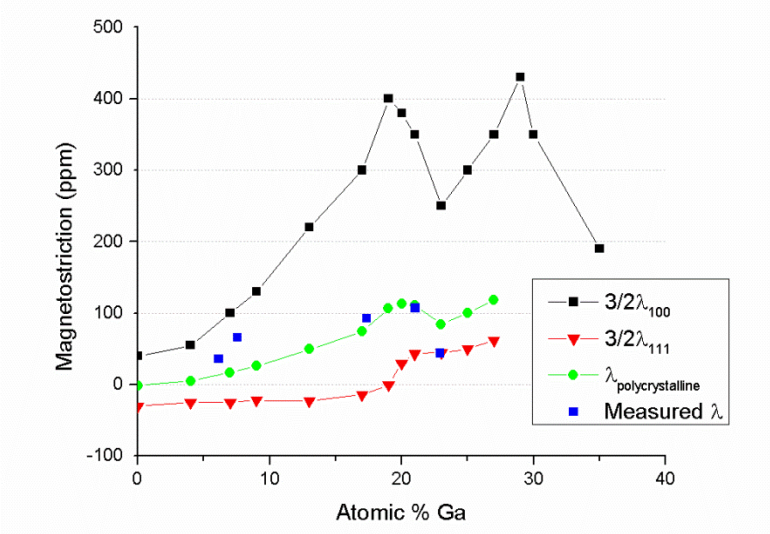

Figure 5-5: Galfenol magnetostriction versus composition from literature, calculations and measurements.

X-ray Diffraction measurements show that our films are fully polycrystalline. A Bruker D8 Discover 2D with a Cu α source was used to analyze a 100nm thick $Fe_{83}Ga_{17}$ sample. These results are shown in Figure 5-6. The peak at 44.4 degrees corresponds to the (110) orientation in BCC iron. The other peaks observed are due to the copper adhesion layer used in these experiments. The uniformity of the

measurement in the Phi direction indicates that our films are polycrystalline which has a significant effect on the net magnetostriction of our films.

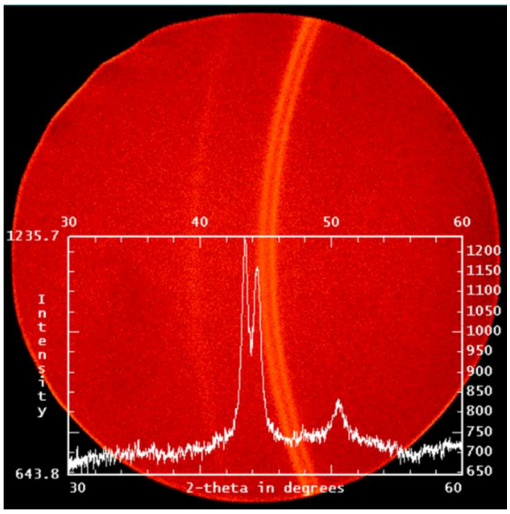

Figure 5-6: XRD measurement of electrodeposited galfenol.

These results can be used to calculate the expected magnetostriction value of our polycrystalline thin films. When the measured magnetostrictive strain is in the same direction as the magnetization, as is the case with our measurement setup, the magnetostriction of the sample is given by Equation 4-2, repeated below, which for a polycrystalline sample is equal to $(2\lambda_{100}+3\lambda_{111})/5$. This derived value is plotted in Figure 5-5 as a function of composition using values for λ_{100} and λ_{111} from literature.[71]

$$\lambda_{Si} = \frac{3}{2}\lambda_{100}\left(\alpha_1^4 + \alpha_2^4 + \alpha_3^4 - \frac{1}{3}\right) + 3\lambda_{111}(\alpha_1^2\alpha_2^2 + \alpha_2^2\alpha_3^2 + \alpha_3^2\alpha_1^2)$$

Equation 5-2: Magnetostriction in a cubic material.

When the polycrystalline nature of our thin films is accounted for, the observed magnetostriction values line up much more closely to the expected results. This quick calculation explains why our electrodeposited films show lower magnetostriction than the single crystal values. While the measured values are not as large the maximum magnetostriction observed in single crystal galfenol, they are still large compared to other magnetostrictive elements and alloys and show that electrodeposited galfenol can be a useful material for MEMS applications requiring large magnetostriction.

These results show that electrodeposition can produce magnetostrictive galfenol films suitable for MEMS and sensor applications. By controlling the deposition parameters, we are able to vary the composition of our films and produce alloys with the largest expected magnetostriction. By accounting for the polycrystallinity of our films, we are able to explain the observed magnetostriction values. In addition, the deposited films are highly uniform in both thickness and composition.

While our galfenol thin films demonstrate lower magnetostriction than bulk samples, electrodeposited galfenol can be more easily integrated into MEMS transducers than bulk single crystal galfenol pieces. This makes electrodeposited galfenol a useful material for the creation of a wide range of devices.

6 Gold thin films for HAMR

6.1 Introduction

Heat Assisted Magnetic Recording (HAMR) is a technology which promises to further increase hard disk drive capacities to meet the exponentially increasing demand for data storage. However, while HAMR has made incredible progress in reliability with lifetimes of the gold Near Field Transducer (NFT) used to focus the electromagnetic energy used for writing increasing from "several tens of track recordings" in 2009 to over 1000 power on hours in 2014, reliability is still the limiting factor preventing this new technology from being fully commercialized.[3, 4] Greater understanding is needed of the gold deposition process as well as the process by which NFTs fail due to thermal deformation.

Electrodeposited gold and gold alloys show promise for this application because they are not damaged by ion bombardment during patterning and can be widely modified through varying bath composition and deposition parameters. Advanced characterization processes using Electron Back Scatter Diffraction (EBSD) were also developed to analyze thin film crystal structure and its role in NFT stability. These results will hopefully contribute to the successful implementation of HAMR as well as improve plasmonic device reliability in other applications.

6.2 Gold electrodeposition mechanism and stability

Electrodeposition of gold is the metallization process of choice for interconnects and electrical contacts in compound semiconductors, as well as optoelectronic and biomedical applications as described in recent reviews.[72, 73, 74, 75] In addition to useful electrical properties, gold also shows excellent plasmonic properties at room temperature, but is susceptible to deformation caused by high energy densities encountered in plasmonic devices.[76]

Traditional cyanide-based gold plating solutions are becoming increasingly unpopular due to toxicity concerns, including possible liberation of toxic HCN gas during reactions with acids, worksite safety and effluent treatment. Excess cyanide ions, liberated during electrochemical reduction of the $Au(CN)_2^-$ complex, can attack photoresist, resulting in lift-off of the resist and deposition of extraneous gold underneath the resist.[75, 77, 78, 79] In order to address these shortcomings, new non-cyanide based solutions including sulfite, thiosulfate and mixed sulfite-thiosulfate along with organic additives as solution-stabilizers have been evaluated. Compared to cyanide, these non-cyanide electrolytes are environmentally friendly, but suffer from SO_2 and colloidal sulfur formation in neutral and acidic media. Thiosulfate plating solutions are unstable under neutral and acidic conditions due to thiosulfate

decomposition and formation of colloidal sulfur from the reaction shown in Equation 6-1.[74]

$$S_2O_3^{2-} \leftrightarrow S_0 + SO_3^{2-}$$

Equation 6-1: Colloidal sulfur formation under neutral conditions.

Colloidal sulfur is also formed by the protonation of excess $S_2O_3^{2-}$ ions according to Equation 6-2.

$$H^+ + S_2O_3^{2-} \leftrightarrow S_0 + HSO_3$$

Equation 6-2: Colloidal sulfur formation under acidic conditions.

The precipitation of colloidal sulfur from thiosulfate complexes is catastrophic when it occurs in an industrial electrodeposition tool. The addition of sulfite into the thiosulfate solution drives the equilibriums of Equation 6-1 and Equation 6-2 to the left, thereby preventing the formation of colloidal sulfur.[80]

A mixed electrolyte solution containing thiosulfate-sulfite ions was proposed by T. Osaka and coworkers as a stable plating solution.[81] In addition, S. Roy and coworkers have demonstrated the bath stability of a thiosulfate-sulfite plating solution.[80] They thoroughly studied the electrochemical behavior as well as the solution chemistry and stability of gold complexes in the thiosulfate-sulfite solution.[80, 82, 83] However, to the best of our knowledge, a gold electrodeposition process from mixed thiosulfate-sulfite plating solution has not yet been commercialized.

Electrodeposition of gold from a basic thiosulfate-sulfite solution containing 0.02M $Na_3Au(S_2O_3)_2$ has been investigated on Au and Pt electrodes using various electroanalytical techniques including cyclic voltammetry (CV), linear sweep voltammetry (LSV) and rotating disk electrodeposition (RDE). The voltammograms for gold deposition on the Au electrode were significantly different from those on Pt indicating that the electron transfer was influenced by the coupled chemical reaction. It was proposed that irreversible one electron reduction to gold at the Pt electrode starts from $Au(S_2O_3)(SO_3)_2^{5-}$, a mixed gold thiosulfate–sulfite complex with a high stability constant ($\log \beta = 30.8$). A diffusion coefficient of 1.77×10^{-6} cm^2/s for $Au(S_2O_3)(SO_3)_2^{5-}$ was calculated from the slope of the i_p versus $v^{1/2}$ obtained with a Pt electrode.

6.2.1 Experimental

Voltammetric measurements were performed in a 100 ml cell using either a Pt or Au disk working electrode (1 cm^2 area), a glassy carbon counter electrode and a saturated calomel electrode (SCE) reference electrode. The Au electrode was cleaned in concentrated HNO_3 for 10 s while the Pt electrode was cleaned using a KI/ I_2 solution for 30 s followed by rinsing with acetone and water. Potential-current and chronoamperometry curves were recorded with a rotating disk electrode (RDE) using a Gamry Instruments PC3 potentiostat and Gamry RDE710

rotator. The composition of gold thiosulfate-sulfite plating solution used for both voltammetric measurements and deposition of thin films was 0.02 M $Na_3Au(S_2O_3)$, 0.42 M $Na_2S_2O_3$ and 0.42 M Na_2SO_3 at pH 8.0.

Thin film depositions were carried out using a rotating disk in a small cell (150 ml) equipped with a graphite anode and SCE reference electrode. The substrates were Si wafers with vacuum deposited 10 nm Au seed layers which were mounted tightly fitted over the flat end of the rotating electrode with an exposed area of 3 cm^2.

6.2.2 Results and discussion

It has been shown that the standard electrode potential of Au^+-complexes becomes more negative as the stability constant increases. The formation of two mixed-ligand species, $Au(S_2O_3)(SO_3)^{3-}$ and $Au(S_2O_3)(SO_3)_2^{5-}$, with highest stability constants ($\log \beta$ = 27.1 and 30.8 respectively), were detected recently using Raman and potentiometric experiments.[84] It was shown experimentally by A. Sullivan and P. Kohl that the addition of sulfite into the gold thiosulfate solution shifts its reduction potential negatively.[85] This was taken as an indication of the formation of a mixed gold thiosulfate-sulfite complex. T. Green and S. Roy published the equilibrium reactions of common Au^+ complexes along with their stability constants, two of which are shown in Equation 6-3 and Equation 6-4 below.[79]

$$Au^{+} + S_2O_3^{2-} + SO_3^{2-} = Au(S_2O_3)(SO_3)^{3-} \quad (\log \beta = 27.1)$$

Equation 6-3: $Au(S_2O_3)(SO_3)^{3-}$ formation.

$$Au^{+} + S_2O_3^{2-} + 2SO_3^{2-} = Au(S_2O_3)(SO_3)_2^{5-} \quad (\log \beta = 30.8)$$

Equation 6-4: $Au(S_2O_3)(SO_3)_2^{5-}$ formation.

In a basic thiosulfate-sulfite solution at pH 8.0 the most dominant Au^{+}-complex is $Au(S_2O_3)(SO_3)_2^{5-}$. Figure 6-1 shows a multicyclic voltammogram of this complex in a thiosulfate-sulfite solution using a Au electrode. Scans were performed using a bath with 0.047 M $Na_3Au(S_2O_3)_2$ in a supporting electrolyte of 0.42 M $Na_2S_2O_3$ + 0.42 M Na_2SO_3 at pH 8.0. The sweep rate was 20 mV/s and the electrode area was 1 cm^2.

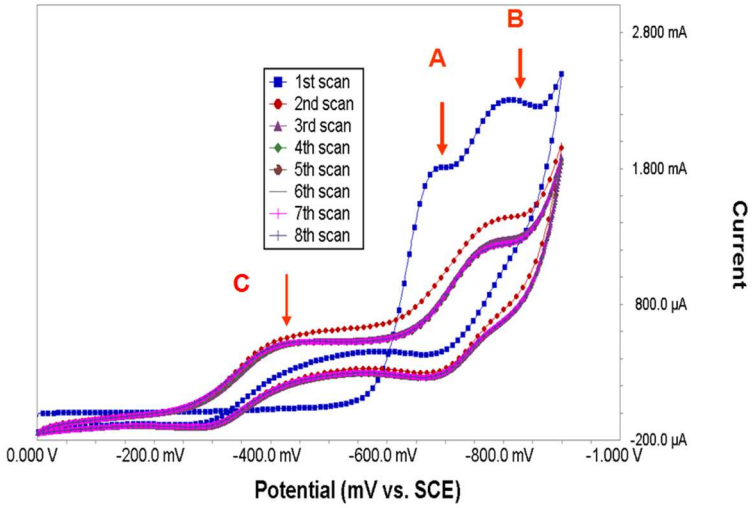

Figure 6-1: Multicyclic voltammogram with Au electrode.

The first cathodic wave (Peak A) with *E*p= -650 mV vs. SCE corresponds to the one electron reduction to gold from the complex shown in Equation 6-4.

$$Au(S_2O_3)(SO_3)_2^{5-} + e^- \rightarrow Au + S_2O_3^{2-} + 2SO_3^{2-}$$

Equation 6-5: Proposed method of Au reduction.

The second cathodic wave (Peak B) with *E*p around -750 mV vs. SCE could be attributed to the reduction of the adsorbed SO_3^{2-} giving rise to a dithionite ion according to the following equation.

$$2SO_3^{2-} + 2e^- + 2H_2O \rightarrow S_2O_4^{2-} + 4OH^-$$

Equation 6-6: Reduction of adsorbed SO_3^{2-} to dithionite.

The results in Figure 6-1 demonstrated that on the reverse of the first scan there is a characteristic nucleation loop where the cathodic current is higher on reverse scan than on the forward one. After the nucleation potential (around -600 mV vs. SCE) a new reduction wave (Peak C) in the potential range from -600 to -250 mV vs. SCE appeared, presumably corresponding to the reduction of the $Au_2S_2O_{3ads}$ intermediate through two electron transfer as shown in Equation 6-7.

$$Au_2S_2O_{3ads} + 2e^- \rightarrow 2Au + S_2O_3^{2-}$$

Equation 6-7: Au reduction from $Au_2S_2O_{3ads}$.

T. Osaka et al. in their study of the mechanism of sulfur inclusion during gold electrodeposition from a thiosulfate-sulfite solution proposed $Au_2S_2O_3$ as an adsorbed species on the gold surface from the diffusing $Au(S_2O_3)_2^{3-}$ complex followed by its electrochemical reduction according to Equation 6-7.[86] Two electron reduction of $Au_2S_2O_{3ads}$ in Equation 6-7 is probably occurring in two steps

in which the $AuS_2O_3^-$ intermediate ($\log \beta = 10.4$) formed during the first electron transfer is reduced at a more positive potential. During the second and following scans Peak A disappears while Peak B and C remained practically unchanged.

Linear sweep voltammograms recorded using Au and Pt electrodes at various sweep rates, ν, are shown in Figure 6-2 below. The cyclic voltammograms run using a Pt electrode showed a peak at a more negative potential, compared to the Au electrode which corresponds to one electron reduction according to Equation 6-5. The shift in deposition potential at the Pt electrode is probably related to the larger nucleation potential on Pt than on Au.[87]

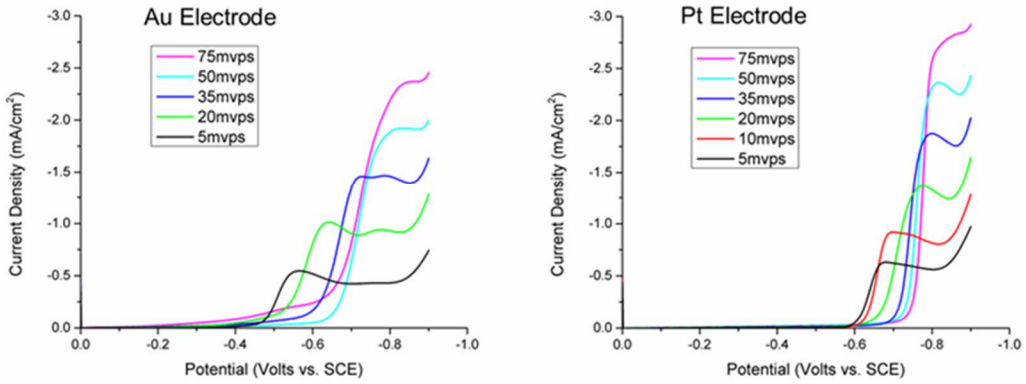

Figure 6-2: Linear sweep voltagrams using Au and Pt electrodes.

The peak potential (peak A) corresponding to the one electron reduction of the gold complex shifted negatively with the increase of sweep rate on both substrates. In addition, the plot of peak current density, i_p versus $\nu^{1/2}$, is linear which indicates that the reaction in Equation 6-5 is electrochemically irreversible.

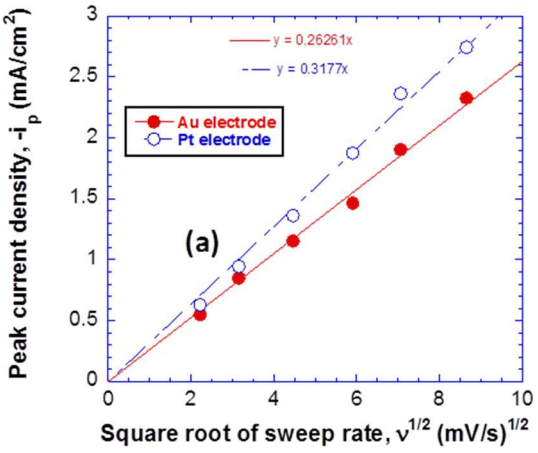

Figure 6-3: Plot of peak current density versus sweep rate.

The plot of i_p versus $v^{1/2}$ is shown in Figure 6-3 along with its linear regression which passes through the origin indicating that the electrode reaction in Equation 6-5 is diffusion controlled. The slope of the i_p versus $v^{1/2}$ plot obtained from the Au electrode in Figure 6-3 is smaller than that obtained from the Pt electrode.

The diffusion coefficient for $Au(S_2O_3)(SO_3)_2^{5-}$ was calculated from the slope of the linear plot obtained using the Pt electrode, according to the Randles-Sevcik equation shown Equation 2-19 and again below.

$$i_p = 2.6 \times 10^2 n^{3/2} \sqrt{D} c_0 \sqrt{v}$$

Equation 6-8: Peak current as a function of sweep rate.

The above equation gives a value of D = 1.77 x 10^{-6} cm^2/s. This value is lower than the literature value of the diffusion coefficient (D = 7.0 x 10^{-6} cm^2/s) obtained for the $Au(S_2O_3)_2^{3-}$ complex from its linear i_p versus $\nu^{1/2}$ plot which may be explained by the larger size of the hydrated $Au(S_2O_3)(SO_3)_2^{5-}$ complex compared to $Au(S_2O_3)_2^{3-}$ complex.

Rotating Disk Electrode (RDE) voltammetry measurements were performed using a Pt electrode in the thiosulfate-sulfite solution at pH 8.0. Rotation rates were varied from 25 rpm to 500 rpm while sweep rate was held at 5 mV/s. The slow sweep rate ensured that the platinum surface was covered with a layer of deposited gold during the rising portion of the curve. Figure 6-4 shows the limiting current density at -0.7 and -0.75 volts versus SCE as a function of rotation rate in $\omega^{1/2}$.

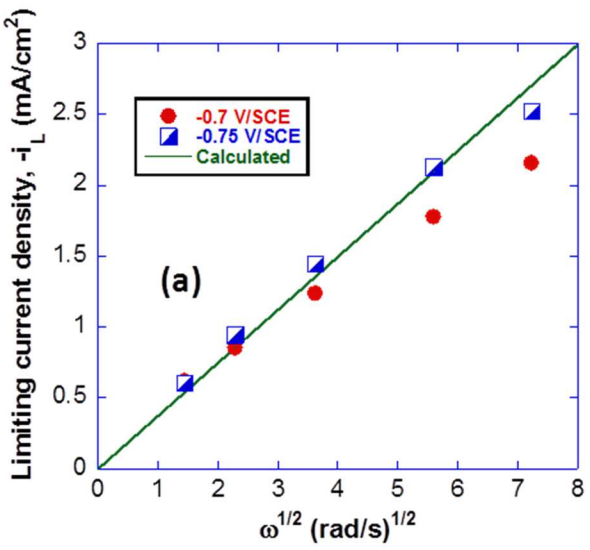

Figure 6-4: Limiting current density versus RDE rotation rate.

In the case of an entirely diffusion-controlled process, the limiting density is given by the Levich equation shown previously in Equation 2-17 and repeated below.

$$i = -0.62nF\frac{D^{2/3}\omega^{1/2}c_0}{\nu^{1/6}}$$

Equation 6-9: The Levich equation for current during RDE deposition.

In the above equation, n is the number of electrons involved in the reaction, F is the Faraday constant, c_0 is the bulk concentration of the diffusing species, D is the diffusion coefficient, ν is the kinematic viscosity in cm^2/s and ω is the angular rotation rate in radians/s. A plot of i vs $\omega^{1/2}$ should be linear and pass through the origin, from such a plot the diffusion coefficient can be estimated using the Levich equation.

Figure 6-4 shows the experimental limiting current densities measured at two potentials, -0.70 V and -0.75 V versus SCE. The limiting current density increases linearly with the square root of rotation rate at both potentials but does not pass through the origin.

We have calculated the apparent number of transferred electrons, n_{APP}, from the i versus $\omega^{1/2}$ plot in Figure 6-4 using the Levich equation for n = 1 and c_0 = 2.0 x 10-5 mol/cm^3. For the diffusion coefficient we used the previously calculated value of D = 1.77 x 10^{-6} cm^2/s from the i_p versus $\nu^{1/2}$ plot shown in Figure 6-3. The current

function for the calculated limiting currents, $i/\omega^{1/2}$, is independent of rotation rate corresponding to n_{APP} = 1.0. The value of n_{APP} was calculated as a ratio of experimental to calculated *i* values according the following equation.

$$n_{APP} = \frac{(i/\omega^{1/2})_{experimental}}{(i/\omega^{1/2})_{calculated}}$$

Equation 6-10: Apparent number of transferred electrons.

The apparent number of transferred electrons decreases with the increase of rotation rate.

These results indicate that the limiting current is dependent on both kinetics and mass transport. There are at least three possible chemical reactions coupled to the electron transfer which can influence the concentration of the diffusing $Au(S_2O_3)(SO_3)_2^{5-}$ complex at the electrode surface and influence the i - $\omega^{1/2}$ relationship. The first equilibrium equation is depicted in Equation 6-4. We can rule out its influence since it has been demonstrated that the total concentration of the $Au(S_2O_3)(SO_3)_2^{5-}$ complex in a basic solution at pH 8.0 is 100 % and the equilibrium is shifted toward the right.[79] The second proposed equilibrium is the dissociative reaction of $Au(S_2O_3)(SO_3)_2^{5-}$ at the gold surface leading to adsorbed $Au_2S_2O_3$ and SO_3^{2-} species shown in Equation 6-11.

$$2Au(S_2O_3)(SO_3)_2^{5-} = Au_2S_2O_{3ads} + 4SO_3^{2-}{}_{ads} + S_2O_3^{2-}$$

Equation 6-11: $Au(S_2O_3)(SO_3)_2^{5-}$ dissociation.

The adsorbed SO_3^{2-} is reduced at a more negative potential. In the third reaction depicted in Equation 6-12, diffusing $S_2O_3^{2-}$ ions react at the electrode surface with adsorbed $Au_2S_2O_3$ releasing the $Au(S_2O_3)_2^{3-}$ complex into the solution.

$$Au_2S_2O_{3ads} + 3S_2O_3^{2-} = 2Au(S_2O_3)_2^{3-}$$

Equation 6-12: Adsorbed Au2S2O3 dissolved by S2O32- ions.

It was proposed that irreversible one electron reduction to gold at the Pt electrode in a thiosulfate-sulfite plating solution starts from the mixed gold thiosulfate–sulfite complex with the highest stability constant (log β = 30.8), $Au(S_2O_3)(SO_3)_2^{5-}$. The diffusion coefficient of $Au(S_2O_3)(SO_3)_2^{5-}$ was calculated from the slope of the linear i_p versus $\nu^{1/2}$ plot obtained using a Pt electrode and found to be D = 1.77 x 10^{-6} cm^2/s, which is lower than the value of diffusion coefficient (D = 7.0 x 10^{-6} cm^2/s) obtained for the $Au(S_2O_3)_2^{3-}$ complex. Cyclic voltammograms for gold deposition using a Au electrode were significantly different from those on Pt indicating that the electron transfer was influenced with the coupled chemical reaction.

Three electroactive species observed on cyclic voltammograms at the Au electrode were attributed to $Au(S_2O_3)(SO_3)_2^{5-}$ (Peak A), $SO_3^{2-}{}_{ads}$ (Peak B) and $Au_2S_2O_{3ads}$ (Peak C).

RDE voltammetry results indicate that the limiting current is dependent on both kinetics and mass transport. There are several possible chemical reactions coupled to the electron transfer which can influence the concentration of the diffusing $Au(S_2O_3)(SO_3)_2^{5-}$ complex at the electrode surface and therefore have an influence on the i - $\omega^{1/2}$ relationship. The most important is the equilibrium generated through the gold-surface catalyzed chemical dissociation reaction of the most stable $Au(S_2O_3)(SO_3)_2^{5-}$ complex seen in Equation 6-11.

6.3 Gold alloys

6.3.1 Background and motivation

Heat Assisted Magnetic Recording presents an incredible materials challenge. While prototype demos have been successful, a dramatic increase in device reliability is required for HAMR to be a successful consumer technology.[3, 62] Initial demos lasted only "several tens of track recordings" in 2009 and have progressed quickly with a 1 Terabyte per square inch demo shown at TMRC in 2012 and the announcement of 1000 write power on hours in 2014.[3, 4, 62] The extreme energy densities encountered in this application can reach 10 MW/ cm^3 due to the plasmonic confinement. High temperatures due to this energy density can cause recrystallization and deformation in gold nanoparticles and failure in the Near Field Transducer (NFT) used in HAMR.[76]

NFT materials are typically deposited using vacuum based processes, however electrodeposition can potentially provide benefits over conventional sputtered films. Electrodeposited structures do not have sidewall ion damage from patterning which can lead to device failure.[88] In addition, sulfur inclusion during electrodeposition can increase the hardness of the gold. However, these benefits must be weighed against a reduction in surface plasmon quality factor observed in

electrodeposited gold films. A non-cyanide based gold electrodeposition process has been investigated which would be compatible with industry standards.[5, 80, 81]

Electrodeposition also allows for more rapid evaluation of plasmonic alloys. Alloys can be deposited using relatively small volumes and inexpensive solutions which could then be scaled up if results are successful. Grain refinement can be achieved through alloying which has the potential to create more robust gold films according to the Hall-Petch relationship shown in Equation 2-7.[46] Alloying can also be used to tune the resonance between that of pure gold and pure silver.[89]

6.3.2 Experimental

Electrochemical experiments were carried out in a 100 ml cell using a Pt disk working electrode (1 cm^2 area), a Pt mesh counter electrode and a saturated calomel electrode (SCE) reference electrode. The electrode was cleaned using a KI/ I_2 solution for 30 s followed by rinsing with acetone and water. Linear Sweep Voltammetry (LSV) measurements were taken with a rotating disk electrode (RDE) using a Gamry Instruments PC3 potentiostat and Gamry RDE710 rotator. The plating solution used for both voltammetric measurements and deposition of thin films was composed of $Na_3Au(S_2O_3)$ along with a 0.4 M $Na_2S_2O_3$ and 0.4 M Na_2SO_3 supporting electrolyte at pH 8.0.[5] Additional concentrations of $NiSO_4$, $CuSO_4$ and $KAg(CN)_2$ were added for the investigation of alloys.

Thin film depositions were carried out using a rotating disk in a small cell (150 ml) equipped with a Pt mesh anode and SCE reference electrode. The substrates were Si wafers with vacuum deposited 10 nm Au seed layers which were mounted tightly fitted over the flat end of the rotating electrode with an exposed area of 3 cm^2.

Linear Sweep Voltammetry (LSV) was performed to investigate the reduction potentials of the complexed Au, Ag, Ni and Cu ions. Figure 6-5 shows the results of LSV measurements performed at 125 rpm with separate solutions of 0.02 M metal ions in a Sulfite-Thiosulfate supporting electrolyte.

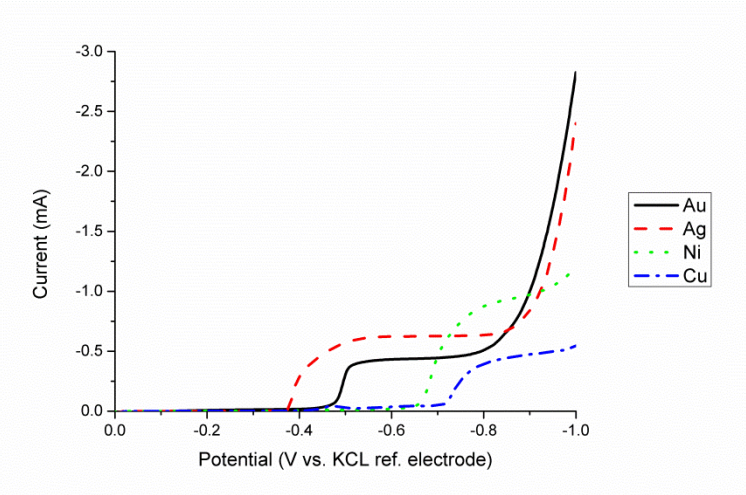

Figure 6-5: Linear Sweep Voltametry results for Au, Ni, Cu and Ag.

From the LSV results above, the steady state currents, i_{SS}, along with the half potentials, $E_{1/2}$, for each metal in our supporting electrolyte were calculated. These results are shown below in Table 6-1.

Metal	i_{SS} (mA/cm²)	$E_{1/2}$ (V)
Au	-0.436	-0.494
Ni	-0.947	-0.702
Cu	-0.476	-0.746
Ag	-0.623	-0.406

Table 6-1: Au, Ni, Cu and Ag LSV results.

The results show that Ag has the lowest reduction potential, followed by Au while Ni and Cu have relatively large reduction potentials.

These results were used to develop a preliminary AuAgCu plating bath with a composition of 0.04 $Na_3Au(S_2O_3)$, 0.003 M $KAg(CN)_2$ and 0.001 M $CuSO_4$ along with a 0.4 M $Na_2S_2O_3$ and 0.4 M Na_2SO_3 supporting electrolyte at pH 8.0 At low current densities, materials with low reduction potentials such as Au and Ag are preferentially deposited, while at high current densities, Au and Ag ions become depleted resulting in the presence of more Cu in the deposited alloy. The bath composition was chosen to produce a range of films composed primarily of Au and Ag due to their superior plasmonic properties with 0 to 5 % Cu for improved alloy integrity.

6.3.3 Results and discussion

Electrodeposition offers a wide range of tunable deposition parameters including bath composition, deposition current density and rotation rate. Thin film

samples with a target thickness of 100 nm were deposited using the bath composition described above over a range of current densities at 0 and 125 rpm. Compositions were measured using Energy Dispersive X-Ray Spectroscopy (EDS) on a JEOL JSM-6610LV with an Oxford Instruments Inca X-Act EDS. Thicknesses were verified using a KLA-Tencor P-16 surface profilometer.

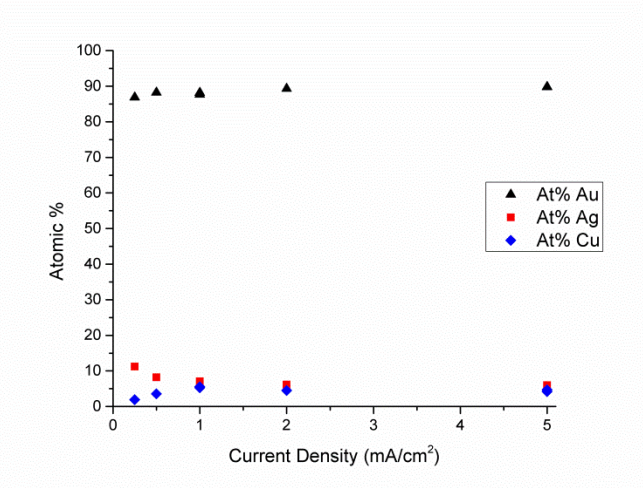

Figure 6-6: AuAgCu alloy composition versus current density at 0 rpm.

Figure 6-6 shows the AuAgCu alloy composition as a function of current density deposited at 0 rpm. The alloys contain 85 – 90 % Au due to the fact that there is roughly 10 times the concentration of Au^{+} ions compared to Cu and Ag combined in the plating bath and that under quiescent conditions, deposition is diffusion controlled. Given relatively similar diffusion coefficients, the Cottrell equation shown in Equation 2-15 states that the limiting current density should be proportional to the bulk concentration of an ion in solution.

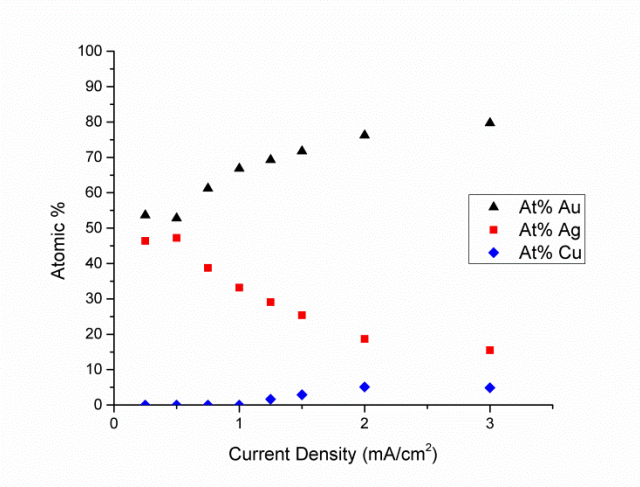

Figure 6-7: AuAgCu alloy composition versus current density at 125 rpm.

The results from deposition at 125 rpm are shown in Figure 6-7 above. For Rotating Disk Electrodeposition, Ag ions are continually refreshed during deposition resulting in a higher Ag composition compared to alloys deposited under quiescent conditions. Control of hydrodynamic conditions during deposition enables a wide range of alloy compositions to be produced from a single plating bath.

Alloy thin films were characterized using a J. A. Wollam VASE Spectroscopic Ellipsometer. Ellipsometry can be used to measure a film's index of refraction, n, and extinction coefficient, κ, given the knowledge of our sample's thickness and composition. These measurements can be used to calculate the complex permittivity of the sample given the relationship shown below, which was introduced earlier in Equation 4-20.

$$\varepsilon = \varepsilon' + i\varepsilon'' = (n + i\kappa)^2$$

Equation 6-13: Complex permittivity relationship.

An estimate of a samples effectiveness as a plasmonic material can be made using the plasmonic quality factor metric shown in Equation 4-13 and repeated bellow. This value is proportional to the expected surface plasmon propagation length since for a given application the wavelength and dielectric permittivity are fixed, leaving only the alloy's complex permittivity, ε' and ε'', to influence propagation length.

$$Q_{SPP}(\omega) = \frac{\varepsilon_m'(\omega)^2}{\varepsilon_m''(\omega)}$$

Equation 6-14: Plasmonic quality factor.

Measurements of plasmonic quality factor at 800 nm as a function of deposition current and rotation rate are shown in Figure 6-8 below. Alloys deposited at lower current densities as well as at lower rotation rates showed better plasmonic quality factors. This is possibly due to the lower Cu content in these films. Cu has worse plasmonic properties than either Au or Ag but its inclusion is expected to improve the integrity of the alloy. It is also possible that at higher electrodeposition current densities there is some sulfur inclusion due to the incomplete reduction of the Au_2SO_{3ads} intermediate as discussed in the previous section.

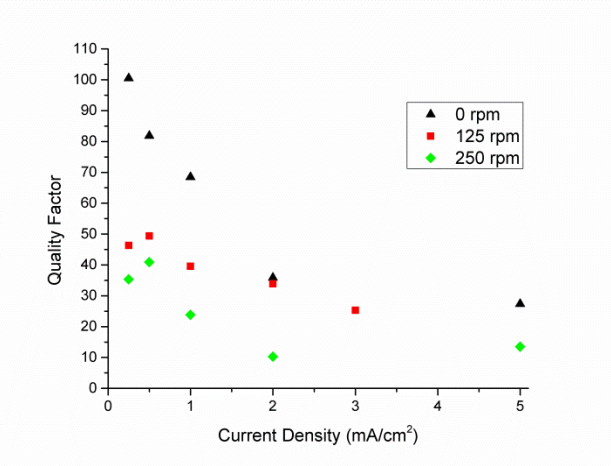

Figure 6-8: Plasmonic quality factor as a function of current density and rotation rate.

Thin film alloy samples were then annealed at 350 ˚C for 1 hour to evaluate their performance in the conditions expected in Heat Assisted Magnetic Recording and other high energy density plasmonic applications. The results in Figure 6-9 show a dramatic improvement in plasmonic quality factor across the entire range of samples. Quality factor values increased by an average of 270 % post annealing.

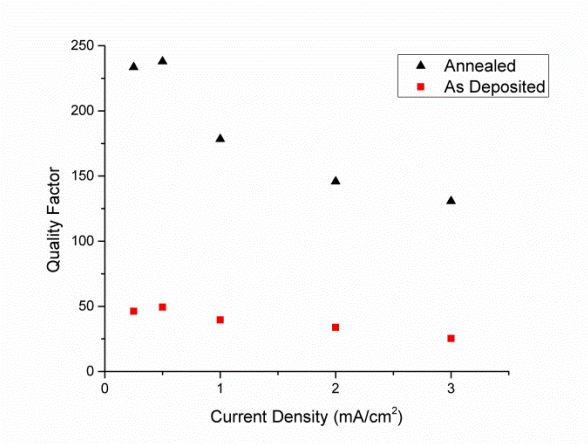

Figure 6-9: Quality factor versus current density at 125 rpm before and after annealing.

AuAgCuNi alloys were electrodeposited by adding 0.003 M $NiSO_4$ to the solution described above. EDS measurements showed Ni concentrations of < 1 % in samples deposited at 1 mA/cm^2 and 125 rpm.

100 nm thin film samples of Au, AgCu and AuAgCuNi were electrodeposited to compare with Au thin films prepared by Physical Vapor Deposition (PVD). The results are shown in Table 6-2 below.

Sample	Q Pre-Anneal	Q Post-Anneal
ED Au	177.43	566.05
AuAgCu	159.83	188.98
AuAgCuNi	153.50	230.25
PVD Au	403.93	463.57

Table 6-2: Plasmonic quality factor before and after annealing.

Quality factor improved for all samples, however the largest increase was seen in electrodeposited gold. PVD gold showed the highest quality factor pre-anneal but did not increase as significantly post anneal. The AuAgCu and AuAgCuNi alloys showed lower plasmonic quality factor but were expected to show greater thermal stability.

Quality factor as a function of annealing temperature is shown in Figure 6-10 below. AuAgCu alloy samples deposited at 1 mA/cm^2 and 125 rpm were annealed for 1 hour at temperatures between 100 and 350 ˚C. Higher annealing temperatures

improved the quality factor and it is possible that the quality factor will further increase with even higher annealing temperatures.

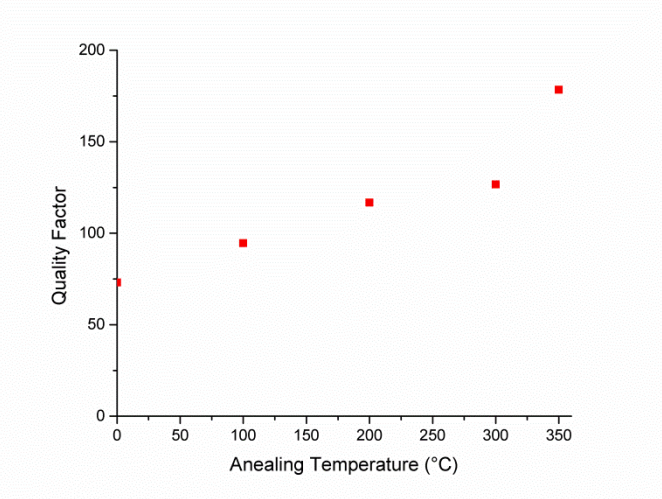

Figure 6-10: Quality factor versus annealing temperature for AuAgCu alloy deposited at 1 mA/cm² and 125rpm.

This improvement is possibly due to the removal of impurities during the annealing process. In addition, grain growth during annealing reduces scattering due to grain boundaries and can increase plasmon propagation length. However, impurities and smaller grains both contribute to material integrity, so this improvement in plasmonic quality may be balanced by a reduction in alloy reliability.

Thin film roughness was analyzed using Atomic Force Microscopy (AFM). Measurements were taken using a Bruker (Veeco/ Digital Instruments) Nanoscope III Multimode SPM. Roughness is an important parameter because increased

surface roughness can reduce surface plasmon propagation length.[31, 90] The results for deposition of 100 nm Au thin films at various currents are shown in Figure 6-11 below.

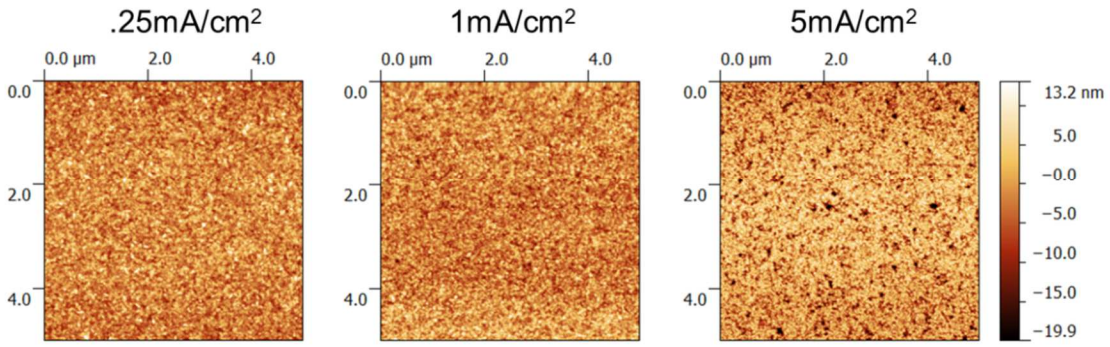

Figure 6-11: AFM roughness versus deposition current for electrodeposited Au.

Films deposited at 5 mA/ cm² show voiding. This is due to the higher deposition rate limiting the amount of surface diffusion during deposition which is needed for smooth and uniform thin films. Voiding in gold thin films can be difficult to identify with SEM due to resolution limits, however AFM shows voiding as well as individual grain size clearly.

Roughness values calculated from these measurements show a minimum surface roughness corresponding to deposition at 1 mA/ cm². Both average (R_a) and root mean squared (R_{rms}) roughness results are shown in Table 6-3. The roughness minimum observed at 1 mA/ cm² is believed to be a product of deposition rates and surface diffusion. At lower deposition current densities, surface diffusion creates

larger grains while at higher deposition current densities voiding is observed as shown in Figure 6-11.

i (mA/cm^2)	Thickness (nm)	R_a (nm)	R_{rms} (nm)
0.25	100	2.67	3.45
1	100	1.23	1.57
5	100	3.7	4.81

Table 6-3: Au roughness versus current density.

Roughness data can be further analyzed by performing a Fourier transform to produce a Power Spectral Density (PSD) function which retains the length scale information lost by the R_a or R_{rms} roughness calculation.[28] Roughness length scale is important for plasmonics applications since roughness with a lateral length scale less than 100 nm has a larger impact on surface plasmon propagation length.[31, 88] AFM measurements taken on 100 nm, 500 nm and 5000 nm electrodeposited Au films were analyzed using the PSD function and the results are shown in Table 6-4 below.

	100nm Au	500nm Au	5000nm Au
R_{rms} (nm)	2.48	5.57	14.93
R_{rms} < 100 nm	2.44	4.98	11.71
Max λ (nm)	41.88	113.67	159.14

Table 6-4: Roughness power spectral density.

The PSD function results can be used to calculate a R_{rms} value which only includes length scales less than 100 nm by integrating the PSD function from 0 to 100 nm.

This calculation shows that while roughness increases with film thickness as expected, roughness with a length scale less than 100 nm does not increase as significantly. For a plasmonic application this new length scale value can give a better measure of how a thin film's roughness will affect surface plasmon propagation.

X-ray Diffraction measurements were taken using a Bruker-AXS Microdiffractometer with a Cu Kα source. In addition to standard XRD measurements, this system uses a 2 dimensional detector along with a 1/4 circle Eulerian cradle sample holder to conduct pole figure measurements for texture analysis. Diffraction intensity at a given θ angle corresponding to a specific crystallographic direction is measured over a range of ω, φ and χ angles. A total of 168 individual measurements were taken to produce the result shown in Figure 6-12 which shows the intensity of the diffraction peak at 38.2 degrees corresponding to the <111> crystallographic direction in Au.

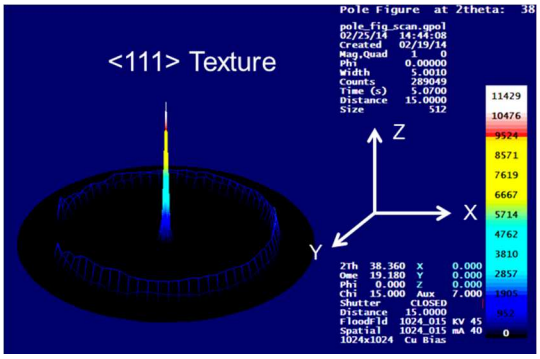

Figure 6-12: Electrodeposited Au XRD <111> pole figure.

The results in Figure 6-12 show that our electrodeposited Au films have a strong <111> texture in the Z direction perpendicular to the substrate. In addition, a smaller intensity peak is observed corresponding to the off-axis <-111> textures at an angle of 70.53 degrees according the interplanar angle formula in Equation 2-5. These results are characteristic of Au thin films and match XRD pole figure measurements on Au films prepared with PVD.

XRD can also be used to approximate grain size using the Scherrer equation introduced in Equation 3-9 and repeated below.

$$D = \frac{\kappa\lambda}{\beta\cos(\theta)}$$

Equation 6-15: Grain size calculation using the Scherrer equation.

In this equation, λ is the wavelength of X-ray radiation used for the measurement. κ is the Scherrer constant which depends on the crystallite shape and is equal to 0.94 for spherical grains of a cubic material, it is often approximated as 1. θ is the Bragg angle of the peak while β is the FWHM peak with after compensating for instrumental broadening effects. Grain sizes calculated using the Scherrer equation are shown below in Figure 6-13 as a function of electrodeposition current density.

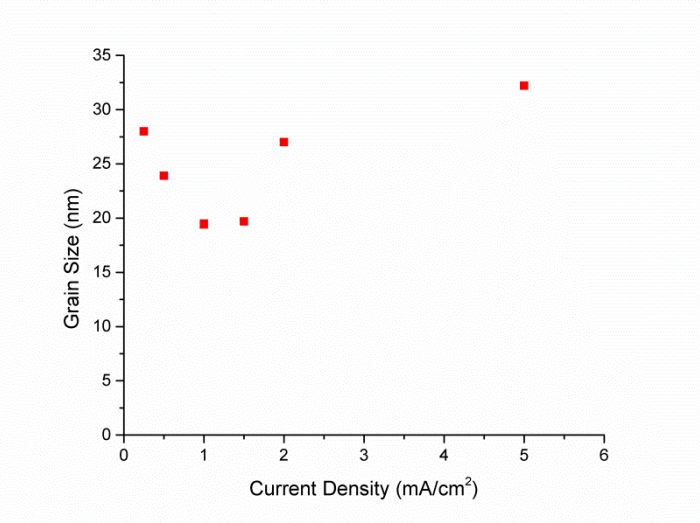

Figure 6-13: Au grain size versus deposition current.

Grain size initially decreases with current density then increases for currents greater than 1 mA/ cm^2. This result matches our previous roughness measurements which showed a roughness minimum at approximately 1 mA/ cm^2. The initial decrease in roughness and grain size can be attributed to the reduction in surface diffusion as deposition rates increase. However, at higher current densities it is possible to reach a limiting current density due to the depletion of Au^+ in solution at the substrate surface. In this situation, the deposition rate becomes diffusion controlled and does not follow the trend observed for lower current densities. These results show that given our bath composition, deposition at 1 mA/ cm^2 will minimize Au thin film roughness and grain size which is desirable for plasmonic applications.

Grain size was also measured pre and post Anneal at 350 ˚C for 1 hour and the results are shown below in Table 6-5.

Sample	Pre-Anneal	Post-Anneal	% increase
ED Au	19.2	32.6	69.7
AuAgCu	27.9	35.4	26.8
AuAgCuNi	31.2	34.6	10.9
PVD Au	32.6	35.3	8.2

Table 6-5: Grain size before and after annealing.

Grain size post annealing increased less when the Au films were alloyed with Cu and Ni. The AuAgCuNi showed the greatest stability among electrodeposited films studied, however PVD Au thin films showed a slightly smaller increase in grain size post annealing.

Electrodepsoited Au alloys show many advantages in plasmonic applications. Au thin film roughness, plasmonic quality factor and grain size can all be controlled by varying process parameters. While these properties are similar to those of PVD films, electrodeposited films are inherently free of ion damage due to patterning which can lead to device failure. Electrodeposition also allows a wide range of plasmonic alloys to be quickly and inexpensively investigated. These advantages make electrodeposited Au alloys a promising option for plasmonic applications.

6.4 Transmission-EBSD characterization

6.4.1 Background and Simulations

In addition to materials challenges, HAMR requires increased understanding of the process by which nanoscale plasmonic near field transducers (NFTs) deform and fail. Incredible progress has been made in HAMR reliability with lifetimes increasing from "several tens of track recordings" in 2009 to a 1 Terabyte per square inch demo in 2012 and most recently a 1000 write power on hours demo in 2014.[3, 4, 62] However, better device characterization and understanding of deformation mechanics is required to produce a robust consumer device.

Nanoscale deformation is significantly different from macroscale melting. Deformation at the nanoscale is dominated by point and line defects which result in surface reconstruction. Gold {110} facets have higher surface energy than either {111} or {100} facets and have been seen to reconfigure into a lower energy configuration when exposed to large temperatures or energies.[76] Gold surface energies are shown in Table 6-6 below.[91] Observations of electrochemically prepared gold nanoparticles using high resolution TEM have shown that nanorods display {110} facets while nanospheres are composed of only the more stable {111} and {100} facets.[92, 93]

Surface	Energy (J/m^2)
{111}	1.283
{100}	1.627
{110}	1.700

Table 6-6: Gold surface energies.

Previous work showing the importance of crystallographic structure on deformation and surface reconstruction has been done using single diffraction measurements taken on a TEM. While this approach can give high resolution images of single crystal gold nanoparticles, it is not suited for characterizing a polycrystalline thin film sample. Techniques such as Precession Enhanced Diffraction (PED) exist which can characterize polycrystalline samples, but requires additional hardware and software to be added to the TEM setup.[34]

Electron Backscatter Diffraction (EBSD) is a SEM based technique capable of identifying and mapping crystallographic orientation. EBSD analyzes the Kikuchi diffraction pattern created by backscattered electrons to determine the crystallographic orientation of the sample. While primarily used for geologic and industrial samples due to its low resolution, the fast speed, ease of sample preparation and measurement as well as low cost make it an attractive option for characterization of gold thin films if the resolution limits can be overcome.

The resolution of EBSD is primarily limited by the interaction volume of the electrons within the sample. Electrons encounter the sample at a 70 degree incident angle and scatter off atoms in the lattice. For this work, the initial samples used were 50nm of sputtered Au on an oxidized Si wafer substrate. The Monte Carlo simulator CASINO was used to calculate electron trajectories within the sample and produced the results seen in Figure 6-14.

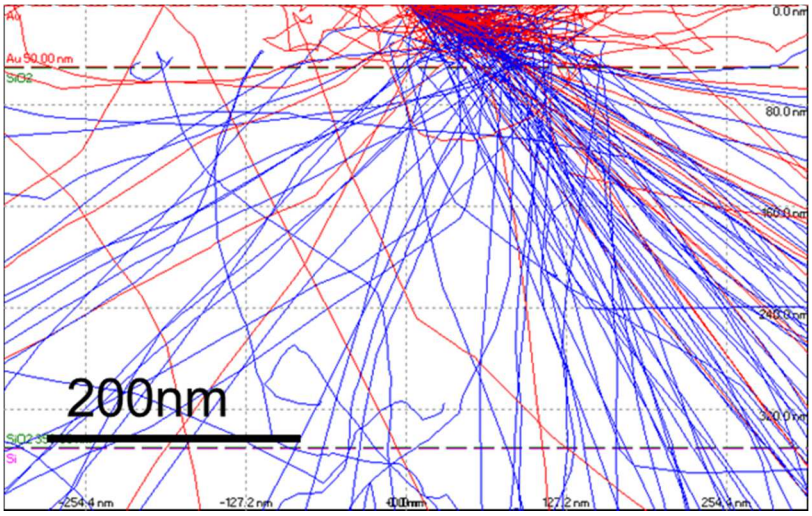

Figure 6-14: EBSD electron trajectories generated with CASINO.

In Figure 6-14, the red lines represent the trajectories of electrons which are backscattered and escape the sample while the blue lines represent electrons with trajectories which end within the sample. Since only the backscattered electrons contribute to the Kikuchi diffraction patterns used for EBSD it is useful to measure their distribution to determine the approximate resolution of this technique. The

maximum depth distribution of backscattered electrons is shown in Figure 6-15 below.

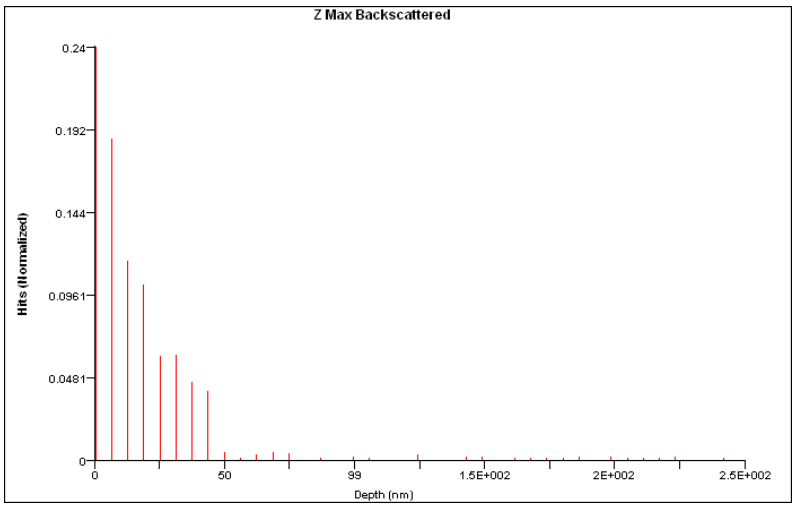

Figure 6-15: Backscattered electron maximum depth histogram.

Figure 6-15 shows that the majority of backscattered electrons are scattered in the 50 nm Au layer. This result is expected because the Au has a much higher atomic number than the SiO_2/ Si substrate and is much more likely to backscatter an incident electron. The results in Figure 6-15 are also positive because we only want electrons backscattered from the Au layer to contribute to our diffraction pattern.

The horizontal distribution of backscattered electrons is shown in Figure 6-16. Due to the geometry required for EBSD electrons encounter the sample at a 70 degree angle and travel horizontally before exiting the sample. Figure 6-16 shows that backscattered electrons can travel up to 200 nm within the sample.

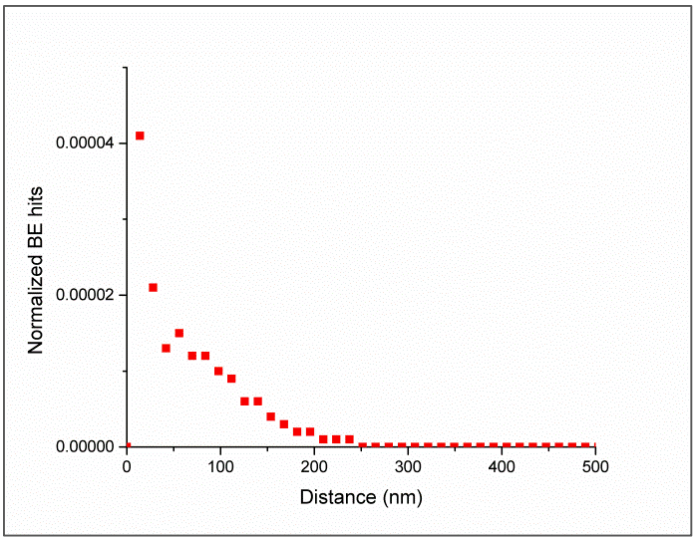

Figure 6-16: Horizontal distance traveled by backscattered electrons.

From our previous AFM and XRD measurements, we expect our gold thin films to have grain sizes on the order of 20 to 30 nm. The results in Figure 6-16 show that backscattered electrons could come from 10 or more different grains during a single measurement using conventional EBSD. In this case, the diffraction patterns from each grain overlap and the system is unable to measure the orientation of the sample at that point. When our gold thin films were measured with conventional EBSD we were not able to observe any Kikuchi patterns due to this effect.

Recently, improvements in EBSD resolution have been obtained using thin specimens or nanoparticles in a transmission configuration.[94] This process is referred to as transmission EBSD or t-EBSD. In transmission mode, the electron interaction volume is much smaller and there is no scattering from the substrate.

The geometry used for t-EBSD is shown in Figure 6-17. A holder was fabricated to keep a thin sample at approximately 10 degrees off normal as indicated in Figure 6-17.

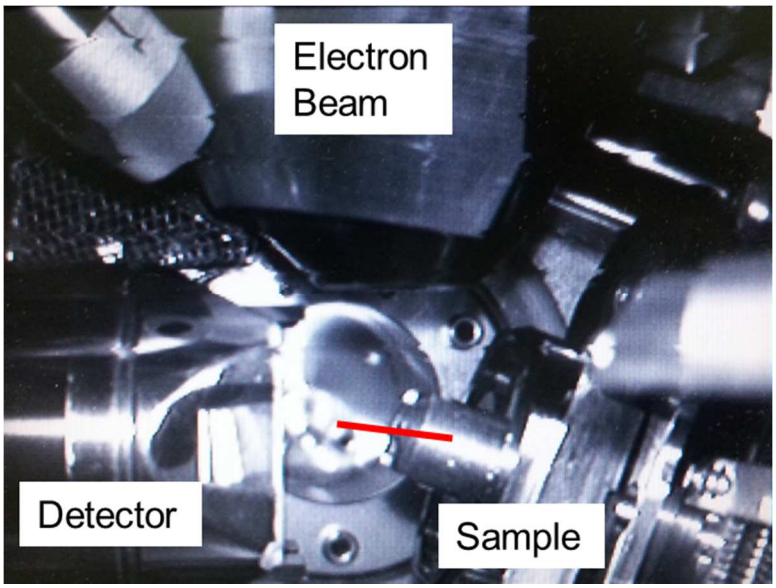

Figure 6-17: Transmission EBSD measurement geometry.

Simulations were performed using CASINO to predict the potential of this new approach. A 50 nm Au thin film on a 5 nm Si_3N_4 substrate was modeled. Simulations for t-EBSD used a -10 degree sample tilt as opposed to the 70 degree tilt used to simulate conventional EBSD. An example simulation is shown in Figure 6-18, which initially appears to have an interaction volume roughly 10 times smaller than seen in Figure 6-14 for conventional EBSD. For t-EBSD, only electrons which are transmitted through the sample can contribute to the Kikuchi diffraction pattern. These electron trajectories are shown in blue in Figure 6-18 below. Results

from literature have suggested that this technique is capable of producing resolutions as low as 8-16nm.

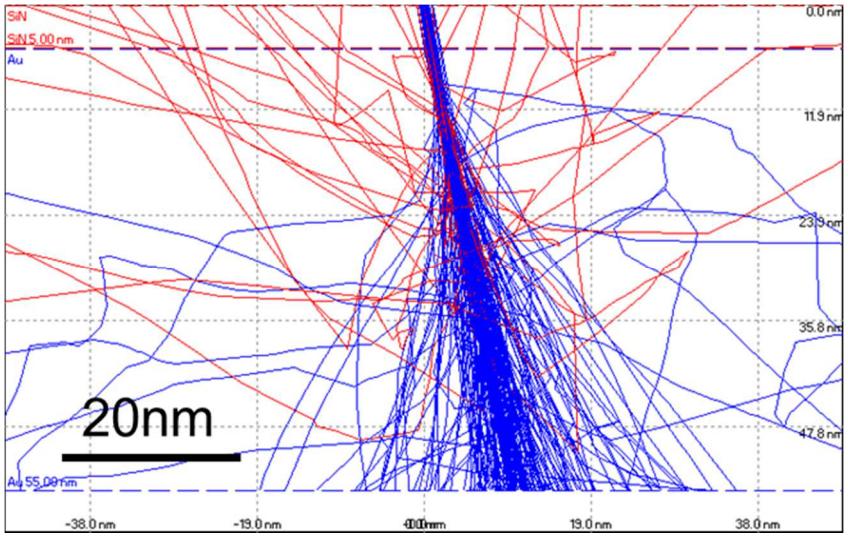

Figure 6-18: Transmission EBSD electron trajectories simulated using CASINO.

Resolution was approximated using the distribution of electrons at the far side of the sample. The effect of acceleration voltage was investigated to find the optimal measurement parameters. These results are shown in Figure 6-19 with the Full Width Half Maximum (FWHM) of each electron distribution shown in Table 6-7.

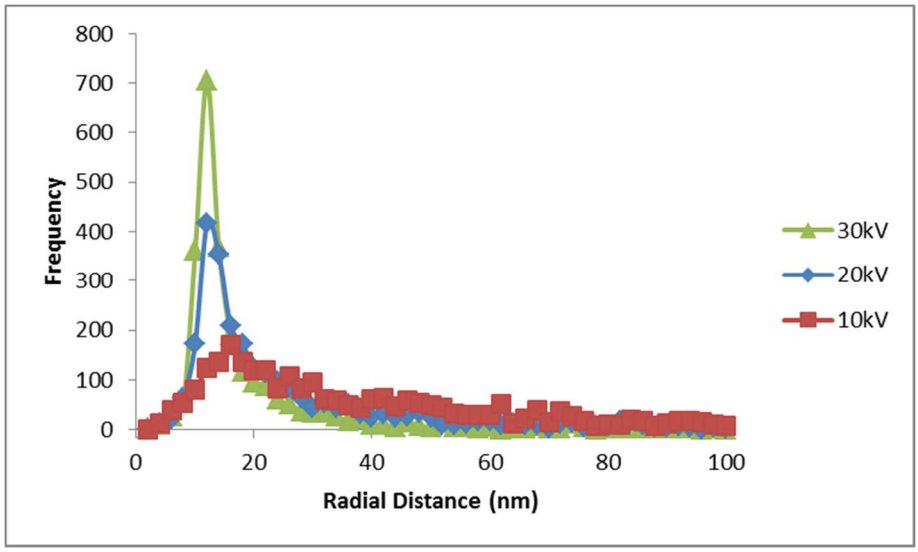

Figure 6-19: Simulated backscatter electron distribution as a function of accelerating voltage.

Potential	FWHM
10kV	18nm
20kV	6nm
30kV	4nm

Table 6-7: Backscatter electron Full Width Half Maximum versus accelerating voltage.

These results show that higher accelerating voltages produce much tighter electron trajectory distributions. Electron distribution decreased from 18 nm to 4 nm when the accelerating voltage was increased from 10 kV to 30 kV. In addition, lower accelerating voltage also broadens the Kikuchi lines. Based on these simulations, t-EBSD measurements were conducted at 30 kV which is the highest accelerating voltage possible with the SEM available.

6.4.2 Results and discussion

Samples were prepared by sputtering 25 nm of Au on commercial TEM windows purchased from TEMwindows.com. A sample clamped in our custom holder during measurement is shown in Figure 6-20. The substrate has 9 50 μm wide windows with 5 nm thick Si_3N_4 membranes to provide support for the gold thin film. While designed for TEM imaging, these substrates work exceptionally well for transmission EBSD since the thin Si_3N_4 membrane is almost entirely electron transparent.

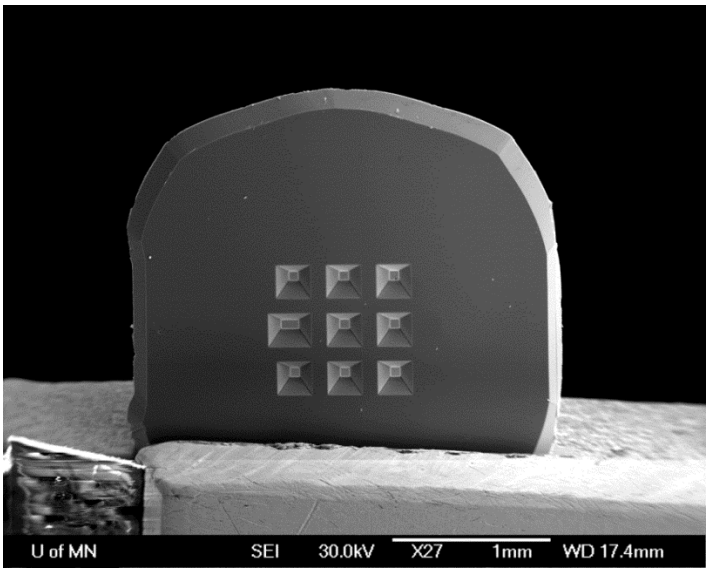

Figure 6-20: TEM window during t-EBSD characterization.

Measurements were taken using a JEOL 6500 Field Emission Gun SEM along with an EBSD detector manufactured by HKL and Oxford Instruments. Based on our

simulations, a 30 kV acceleration voltage was used along with the maximum beam current possible. Data acquisition, processing and analysis were performed using the HKL Channel 5 EBSD software package.

An example diffraction pattern is shown in Figure 6-21 below. t-EBSD produces much higher contrast Kikuchi lines compared to conventional EBSD when analyzing gold thin films with 20 to 30 nm grain sizes. Kikuchi lines are automatically identified and indexed and matched to their corresponding crystal orientation. The inset in Figure 6-21 shows that the diffraction pattern recorded corresponds to a crystal orientation with its <111> direction approximately perpendicular to the substrate.

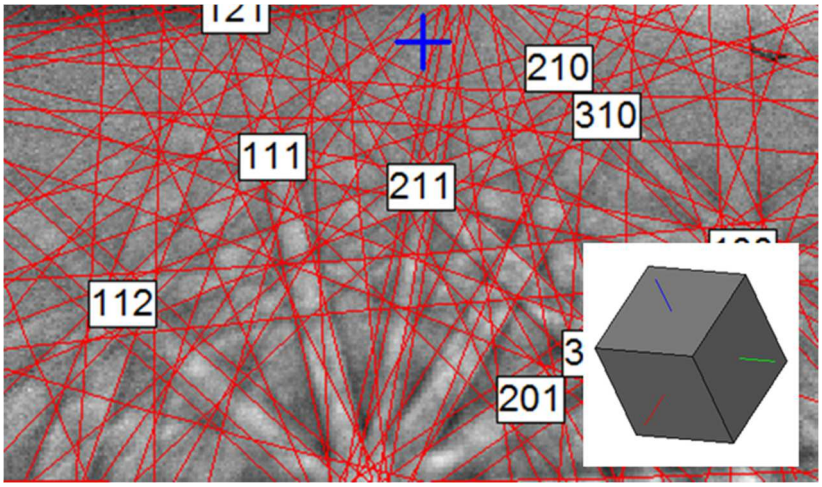

Figure 6-21: Example indexed Kikuchi diffraction pattern and corresponding crystal orientation (inset).

The electron beam can be rastered across the sample to produce a map of crystallographic orientation. Based on our simulation results of electron interaction

volume, a step size of 10 nm was chosen. Results are shown in Figure 6-22 below. 80 – 90% indexing has been achieved over a 1 μm by 1 μm area using this technique. It is possible to further increase indexing by applying a post processing noise reduction algorithm to achieve greater than 90% indexing.

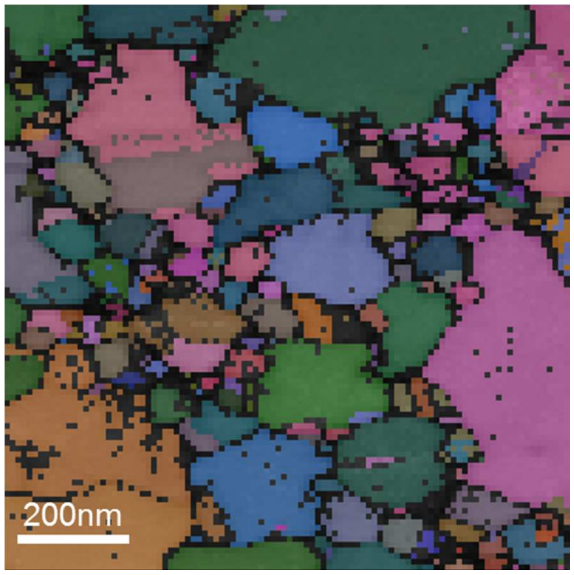

Figure 6-22: Euler map of crystallographic orientation.

The color scheme used in Figure 6-22 assigns a red green blue value to each of the three Euler angles. This provides a vivid contrast to individual grains. The large variation in grain size matches observations using TEM. Figure 6-22 shows that grains as small as 10 – 20 nm (1 – 2 pixels) have been indexed. However, the Euler color scheme does not provide any quantitative data about individual crystallographic orientations.

It is also possible to produce a map of Kikuchi band contrast which serves as a measure of the quality factor of the measurement process. This is shown in Figure 6-23 below. These results match the appearance of grains in the film because contrast is typically lowest at grain boundaries where overlapping diffraction patterns from adjacent grains due to the electron interaction volume make it difficult to assign a single crystallographic orientation at the grain boundary.

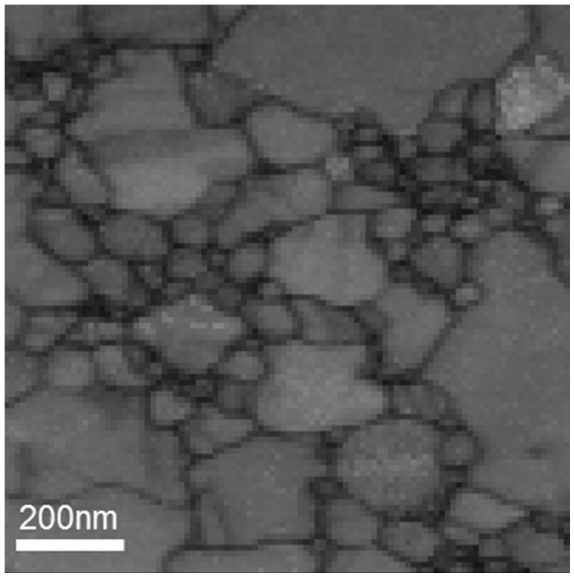

Figure 6-23: Quality factor map showing Kikuchi band intensity and band contrast during imaging.

Texture information can be visualized using an Inverse Pole Figure (IPF) plot, an example is shown in Figure 6-24. In this coloring scheme, the texture in a given direction is represented by the color legend seen in the figure. Figure 6-24 shows the texture in the X, Y (in plane) and Z (perpendicular to the plane) directions. The results show that the films have a strong <111> texture, represented by the blue

color in the Z direction. This matches our XRD measurements and confirms the validity of these measurements. There is also a strong in-plane <110> texture due to the 90 degree angle between the <111> and <1-10> directions according to Equation 2-5. It is also possible to observe twinning in several of the grains.

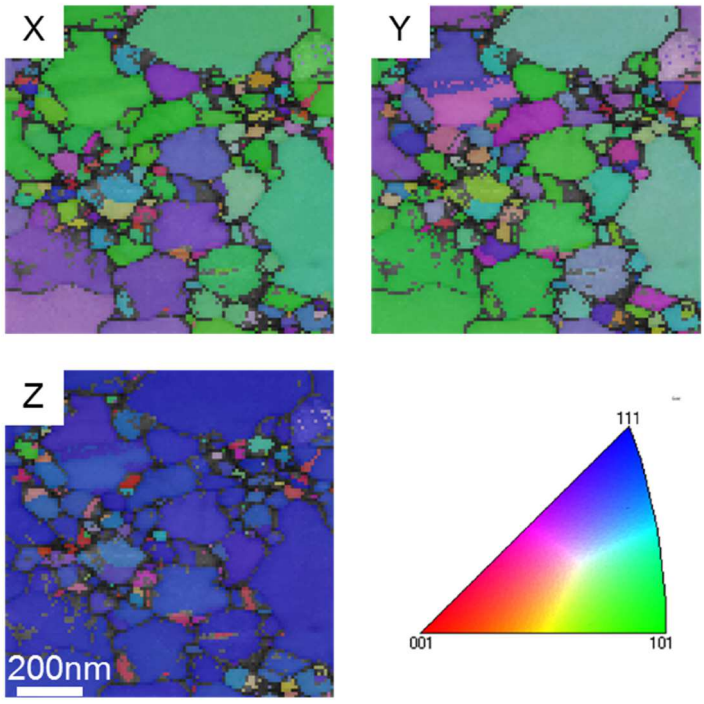

Figure 6-24: Crystallographic orientation measured with t-EBSD.

Data can also be organized using pole figures. Rather than displaying the texture in each direction as above, pole figures display the direction distribution of each texture. The results in Figure 6-25 show that the <111> texture is strongly oriented in the Z direction which matches our previous results. The <100> and

<110> textures follow as expected and do not have any additional preferred orientation.

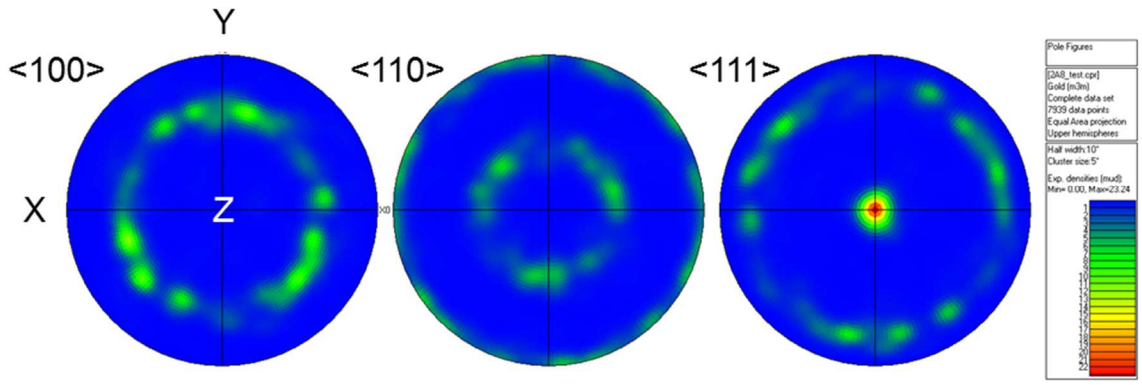

Figure 6-25: Pole figures generated from EBSD data.

The previous results accurately characterize our films but do not provide much additional information beyond basic texture and grain size data which was available through XRD and do not demonstrate the full capability of EBSD. Given the wealth of crystallographic information available with EBSD it is possible to produce a much more detailed analysis of our samples. Figure 6-26 shows the deviation angle between the measured <111> direction and normal to the substrate.

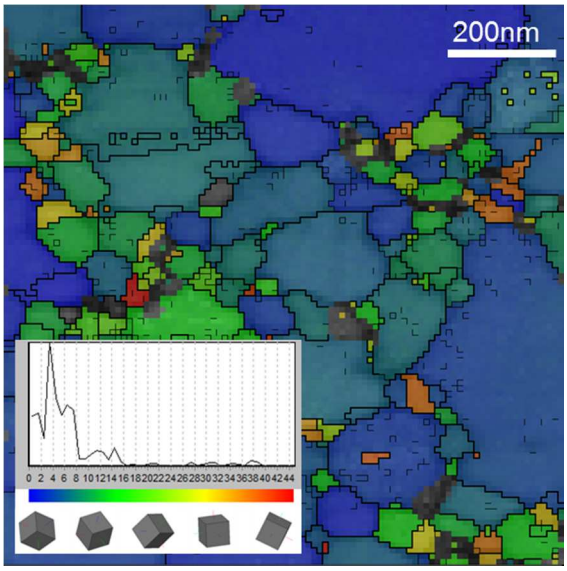

Figure 6-26: Grain misoreintation and histogram measured with t-EBSD.

The results show that the majority of grains are oriented within 6 degrees of normal. Grains with <111> orientations much further from normal are marked in shades of yellow and red. This analysis can also be used to locate areas of deformation in samples.

Grain boundary angle is an important parameter when investigating the integrity of polycrystalline materials.[95] In general, low angle grain boundaries, which have grain boundary angles less than 10 degrees, have lower energies then high angle grain boundaries. Coincident Site Lattice (CSL) boundaries, in which adjacent grains have some fraction of lattice sites in common, also have very low energies.[13, 15] These low energy configurations are more stable and their presence

will result in more robust polycrystalline films. Crystallographic information can also be used to derive the grain boundary angle between two adjacent grains.

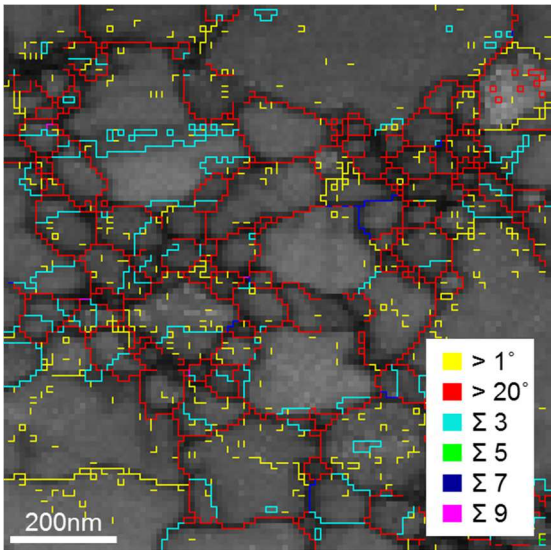

Figure 6-27: Grain boundary angle map.

Figure 6-27 shows the grain boundary angle between adjacent grains. High angle grain boundaries are shown in red while low angle grain boundaries are shown in yellow. CSL boundaries are labeled according to the inverse density of their common lattice points. Twin boundaries observed in Figure 6-24 are more clearly visible as Σ3 boundaries in Figure 6-27.

EBSD is useful technology for characterizing the crystallographic structure of a variety of samples. However, until recently it has been restricted to low resolution applications due to electron interaction volume. The dramatic increase in resolution with Transmission EBSD allows us to apply this powerful characterization

technique at the nanoscale. One such application which stands to benefit from these developments is HAMR, which requires the development of robust nanoscale Au transducers. By applying this technique to gold thin films, t-EBSD can be used to investigate failure mechanisms, predict material integrity and perhaps contribute to HAMR's successful development.

7 Results and Conclusions

7.1 Summary

Identifying the fundamental characteristics which influence a material's properties has been critical to understanding and developing a range of thin film metals and alloys. While both the applications and challenges of magnetostrictive GaFe and plasmonic gold vary greatly, the approach to solving these problems is similar. Beyond the conclusions presented here, this work forms a solid foundation for addressing material development problems in the future.

In order to successfully measure magnetostriction in electrodeposited GaFe thin films, issues with delamination and uniformity first had to be addressed. Adhesion was improved by developing a sputtered Cr/ Cu seed layer process while 11 % thickness uniformity and 1 % compositional uniformity was achieved through the use of rotating disk electrochemistry. These developments allowed magnetostriction in GaFe thin films to be measured for the first time. Measured magnetostriction values were lower than initially expected, however when the GaFe polycrystallinity was measured using x-ray diffraction and accounted for, our measurements matched our predictions. Magnetostriction values of approximately 100 ppm were obtained which along with our robust deposition process results

show that these electrodeposited alloys are promising candidates for magnetostrictive applications.

Electrodeposition was also used to investigate gold and gold alloys for potential applications in Heat Assisted Magnetic Recording. The extreme optical and reliability requirements for this application can potentially be met with electrodeposited films because they can be more stable due to sulfur inclusions and grain refinement due to alloying. A sulfite-thiosulfate based gold electrodeposition solution was investigated and the deposition mechanism was discussed. Understanding the gold electrodeposition mechanism allowed the development of several gold alloys. These alloys showed improved thermal stability with an average increase in grain size post anneal of 10.9 % for AuAgCuNi compared with 69.7 % for pure electrodeposited gold. In addition, other alloy compositions may possibly exist with even greater thermal stability.

Characterization of crystallographic properties is also important for developing more reliable plasmonic materials due to the large energy densities encountered in these applications. Material properties influencing thermal stability including film texture, grain size and grain boundary configuration were investigated using Electron Backscatter Diffraction. Simulations conducted were used to optimize the process parameters which greatly improved detection and resolution. These results were confirmed by x-ray diffraction and showed that

tEBSD is a valuable technique for analyzing the crystallographic structure of nanoscale materials. In addition, tEBSD is capable of deriving crystallographic information such as grain boundary configuration which is vital for predicting material thermal stability.

7.2 Future Work

Going forward, this work enables many exciting possibilities. Results on electrodeposited galfenol have shown that the material is suitable for a variety of applications which are now being investigated. Electrodeposited gold and gold alloy results show promise for plasmonic applications requiring good thermal stability and suggest that further research may produce other alloy compositions with even greater potential. The demonstration of transmission Electron Backscatter Diffraction also enables promising developments in material characterization. In addition to the characterization of thin films discussed previously, this technique can be used to analyze the crystallographic properties of patterned samples, a unique capability of tEBSD.

While the magnetostriction values observed for electrodeposited Galfenol were lower than those of bulk samples, electrodeposition offers many advantages over bulk materials and other forms of deposition. A variety of devices can be inexpensively fabricated using electrodeposited magnetostrictive Galfenol such as integrated torque sensors, MEMS pressure sensors, SONAR sensors and actuators. Some of these applications take advantage the ability of electrodeposition to create high aspect nanowire structures and uniformly cover non-flat surfaces.

One such application is shown in Figure 7-1 below. Galfenol/ Gold multilayer nanowires were electrodeposited into Anodic Aluminum Oxide templates to study magnetization in nanowires using neutron scattering. Electrodeposition was completed using a single GeFe/ Au solution which allowed multilayer structures to be deposited by varying the deposition conditions during the process. The multilayers in 35 nm diameter wires are highlighted with an arrow below. This demonstrates the capability to integrate magnetostrictive galfenol in complex nanowire structures using electrodeposition.

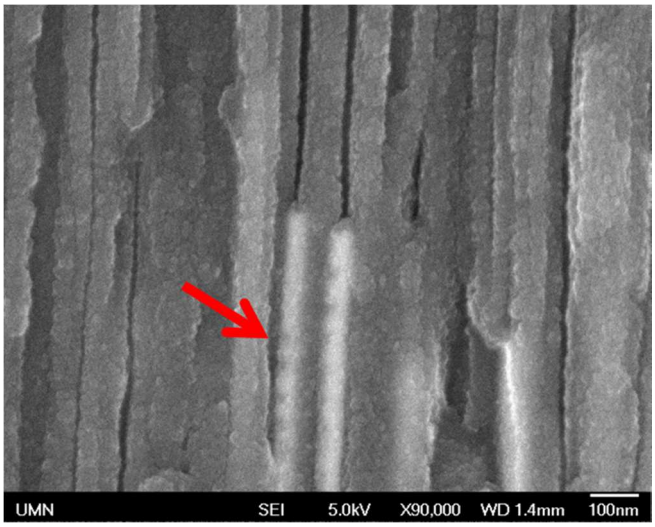

Figure 7-1: Galfenol/ Gold multilayer nanowires in an Anodic Aluminum Oxide template.

The large improvement in resolution obtained using Electron Backscatter Diffraction in transmission mode demonstrated that this technique is a valuable method of nanoscale material characterization. Other gold films and alloys can be measured to investigate the effect of deposition conditions and alloying on

crystallographic structure and material stability. In addition, while the results presented were obtained using thin films, one of the advantages of this technique is the capability to measure patterned nanostructures.

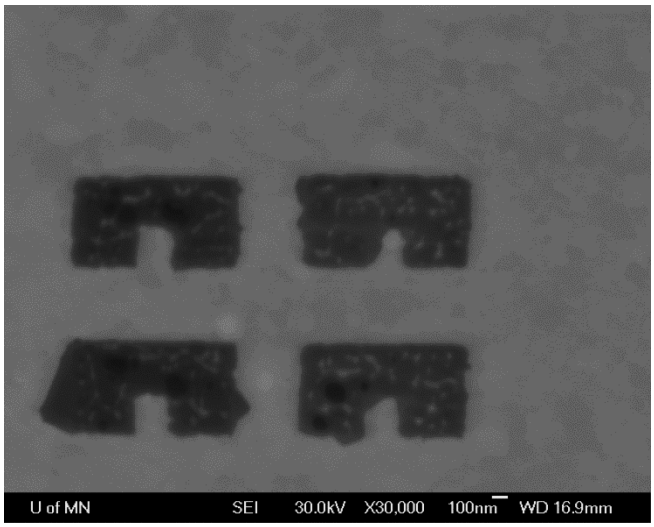

Figure 7-2: Patterned cantilevers showing deformation post annealing.

Figure 7-2 shows thin film gold features patterned using a Focused Ion Beam. These structures were then encapsulated in aluminum oxide and annealed to induce deformation. tEBSD can be used to analyze the crystallographic structure of these devices and correlate that to device reliability. Statistical data from multiple features is currently being gathered to determine the impact of texture, grain size and grain boundary configuration on device reliability. Results from this investigation will potentially be used to form decisions on the development of Heat Assisted Magnetic Recording.

tEBSD can also be used on a variety of other materials and samples. While the results presented were obtained from gold, the technique can be applied to other nanostructured materials which could not previously be analyzed using conventional EBSD. Material crystallographic properties are now more important than ever for the development of nanoscale devices and tEBSD is an exciting technique for their investigation.

These results provide a solid basis for a number of current and future projects. Electrodeposited Galfenol based integrated torque sensors are currently being investigated and nanowire based studies of magnetostriction and magnetization are in progress. Heat Assisted Magnetic Recording is another exciting application which will hopefully benefit from these results. Electrodeposited gold alloys are potential candidates for plasmonic nanostructures and tEBSD is a powerful technique for better understanding device reliability. Finally, the experience gained will help in solving a variety of engineering challenges in the future.

8 References

[1] E. C. Estrine, W. P. Robbins, M. M. Maqableh, and B. J. Stadler, "Electrodeposition and characterization of magnetostrictive galfenol (FeGa) thin films for use in microelectromechanical systems," J. Appl. Phys. 113, 17 (2013).

[2] E. C. Estrine, M. Hein, W. P. Robbins, and B. J. Stadler, "Composition and crystallinity in electrochemically deposited magnetostrictive galfenol (FeGa)," J. Appl. Phys. 115, 17 (2014).

[3] W. Challener, C. Peng, A. Itagi, D. Karns, W. Peng, Y. Peng, X. Yang, X. Zhu, N. Gokemeijer, and Y. Hsia, "Heat-assisted magnetic recording by a near-field transducer with efficient optical energy transfer," Nature Photonics 3, 4 (2009).

[4] T. Rausch, A. S. Chu, P. Lu, S. Puranam, D. Nagulapally, and J. Dykes, Recording Performance of a Pulsed HAMR Architecture, (2014).

[5] E. Estrine, S. Riemer, V. Venkatasamy, B. Stadler, and I. Tabakovic, "Mechanism and Stability Study of Gold Electrodeposition from Thiosulfate-Sulfite Solution," J. Electrochem. Soc. 161, 12 (2014).

[6] M. Ohring, Materials Science of Thin Films, Academic press, (2001).

[7] E. Machlin, Materials Science in Microelectronics: The Relationships between Thin Film Processing and Structure, Cambridge Univ Press, (2006).

[8] J. A. Thornton, "High rate thick film growth," Annual Review of Materials Science 7, 1 (1977).

[9] R. J. Tilley, Crystals and Crystal Structures, Wiley. com, (2006).

[10] A. A. Kelly, and K. M. Knowles, Crystallography and Crystal Defects, Wiley. com, (2012).

[11] R. F. Pierret, Semiconductor Device Fundamentals, Addison-Wesley Reading, MA, (1996).

[12] C. Hammond, and C. Hammond, The Basics of Crystallography and Diffraction, Oxford University Press Oxford, (2009).

[13] G. Hasson, and C. Goux, "Interfacial energies of tilt boundaries in aluminium. Experimental and theoretical determination," Scripta Metallurgica 5, 10 (1971).

[14] D. Field, and D. Dingley, "MICROTEXTURE ANALYSIS IN ALUMINUM THIN-FILMS," Solid State Technol. 38, 11 (1995).

[15] D. Brandon, "The structure of high-angle grain boundaries," Acta Metallurgica 14, 11 (1966).

[16] P. D. McGary, L. Tan, J. Zou, B. J. Stadler, P. R. Downey, and A. B. Flatau, "Magnetic nanowires for acoustic sensors," J. Appl. Phys. 99, 8 (2006).

[17] W. Plieth, Electrochemistry for Materials Science, Elsevier, (2008).

[18] J. Newman, and K. E. Thomas-Alyea, Electrochemical Systems, John Wiley & Sons, (2012).

[19] H. J. Sand, "III. On the concentration at the electrodes in a solution, with special reference to the liberation of hydrogen by electrolysis of a mixture of copper sulphate and sulphuric acid," The London, Edinburgh, and Dublin Philosophical Magazine and Journal of Science 1, 1 (1901).

[20] F. Cottrell, "Residual current in galvanic polarization regarded as a diffusion problem," Z. Phys. Chem. 42, (1903).

[21] V. G. Levich, Physicochemical Hydrodynamics, Prentice-Hall Englewood Cliffs, NJ, (1962).

[22] C. M. Brett, and A. M. O. Brett, Electrochemistry: Principles, Methods, and Applications, Oxford university press Oxford, (1993).

[23] J. Butler, "Studies in heterogeneous equilibria. Part II.—The kinetic interpretation of the nernst theory of electromotive force," Transactions of the Faraday Society 19, March (1924).

[24] T. Erdey-Gruz, and M. Volmer, "Zur theorie der wasserstoffüberspannung," Z.Phys.Chem.A 150, (1930).

[25] J. E. Randles, "A cathode ray polarograph. Part II.—The current-voltage curves," Transactions of the Faraday Society 44, (1948).

[26] A. Ševčik, "Oscillographic polarography with periodical triangular voltage," Collect. Czech. Chem. Commun. 13, (1948).

[27] H. H. Girault, Analytical and Physical Electrochemistry, CRC Press, (2010).

[28] G. Haugstad, Atomic Force Microscopy Understanding Basic Modes and Advanced Applications, Hoboken, N.J. : Wiley, Hoboken, N.J., (2012).

[29] G. Binnig, C. F. Quate, and C. Gerber, "Atomic force microscope," Phys. Rev. Lett. 56, 9 (1986).

[30] G. Haugstad, SPM Training: Basic Imaging and Characterization, Characterization Facility, College of Science and Engineering, University of Minnesota, Minneapolis, MN, (2012).

[31] H. Raether, Surface Plasmons on Smooth Surfaces, Springer, (1988).

[32]College of Science and Engineering Characterization Facility Bruker Microdiffractometer User Manual, University of Minnesota, (2012).

[33] G. Gottstein 1944-, and G. Gottstein, Physical Foundations of Material Science, Berlin ; New York : Springer, Berlin ; New York, (2004).

[34] X. Zou, S. Hovmöller, and P. Oleynikov, Electron Crystallography: Electron Microscopy and Electron Diffraction, Oxford University Press, (2011).

[35] D. J. Prior, A. P. Boyle, F. Brenker, M. C. Cheadle, A. Day, G. Lopez, L. Peruzzo, G. J. Potts, S. Reddy, and R. Spiess, "The application of electron backscatter diffraction and orientation contrast imaging in the SEM to textural problems in rocks," Am. Mineral. 84, (1999).

[36] E. Mariani, D. Prior, D. McNamara, M. Pearce, N. Seaton, G. Seward, D. Tatham, and J. Wheeler, "Electron backscatter diffraction (EBSD) in the SEM: applications to microstructures in minerals and rocks and recent technological advancements," Seminarios De La Sociedad Espanola De Mineralogıa 5, (2008).

[37] T. Maitland, and S. Sitzman, Electron Backscatter Diffraction (EBSD) Technique and Materials Characterization Examples, Springer Berlin, (2007).

[38] S. Zaefferer, "On the formation mechanisms, spatial resolution and intensity of backscatter Kikuchi patterns," Ultramicroscopy 107, 2 (2007).

[39] B. D. Cullity, and C. D. Graham, Introduction to Magnetic Materials, Wiley. com, (2011).

[40] A. E. Clark, J. B. Restorff, M. Wun-Fogle, T. A. Lograsso, and D. L. Schlagel, "Magnetostrictive properties of body-centered cubic Fe-Ga and Fe-Ga-Al alloys," Magnetics, IEEE Transactions On 36, 5 (2000).

[41] J. Atulasimha, and A. B. Flatau, "A review of magnetostrictive iron–gallium alloys," Smart Mater. Struct. 20, 4 (2011).

[42] R. Hall, "Single-Crystal Magnetic Anisotropy and Magnetostriction Studies in Iron-Base Alloys," J. Appl. Phys. 31, (1960).

[43] A. E. Clark, M. Wun-Fogle, J. B. Restorff, and T. A. Lograsso, "Magnetostrictive properties of Galfenol alloys under compressive stress," Materials Transactions 43, 5 (2002).

[44] E. Klokholm, "The measurement of magnetostriction in ferromagnetic thin films," Magnetics, IEEE Transactions On 12, 6 (1976).

[45] N. Tsuya, K. I. Arai, K. Ohmori, and Y. Shirage, "Magnetostriction measurement by three terminal capacitance method," Japan.J.Appl.Physics 13, 11 (1974).

[46] S. Link, Z. L. Wang, and M. El-Sayed, "Alloy formation of gold-silver nanoparticles and the dependence of the plasmon absorption on their composition," The Journal of Physical Chemistry B 103, 18 (1999).

[47] H. A. Atwater, "The promise of plasmonics," Sci. Am. 296, 4 (2007).

[48] G. Mie, "Beiträge zur Optik trüber Medien, speziell kolloidaler Metallösungen," Annalen Der Physik 330, 3 (1908).

[49] W. A. Murray, and W. L. Barnes, "Plasmonic materials," Adv Mater 19, 22 (2007).

[50] D. K. Gramotnev, and S. I. Bozhevolnyi, "Plasmonics beyond the diffraction limit," Nature Photonics 4, 2 (2010).

[51] P. R. West, S. Ishii, G. V. Naik, N. K. Emani, V. M. Shalaev, and A. Boltasseva, "Searching for better plasmonic materials," Laser & Photonics Reviews 4, 6 (2010).

[52] R. Ikkawi, N. Amos, A. Lavrenov, A. Krichevsky, D. Teweldebrhan, S. Ghosh, A. Balandin, D. Litvinov, and S. Khizroev, "Near-Field Optical Transducer for Heat-

Assisted Magnetic Recording for Beyond-10-Tbit/in 2 Densities," Journal of Nanoelectronics and Optoelectronics 3, 1 (2008).

[53] Z. Bandic, and R. H. Victora, "Advances in magnetic data storage technologies," Proc IEEE 96, 11 (2008).

[54] M. N. Baibich, J. Broto, A. Fert, F. N. Van Dau, F. Petroff, P. Etienne, G. Creuzet, A. Friederich, and J. Chazelas, "Giant magnetoresistance of (001) Fe/(001) Cr magnetic superlattices," Phys. Rev. Lett. 61, 21 (1988).

[55] L. Néel, "Théorie du traînage magnétique des ferromagnétiques en grains fins avec applications aux terres cuites," Ann.Géophys 5, 2 (1949).

[56] W. A. Challener, T. W. Mcdaniel, C. D. Mihalcea, K. R. Mountfield, K. Pelhos, and I. K. Sendur, "Light delivery techniques for heat-assisted magnetic recording," Japanese Journal of Applied Physics 42, 2S (2003).

[57] L. Pan, and D. B. Bogy, "Data storage: Heat-assisted magnetic recording," Nature Photonics 3, 4 (2009).

[58] B. C. Stipe, T. C. Strand, C. C. Poon, H. Balamane, T. D. Boone, J. A. Katine, J. Li, V. Rawat, H. Nemoto, and A. Hirotsune, "Magnetic recording at 1.5 Pb m− 2 using an integrated plasmonic antenna," Nature Photonics 4, 7 (2010).

[59] Y. Shiroishi, K. Fukuda, I. Tagawa, H. Iwasaki, S. Takenoiri, H. Tanaka, H. Mutoh, and N. Yoshikawa, "Future options for HDD storage," Magnetics, IEEE Transactions On 45, 10 (2009).

[60] M. H. Kryder, E. C. Gage, T. W. McDaniel, W. A. Challener, R. E. Rottmayer, G. Ju, Y. Hsia, and M. F. Erden, "Heat assisted magnetic recording," Proc IEEE 96, 11 (2008).

[61] K. Gao, X. Wang, T. Rausch, A. Wu, Y. Kubota, T. Klemmer, C. Peng, Y. Peng, D. Karns, and X. Zhu, From Perpendicular Magnetic Recording to Heat Assisted Magnetic Recording, IEEE, (2012), p. 1.

[62] A. Q. Wu, Y. Kubota, T. Klemmer, T. Rausch, C. Peng, Y. Peng, D. Karns, X. Zhu, Y. Ding, and E. K. Chang, "HAMR Areal Density Demonstration of 1 Tbpsi on Spinstand," Magnetics, IEEE Transactions On 49, 2 (2013).

[63] A. E. Clark, M. Wun-Fogle, J. B. Restorff, T. A. Lograsso, and J. R. Cullen, "Effect of quenching on the magnetostriction on Fe< sub> 1-x Ga< sub> x(0.13 x< 0.21)," Magnetics, IEEE Transactions On 37, 4 (2001).

[64] D. Iselt, U. Gaitzsch, S. Oswald, S. Fähler, L. Schultz, and H. Schlörb, "Electrodeposition and characterization of Fe< sub> 80 Ga< sub> 20 alloy films," Electrochim. Acta 56, 14 (2011).

[65] C. Mudivarthi, M. Laver, J. Cullen, A. B. Flatau, and M. Wuttig, "Origin of magnetostriction in Fe–Ga," J. Appl. Phys. 107, 9 (2010).

[66] J. J. Park, M. Reddy, C. Mudivarthi, P. R. Downey, B. J. Stadler, and A. B. Flatau, "Characterization of the magnetic properties of multilayer magnetostrictive iron-gallium nanowires," J. Appl. Phys. 107, 9 (2010).

[67] D. Flamini, S. Saidman, and J. Bessone, "Electrodeposition of gallium onto vitreous carbon," J. Appl. Electrochem. 37, 4 (2007).

[68] P. McGary, and B. Stadler, "Electrochemical deposition of Fe 1-x Ga x nanowire arrays," J. Appl. Phys. 97, 10 (2005).

[69] K. Reddy, E. C. Estrine, D. Lim, W. H. Smyrl, and B. J. Stadler, "Controlled electrochemical deposition of magnetostrictive Fe 1− x Ga x alloys," Electrochemistry Communications 18, (2012).

[70] J. R. Hattrick-Simpers, D. Hunter, C. M. Craciunescu, K. S. Jang, M. Murakami, J. Cullen, M. Wuttig, I. Takeuchi, S. E. Lofland, and L. Benderksy, "Combinatorial investigation of magnetostriction in Fe–Ga and Fe–Ga–Al," Appl. Phys. Lett. 93, 10 (2008).

[71] A. Clark, K. Hathaway, M. Wun-Fogle, J. Restorff, T. Lograsso, V. Keppens, G. Petculescu, and R. Taylor, "Extraordinary magnetoelasticity and lattice softening in bcc Fe-Ga alloys," J. Appl. Phys. 93, 10 (2003).

[72] M. Schlesinger, and M. Paunovic, Modern Electroplating, John Wiley & Sons, (2011).

[73] S. Dimitrijević, M. Rajčić-Vujasinović, and V. Trujić, "Non-Cyanide Electrolytes for Gold Plating–A Review," Int.J.Electrochem.Sci 8, (2013).

[74] T. A. Green, "Gold electrodeposition for microelectronic, optoelectronic and microsystem applications," Gold Bulletin 40, 2 (2007).

[75] M. Liew, S. Roy, and K. Scott, "Development of a non-toxic electrolyte for soft gold electrodeposition: an overview of work at University of Newcastle upon Tyne," Green Chem. 5, 4 (2003).

[76] S. Link, Z. L. Wang, and M. A. El-Sayed, "How Does a Gold Nanorod Melt?#," The Journal of Physical Chemistry B 104, 33 (2000).

[77] D. Josell, and T. Moffat, "Extreme Bottom-up Filling of Through Silicon Vias and Damascene Trenches with Gold in a Sulfite Electrolyte," J. Electrochem. Soc. 160, 12 (2013).

[78] H. Honma, and Y. Kagaya, "Gold plating using the disulfiteaurate complex," J. Electrochem. Soc. 140, 9 (1993).

[79] T. Green, and S. Roy, "Speciation analysis of Au (I) electroplating baths containing sulfite and thiosulfate," J. Electrochem. Soc. 153, 3 (2006).

[80] T. Green, M. Liew, and S. Roy, "Electrodeposition of gold from a thiosulfate-sulfite bath for microelectronic applications," J. Electrochem. Soc. 150, 3 (2003).

[81] T. Osaka, A. Kodera, T. Misato, T. Homma, Y. Okinaka, and O. Yoshioka, "Electrodeposition of Soft Gold from a Thiosulfate-Sulfite Bath for Electronics Applications," J. Electrochem. Soc. 144, 10 (1997).

[82] M. J-Liew, S. Sobri, and S. Roy, "Characterisation of a thiosulphate–sulphite gold electrodeposition process," Electrochim. Acta 51, 5 (2005).

[83] S. Sobri, and S. Roy, "Gold electrocrystallization from a spent thiosulfate-sulfite electrolyte," J. Electrochem. Soc. 152, 9 (2005).

[84] W. N. Perera, G. Senanayake, and M. J. Nicol, "Interaction of gold (I) with thiosulfate–sulfite mixed ligand systems," Inorg. Chim. Acta 358, 7 (2005).

[85] A. M. Sullivan, and P. A. Kohl, "Electrochemical study of the gold thiosulfate reduction," J. Electrochem. Soc. 144, 5 (1997).

[86] T. Osaka, M. Kato, J. Sato, K. Yoshizawa, T. Homma, Y. Okinaka, and O. Yoshioka, "Mechanism of sulfur inclusion in soft gold electrodeposited from the thiosulfate-sulfite bath," J. Electrochem. Soc. 148, 10 (2001).

[87] I. Tabakovic, J. Qiu, S. Riemer, M. Sun, V. Vas'ko, and M. Kief, "CoFeRh alloys: Part 1. Electrodeposition of Rh and nonmagnetic CoFeRh alloy," Electrochim. Acta 53, 5 (2008).

[88] P. Nagpal, N. C. Lindquist, S. H. Oh, and D. J. Norris, "Ultrasmooth patterned metals for plasmonics and metamaterials," Science 325, 5940 (2009).

[89] F. Hubenthal, T. Ziegler, C. Hendrich, M. Alschinger, and F. Träger, "Tuning the surface plasmon resonance by preparation of gold-core/silver-shell and alloy nanoparticles," The European Physical Journal D-Atomic, Molecular, Optical and Plasma Physics 34, 1 (2005).

[90] S. A. Maier, Plasmonics: Fundamentals and Applications, Springer, (2007).

[91] L. Vitos, A. Ruban, H. L. Skriver, and J. Kollar, "The surface energy of metals," Surf. Sci. 411, 1 (1998).

[92] Z. Wang, M. Mohamed, S. Link, and M. El-Sayed, "Crystallographic facets and shapes of gold nanorods of different aspect ratios," Surf. Sci. 440, 1 (1999).

[93] Z. Wang, R. Gao, B. Nikoobakht, and M. El-Sayed, "Surface reconstruction of the unstable {110} surface in gold nanorods," The Journal of Physical Chemistry B 104, 23 (2000).

[94] R. Keller, and R. Geiss, "Transmission EBSD from 10 nm domains in a scanning electron microscope," J. Microsc. 245, 3 (2012).

[95] G. S. Rohrer, "Grain boundary energy anisotropy: a review," J. Mater. Sci. 46, 18 (2011).